2022

Engineering of thermal conductivity in functional materials using chemical doping and nanoparticle additives

Md Rezoanur Rahman

UNIVERSITY OF WOLLONGONG AUSTRALIA

Institute for Superconducting and Electronic Materials

Engineering of thermal conductivity in functional materials using chemical doping and nanoparticle additives

Md Rezoanur Rahman

Supervisors:

Dr David Cortie

Distinguished Prof. Xiaolin Wang

This thesis is presented as part of the requirements for the Award of the Degree of 'Masters of Philosophy of the University of Wollongong

April 2022

CERTIFICATE OF RESEARCH

This is to certify that the work presented in this thesis is carried out by the author under the supervision of Dr David Cortie, Senior Research Fellow of the Institute for Superconducting and Electronic Materials, Australian Institute for Innovative Materials, University of Wollongong, Australia.

Dr David Cortie **Md Rezoanur Rahman**

IMPACT OF COVID-19

Since March 2020, New South Wales (NSW), the Australian state in which the University of Wollongong (UOW) is located, has been significantly impacted by the COVID-19 pandemic. NSW has experienced two 'lockdown' periods resulting in considerable disruptions to the research activities of Higher Degree Research students at UOW. As a UOW HDR student, I have been impacted by these COVID-19-related disruptions, and my research has similarly been impacted.

DECLARATION

I, Md Rezoanur Rahman, declare that this thesis, submitted in fulfilment of the requirements for the award of Masters of Philosophy in the Institute for Superconducting and Electronic Materials, Australian Institute for Innovative Materials, University of Wollongong, is wholly original work unless otherwise referenced or acknowledged. I acknowledge the contributions of Dr Sheik Md Kazi Nazrul Islam in Chapter 4 with XRD, SEM measurements and the synthesis process. In Chapter 6, Mr Abuduliken Bake performed the vibrating sample magnetometry. This thesis has not been submitted for qualifications at any other academic institution.

Md Rezoanur Rahman

April 2022

ABSTRACT

The intrinsic ability of solid materials to conduct heat is called thermal conductivity (and here is denoted by the symbol κ). It is essential to control the thermal conductivity in functional materials wherever heat transfer plays a key role, such as in thermoelectric devices, "thermal interface" materials for heat management in electronics, biomedical implants and personal protective equipment. Techniques are needed to tailor the thermal conductivity for specific applications. For example, thermoelectric devices require lower thermal conductivity to maximise their efficiency. Such devices offer a way to capture approximately 60-70% of the energy that is converted into unused heat as a secondary by-product of many technological and industrial processes. Consequently, methods to control thermal conductivity are important to improve thermo-electronic devices' efficiency. This thesis focuses on controlling thermal conductivity using chemical doping methods, including embedding a secondary phase of nanoparticles into a primary phase to form a so-called nanocomposite. In this thesis, the laser flash analysis technique was applied as the principal method to understand the thermal transport behaviour among the fabricated materials.

The first section of the research project focused on producing chemically doped thermoelectric materials where sodium and oxygen were substituted into Cu_2Se to reduce the thermal conductivity. This project used a solid-state reaction with Na_2CO_3 using the melt-route fabrication process to obtain a surprisingly strong effect on the thermal and electrical conductivity for the well-known thermoelectric material Cu_2Se. The reaction with Na_2CO_3 (0.09, 0.18, 0.35, 0.70, and 1.40 wt.%) in Cu_2Se leads to a decreased thermal conductivity within the temperature range of 355 K to 981 K. The lowest thermal conductivity (κ) observed is for the 1.40 wt. % Na_2CO_3 (0.464

$W.m^{-1}.K^{-1}$ at 554 K), and this is ~34% lower than pure Cu_2Se (0.709 $W.m^{-1}.K^{-1}$ at 554 K). The reduction in thermal conductivity for the material is attributed to the high density of defects causing the scattering of phonons via the effect of Na and O doping in the Cu_2Se matrix.

The second part of the thesis investigated modifying the thermal conductivity of Bi_2Te_3 and its composites by developing composites of polymers combined with an inorganic (Bi_2Te_3) thermoelectric filler phase. Using an inorganic filler phase in a polymer is a possible way to produce prospective flexible, wearable thermoelectric devices. As a starting point, this study investigated the inclusion of chemically-exfoliated Bi_2Te_3 into polyurethane (Chronoflex®) to find the best methods to control thermal conductivity in nanocomposite forms as a step toward future flexible thermoelectric composites. The thermal characterization of nanoparticle-embedded polymer composites was performed using laser flash analysis (Linseis LFA 1000) at room temperature on neat polyurethane, 2 v%, 4%, 7% Bi_2Te_3 (% by volume) composites, which were compared with measurements on a pure Bi_2Te_3 single crystal. The thermal conductivity in 2%, 4% and 7% Bi_2Te_3-PU was 0.11, 0.12, and 0.23 $Wm^{-1}k^{-1,}$ respectively, which was reduced by up to 94% in 2% Bi_2Te_3-PU compared to the pure Bi_2Te_3 crystal (1.7089 $Wm^{-1}k^{-1}$). Additionally, the Bi_2Te_3-PU composites showed a 16% reduction in 2 % Bi_2Te_3-PU compared with the expected thermal conductivity calculated using the Law of Mixtures, whereas 4% Bi_2Te_3-PU showed a 24% reduction. Future efforts are needed to improve the electrical conductivity in these materials to enable thermoelectric applications; however, the initial results show a promising reduction of thermal conductivity and flexibility, so Bi_2Te_3-PU composites could also be useful as a low thermal conductive substrate for a variety of other purposes.

In the project's third phase, nanocomposites of polyurethane with embedded superparamagnetic Fe_3O_4 nanoparticles were explored to identify the trends in thermal conductivity and magnetic properties. Such materials offer prospective hybrid composites enabling magnetic inductive heating technology. These are multifunctional and can, for example, potentially be combined with thermoelectric generators, although the overall device performance will have a trade-off that depends on the thermal conductivity of the components. The thermal conductivity is increased by 41% in 7 wt. % Fe_3O_4-PU (0.13 $W.m^{-1}.K^{-1}$), 51% in 10 wt. % of Fe_3O_4-PU (0.14 $W.m^{-1}.K^{-1}$), and 178% in 13 wt. % Fe_3O_4-PU composites (0.26 $W.m^{-1}.K^{-1}$) compared to neat polyurethane (0.094 $W.m^{-1}.K^{-1}$). The magnetic properties were also studied between 5–300 K using vibrating sample magnetometry to determine the embedded oxide particles' superparamagnetic mean blocking temperature (T_B=90 K). Using an AC magnetic field operating at 85 kHz, remote heating was demonstrated of the plastic with Fe_3O_4 nanoparticles submerged in a water environment up to 45 °C within 18 minutes. This work shows that, in the future, it will be possible to custom-design plastic magnetic objects that can be heated remotely to achieve a variety of functionalities. Due to their tuneable thermal conductivity, flexibility and biocompatibility, the Fe_3O_4-PU composites may be explored further in the future for skin-compatible wearable electronic devices, hybrid inductive-thermoelectric generators and 3D-printable biomedical structures.

ACKNOWLEDGEMENTS

First and foremost, all praise and gratitude to Allah, the Almighty, for giving me the strength and patience to complete this thesis work.

I would like to express my sincere appreciation and heartfelt gratitude to my principal supervisor Dr David Cortie for his academic guidance, continuous support, enthusiastic encouragement and kindness during my MPhil study at the Institute for Superconducting & Electronic Materials (ISEM), the University of Wollongong (UOW), Australia. He has been a great mentor in mapping my MPhil journey, advising on research topics, and connecting me with my needed resources. I would also like to thank my co-supervisor, Distinguished Professor Xiaolin Wang, for valuable guidance, support, and laboratory facilities during my journey at the Institute for Superconducting & Electronic Materials (ISEM), the University of Wollongong (UOW).

I am thankful for my International Postgraduate Tuition Award from the University of Wollongong, Australia, to support me during my MPhil financially.

I acknowledge the beamtime provided by the Australian Synchrotron to obtain variable temperature X-ray diffraction patterns presented in the chapter on Cu_2Se.

I would like to express my appreciation to Dr Germanas Peleckis, Dr Mitchell Nancarrow, Mr Tony Romeo and Dr Dongqi Shi for their contributions to training and maintaining relevant instruments and for doing measurements for some samples.

I would like to thank my dear friends and colleagues, including Dr Sheik Md Kazi Nazrul Islam, Mr Abuduliken Bake, Mr Caleb Stamper, Mr Kyle Portwin, Dr Al Jumlat Ahmed, Dr Guangsai Yang, Dr Weiyao Zhao, Mr Yaser Rehman, Marcela Chaki Borras and other students and staff in ISEM. My special thanks are owed to Dr Sheik Md Kazi Nazrul Islam for his collaboration in chapter 4 and for guiding me from the beginning of my Mphil degree. My special thanks also go to Mr Caleb Stamper for his critical thesis review. Finally, my gratitude goes to Professor Michael Cortie for his valuable time to review the thesis.

This thesis could not have been completed without my parents' contributions and my brothers and sister. They continuously encouraged me to obtain this higher degree. Their unfailing support and advice helped me to accomplish this study. I would also like to acknowledge my aunt Achia Khan Sumona for supporting me mentally with her motivation and guidance from the beginning of my journey of higher studies in Australia.

LIST OF PUBLICATIONS

The following publications were produced during the period of the Master's research. Publications directly related to the contents of the thesis are indicated by an asterix*.

1. Sheik Md Kazi Nazrul Islam, **Md Rezoanur Rahman,** Al Jumlat Ahmed, Frank Fei Yun, David L. Cortie, Xiaolin Wang, Michael B. Cortie " Beneficial effect of Na_2CO_3 additions on the thermoelectric performance of melt-route Cu_2Se, https://doi.org/10.1002/aelm.202100802 *

2. Abdulhakim Bake, **Md Rezoanur Rahman**, Peter J. Evans, Michael Cortie, Mitchell Nancarrow, Radu Abrudan, Florin Radu, Yury Khaydukov, Grace Causer, Sara Callori, Karen L. Livesey, David Mitchell, Zeljko Pastuovic, Xiaolin Wang, and David Cortie, " Structure and magnetism of ultra-small cobalt particles assembled at titania surfaces by ion beam synthesis" Volume 570, 30 December 2021, 151068, https://doi.org/10.1016/j.apsusc.2021.151068.

3. Abdulhakim Bake, **Md Rezoanur Rahman**, Peter J. Evans, Michael Cortie, Mitchell Nancarrow, Radu Abrudan, Florin Radu, Yury Khaydukov, Grace Causer, Sara Callori, Karen L. Livesey, David Mitchell, Zeljko Pastuovic, Xiaolin Wang, and David Cortie, "Ultra-small cobalt particles embedded in titania by ion beam synthesis: Additional datasets including electron microscopy, neutron reflectometry, modelling outputs and particle size analysis." https://doi.org/10.1016/j.dib.2021.107674

4. Shahbaz Khan, Nicholas B. Lawler, Abdulhakim Bake, **Md Rezoanur Rahman**, David Cortie, Killugudi Swaminathan Iyer, Mariusz Martyniuk and Mikhail Kostylev, "Iron Oxide-Palladium core-shell nanospheres for ferromagnetic resonance-based hydrogen gas sensing" https://doi.org/10.1016/j.ijhydene.2021.12.135

5. **Md Rezoanur Rahman**, Abdulhakim Bake, Jumlat Al Ahmed, Liang Wu, Hadis Khakbaz, Sara FitzGerald, Artek Chalifour, Karen L. Livesey, Jonathan C. Knott, Peter Innis, Stephen Beirne, David Cortie, " Targeted heating of a biocompatible thermoplastic using embedded superparamagnetic Fe_3O_4 nanoparticles" Manuscript ID an-2021-02524h, ACS Applied Nano Materials, (**Under Review**). *

6. **Md Rezoanur Rahman**, Caleb Stamper, Sheik Md Kazi Nazrul Islam, David Cortie, "Thermal conductivity of Nomex under different conditions" (**Preparing for submission**).

7. **Md Rezoanur Rahman**, Sheik Md Kazi Nazrul Islam, Abdulhakim Bake, David Cortie, "Significant modification of the thermal diffusivity using exfoliated Bi_2Te_3 embedded into polyurethane by applying a solvent-based processing method." (**Preparing for submission**). *

TABLE OF CONTENTS

LIST OF FIGURES

LIST OF TABLES

LIST OF ABBREVIATIONS

XRD	X-ray diffraction
SHT-XRD	Synchrotron high temperature X-ray diffraction
FE-SEM	Field emission scanning electron microscopy
EDS	Energy-dispersive X-ray spectroscopy
STEM	Scanning transmission electron microscopy
PLD	Pulsed laser deposition
SPS	Spark plasma sintering
DSC	Differential scanning calorimetry
PPMS	Physical properties measurement system
TE	Thermoelectric
TEG	Thermoelectric generator
TEC	Thermoelectric cooler
R_p	Profile R-factor
R_{wp}	Weighted Profile R-factor
GOF	Goodness of fit
LN	Liquid nitrogen
σ	Electrical conductivity
S	Seebeck coefficient
D	Thermal diffusivity
κ	Thermal conductivity
Fcc	Face-centred cubic
L	Lorentz factor

ξ	Interaction parameter
r	Scattering parameter
k_B	Boltzmann constant
e	Electron charge

CHAPTER 1: Introduction

1.1.Overview

Heat flow plays a vital role in the performance of many materials. For example, in materials used in solar cells or batteries in electronic vehicles, the goal is to enhance heat flow to avoid device degradation. In other devices, such as thermoelectrics, the challenge is to retard heat flow to achieve high thermal gradients. To address these challenges, one can use special “heat-functionalised” materials to achieve extreme thermal conductivity or heat-enhanced functionalities. Thermal conductivity in materials and heat-functional materials is essential in several industries, such as solar cells and wearable smart devices. Heat functional materials can resist damage, increase product lifetime, and save energy by playing a vital role in heat conduction. These types of materials have two major forces in the worldwide context, the first one is to enhance environmental sustainability, and the second is energy[1]. The second driving force is economical by saving energy and preserving fossil fuel stocks. Regarding converting heat into energy, maximum heat management can open several doors in the modern world for producing smart devices. For example, thermoelectric materials could be a primary attraction as wearable devices to extract energy from the human body. Other potential applications for advanced thermal materials include solar cells, green energy, environmentally friendly electronic devices, smart vehicles, energy-efficient buildings, thermoplastic industries, and space/aviation technology. This thesis explores methods to control different materials' thermal conductivity, including examples where heat can be generated or utilized in heat-functional materials (via thermoelectric effects or magnetic induction). The two main strategies to control the thermal conductivity explored in this thesis are chemical doping and forming composites via adding nanoparticles.

1.1. Chemical doping

Doping is a technique to intentionally introduce impurities into a material to change the samples' properties, such as physical, electrical, and thermal properties. Chemical doping is a widely acceptable and popular method among several doping techniques for improving thermoelectric materials' performance. Chemical doping is a technique where chemical reactions occur to incorporate and substitute specific elements into the crystal structure of a compound. For example, in chapter 4, due to the reactions of $Na_2CO_3 \rightarrow Na_2O$ (s) + CO_2 (g) followed by $Na_2O \rightarrow 2Na$ (g) + 1/ $2O_2$ (g), Na and O atoms have been produced, which are incorporated into the Cu_2Se matrix via a substitutional chemical reaction as impurities. This influences the Seebeck effect, electrical conductivity and thermal conductivity [2]. Moreover, chemical doping in thermoelectric materials can significantly enhance thermoelectric performance by reducing thermal conductivity [2], modifying the power factor [3], electrical conductivity, Hall coefficient and the concentration/mobility of electronic carriers [4]. Introducing impurities impacts the thermal conductivity of thermoelectric materials using point defect methods which influence phonon scattering (brief description in sections 2.4 and 2.5). Introducing impurities into thermoelectric materials generally reduces the phonon mean free path, which helps to reduce thermal conductivity.

1.2.Nanocomposites

A nanocomposite is a composite mixture of two or more materials, where one of the component materials has a sub-micron-scale structure [5]. The aim of mixing several materials is to produce new composites with enhanced properties beyond those of the starting components [6]. Descriptively, the nanocomposite is a hybrid composite that expresses intrinsically new properties which are absent in the macro composites or pure composites/materials. The inherently unique

properties come from the nanoscale level materials. The basic concept of building nanocomposites is creating new designs and structures using different dimensions to get unprecedented thermal behaviour and improved physical properties. There are several properties such as mechanical, electrical, thermal, optical, electrochemical, and catalytic performance which are known to depend closely on the size of the starting nanostructures. Therefore, the size of the elements in composites can significantly impact the nanocomposites' properties. For example, the smaller particle size leads to a more significant interface density, which generally reduces the thermal conductivity of the nanocomposite [7].

1.3. Key criteria for selecting materials

Materials selection for thermal applications must take account of many factors. Among all the factors, thermal stability, chemical resistance in the target working environment, mechanical behaviour of the materials in particular environments, and the selected materials' physical properties are necessary to consider. For many applications, including thermoelectric devices, selected materials have a long lifetime, especially for industrial uses.

Their certain key physical properties have a significant effect on materials for high temperature/thermal applications; for this reason, the following critical criteria should be considered carefully:

- **Thermal conductivity**: The materials must have very specific thermal conductivity depending on the types of purposes. For example, thermoelectric materials require low thermal conductivity (κ), whereas thermal interface materials require high conductivity (κ).

- **Melting Point**: Selection of high melting point materials depends on their applications. For high-temperature applications, the materials must have high melting points. But for medical thermal composites, the melting point doesn't need to be high in general.

- **Phase stability:** To maximize the thermal and electrical performance over long time periods, the primary materials, along with any composite or nanofiller phases, should be in a stable phase that does not undergo thermal degradation at the target temperature.

- **Electrical conductivity**: Higher electrical conductive materials are generally considered the best candidate for thermoelectrics, although there is a tradeoff with the Seebeck effect and thermal conductivity. Combining higher electrical conductivity and lower thermal conductivity makes it possible to get a higher figure-of-merit (ZT).

- **Environmental friendly:** With the new change in the modern world to minimise greenhouse gas, and toxicity, it is important to consider eco-friendly thermoelectric materials. A significant challenge is to select non-toxic thermoelectric materials as most high-performance thermoelectric materials have some toxic properties.

1.4.Outline of the thesis

This thesis is discussed in seven chapters. **The first chapter** briefly introduces heat-functionalised materials, their applications, nanocomposites, and the key criteria for selecting appropriate component materials**. Chapter 2** gives detailed information about thermal conductivity, the theory of thermal conductivity of different materials, the techniques to reduce thermal conductivity, several models of thermal conductivity and their mathematical expressions, and motivation to modulate thermal conductivity using the nanoengineering approach. The final part of chapter 2

discusses thermoelectric materials (Cu_2Se, Bi_2Te_3) and superparamagnetic (Fe_3O_4) as components in heat-functionalised materials. Flowing on from this, **Chapter 3** explains the fabrication methods for selected materials and their characterization technique with a brief description of devices. Chapter 3 also explains several forms of thermal analysis techniques, emphasizing laser flash analysis techniques and their models. **Chapter 4** presents a study of the significantly reduced thermal conductivity Cu_2Se with Na, O dopants prepared by a chemical reaction with Na_2CO_3 during a melt route solidification method. **Chapter 5** investigates the thermal conductivity of Bi_2Te_3 embedded into polyurethane matrix by applying a solvent-based processing method. The liquid phase exfoliation method was also discussed, which was used to prepare Bi_2Te_3 as a nanofiller for the polyurethane. **Chapter 6** demonstrates targeted heating and reports the thermal properties of a biocompatible thermoplastic using embedded superparamagnetic Fe_3O_4 nanoparticles. Additionally, the possibility of remote heating for hyperthermia treatment is also explained in this chapter. **Chapter 7** summarises all the work done throughout my MPhil degree and provides a brief conclusion of the thesis chapters and an outline of future work.

Chapter 2: Literature Review

2.1.Thermal conductivity

Thermal conductivity is considered a critical property of solid materials and has been studied widely over many decades [8]. Thermal materials have a vital role in flexible electronics, wearable electronics devices, artificial intelligence chips, thermal protection and personal protection, advanced detectors, thermoelectric devices, and so on.

Thermal conductivity specifies the ability of a material to transfer heat and is denoted by κ with the unit of $W \cdot m^{-1} \cdot K^{-1}$.

2.1.1. Fourier's law of thermal conduction

Fourier's law of thermal conduction can explain the heat transfer processes at non-cryogenic temperatures, and for solid-state materials, the key characteristic parameter in Fourier's Law is the thermal conductivity (κ).

According to Fourier's law of thermal conduction, the heat flux is proportional to the negative gradient of temperature and the material's thermal conductivity, where the heat flux is the rate of heat transfer per unit area in the direction of heat transfer. The differential form of Fourier's law of thermal conduction is:

$$q = -\kappa \nabla T \qquad 2.1$$

Where,

q = local heat flux [W. m^{-2}]

κ = material's thermal conductivity [W. $m^{-1}.K^{-1}$]

∇T = temperature gradient [$K.m^{-1}$]

2.2.Theory of thermal conduction

The elementary excitation of the quantum mechanical vibration phenomenon inside a crystal lattice is known as a phonon [9]. Phonons can travel through a material or inside the crystal and are affected by scattering. Phonon scattering mainly arises due to anharmonicity within the crystal potential. There are three types of phonon scattering mechanisms that are typically considered:

1. Boundary scattering
2. Mass defect scattering
3. Phonon-phonon scattering

In many insulating materials, phonons are the main carriers of heat. If electronic carriers are also present, then thermal conductivity (κ) consists of contributions from charge carriers (electrons) (κ_c) and lattice vibrations (phonons), (κ_L). (See following equation: 2.2)

$$\kappa = \kappa_c + \kappa_L \qquad 2.2$$

The electronic thermal conductivity can be calculated by:

$$\kappa_c = L\sigma T \qquad 2.3$$

Where,

κ_c = electronic thermal conductivity

L = Lorentz number

σ = electrical conductivity

T = absolute temperature

If the phonon bandstructure is known, the lattice thermal conductivity can be calculated using kinetic theory, and the Boltzmann transport equation [10]:

$$\kappa_L = \frac{1}{3} \int C\ (\omega) V(\omega) l(\omega) d\omega \qquad 2.4$$

Here,

κ_L = lattice thermal conductivity

C = single phonon specific heat

V = single phonon velocity

L = single phonon mean free path

ω = phonon frequency

For good electrical conductors such as metals, electrons are responsible for carrying heat, whereas lattice vibrations are predominately responsible for heat transport in semiconductors and dielectric materials. The Lorentz number is material-dependent and has values such as $1.5 \times 10^{-8}\ \mathrm{W\Omega K^{-2}}$ for non-degenerate semiconductors, $2.0 \times 10^{-8}\ \mathrm{W\Omega K^{-2}}$ for degenerated semiconductors, and $2.45 \times 10^{-8}\ \mathrm{W\Omega K^{-2}}$ for heavily doped semiconductors.

2.2.1. Theory of thermal transport in crystalline materials

Thermal energy is transferred in solid materials by two means: thermal energy carried by electrons, and lattice vibrations, i.e., phonons. In the case of a metal, electrons are primarily responsible for transferring thermal energy. In contrast, lattice vibrations dominate thermal transport in dielectric solids such as semiconductors and insulators. A phonon carries collective energy with its own

wave vector frequency and moves with a specific velocity for a given crystalline solid. Phonons carry heat energy like other particles that travel inside the system and experience resistance, analogous to the transport of gas molecules. Therefore, a few factors such as defects, imperfections, material boundaries, and other phonons determine the phonon relaxation time and impact phonon scattering rate.

Additionally, temperature gradients can drive phonon diffusion in a periodic solid as thermal transport. The theory is well known as "**the phonon gas model."** According to gas kinetic theory and Debye's specific heat theory, the conductivity of a crystalline solid is expressed as [10] following equation

$$\kappa = \frac{1}{3} c_v v_g l = \frac{1}{3} C_v v_g^2 \tau \qquad 2.5$$

Where,

C_v = average specific heat per unit volume

v_g = average phonon group velocity

l = average phonon mean free path

τ = relaxation time

Peierls modified Debye's specific heat theory and Boltzmann's kinetic gas theory [11, 12]. According to Peierls, the phonon distribution can explain heat flux, which can be obtained by solving the Peierls–Boltzmann transport equation. Additionally, the Peierls–Boltzmann statistical distribution is obeyed by phonons. Peierls stated that lattice thermal conductivity increases with increasing temperature due to the temperature dependence of specific heat under low-temperature

conditions. In contrast, under the condition of high temperature, the relation between the lattice thermal conductivity and rate of temperature increment is inversely proportional because the phonon scattering increases at high temperature.

2.2.2. Theory of thermal transport in amorphous and polymer materials

Phonon dispersion relation concepts and phonon group velocity are not rigorously defined in amorphous solids because amorphous materials do not have a periodic crystal structure, which is one of the biggest challenges for researchers to understand the thermal transport properties in amorphous materials. Einstein proposed the "amorphous limit" model in 1911 to explain the mechanism and calculate the minimum lattice thermal conductivity of an amorphous solid [13]. Einstein considered atom vibrations of any solid material as independent and unrelated, but their frequency is the same – called the Einstein frequency. In the proposed model, heat conduction is governed based on the random walk of independent oscillators. In 1979, Slack proposed the "minimum thermal conductivity" model, where he improved Einstein's "amorphous limit" model based on calculating the minimum average free path of phonons with lattice wavelength [14]. However, the special interaction between two adjacent atoms means they cannot be completely independent. Additionally, they vibrate with their adjacent atoms, but their atomic vibration frequencies are different. In 1992, Cahill and other researchers developed the "minimum thermal conductivity" model and provided a new model with a series of oscillators [15]. The oscillator's wavelength is half of the Debye wavelength, where the low-frequency sound speed $\omega = 2\pi\upsilon/\lambda$ gives the oscillators' frequencies.

The lattice thermal conductivity formula is given below

$$\kappa_{min} = \left(\frac{\pi}{6}\right)^{\frac{1}{3}} k_B n^{\frac{2}{3}} \sum_i \upsilon_i \left(\frac{T}{\Theta_D}\right)^2 \int_0^{\Theta_D/T} \frac{x^3 e^x}{(e^x - 1)^2} dx \qquad 2.6$$

Where,

υ_i = speed of the sound

Θ_D = Cutoff frequency of polarization modes = $\nu_i (\hbar/k_B) (6\pi^2 n)^{1/3}$

n = number of the density of atoms.

x = distance of two atoms

k_B = Boltzmann constant

The 'minimum thermal conductivity' framework is widely used to mathematically model amorphous materials' thermal conductivity [15].

The lattice vibration properties between amorphous and crystalline materials are different. The lattice vibrations are considered as phonons in crystalline materials, and the lattice vibration is delocalised as plane waves. In the Debye model, a solid is treated as an elastic continuum for useful approximation under a long-wavelength limit. Heat capacity plays a crucial role in regulating thermal conductivity, while temperature is the principal factor. In the condition of high temperature, heat capacity is independent of temperature, as it follows the Dulong–Petit law. In contrast, the thermal properties show significant differences in amorphous materials compared to crystalline materials. The heat capacity of amorphous materials is higher than crystalline materials, especially in low-temperature regions [16].

2.3.Methods of thermal conductivity measurements

There are several methods to measure thermal conductivity, but two categories of techniques are considered to be the best [17]:

1. Steady-state methods
    - Guarded hot plate
    - Heat-flow meters
    - Direct heating method
    - Pipe method

2. Transient or non-steady-state methods
    - Hot-wire method
    - Hot-disk method
    - Laser flash method
    - The 3-ω method
    - Fitch method
    - Photothermal methods

2.3.1. Comparison between several methods

The comparison between various methods to measure thermal conductivity is given below [18, 19]

Method		Temperature range	Uncertainty and Range	Materials	Positive	Negative
Steady-state method	Guarded hot Plate	80–1500 K	2–5% and 0.0001–1 W/(m K)	Insulation Materials and solid, opaque, insulators	High accuracy	Long measurement, large specimen size, low conductivity materials

	Cylinder	4–1000 K	2%	Metals	Temperature range, simultaneous determination of electrical conductivity	Long measurement
	Heat-flow Meter	(−100-200°C) for normal 90–1300K for axial heat flow and 298–2600 K for radial heat flow	3–10% 0.007–1.0 W/(m K) 0.5–2% and 10–500 W/(m K) (axial) and 3–15% and 0.01–200 W/(m K) (radial)	Insulations, plastics, glasses, ceramics Some metals, rocks, polymers Metals and Solids	Simple construction and operation	Measurement uncertainly, relative measurement
	Comparative	20–1300°C	10–20%	Metals, ceramics, plastics	Simple construction and operation	Measurement uncertainly, relative measurement
	Direct heating	400–3000 K	2–10%	Metals Wires, rods, tubes of electrical conductors	Simple and fast measurements, simultaneous determination of electrically conducting materials	Only electrically conducting materials
	Pipe method	20–2500°C	3–20%	Solids calcium silicates, minerals and refractory fibre blankets	Broad temperature range	Specimen preparation, long measurement time

Transient Methods	Hotwire, hot strip	20–2000°C (−40–1600°C) for hot wire and (−50-500°C) for hot strip 298–1800 K for hot wire	1–10 % for hotwire and 0.1–5 W/(m K) for hot strip 5–15% and 0.02–2 W/(m K) for Hotwire	Liquids, glasses, solids of low refractory materials and plastics, granules, powders for hotwire and glasses, foods, ceramics for hot strip	Broad temperature range, fast, accuracy	Limited to low conductivity materials
	Hot-disk (TPS technique)	30–1200 K	-	liquids, pastes, solids and powders	very short time accuracy, different thermal properties simultaneously	the range of 0.005 and 500 W/(m K) (conducting or insulating material)
	Photothermal (PT), Photoacoustic	30–1500 K −50–500°C and 200–800 K for PT	Not sufficiently known, 1–10 % 0.1–200 W/(m K) for PT	Solids, liquids, gases, thin films [7], small parts of most solid	Usable for thin films, liquids, and gases	The precise accuracy of this method is still the subject of research
	Laser flash	(−100–3000°C) and 100–3300 K	1.5–5% and 0.1–1500 W/(m K)	solids, liquids, and powders and liquid metals, polymer, ceramics	Temperature range, most small specimen, fast, accuracy at high temperature	Expensive,

2.4.Strategies to influence thermal conductivity

The performance of thermoelectric composites largely depends on lattice thermal conductivity (κ_L). As Equation 2.6 outlines, the lattice thermal conductivity mainly depends on three major factors (Figure: 2.1).

- Specific heat
- Velocity of phonon
- Phonon scattering time (lifetime)

It is desirable to control or modify these three parameters in engineering the thermal conductivity for specific applications, as indicated in Figure 2.1. Figure 2.1 also shows that the following factors play a significant role in controlling the thermal conductivity in inorganic and organic composites:

- Strong anharmonicity
- Weak chemical bonds
- Complex primitive cell
- Electron-phonon scattering
- Resonance scattering
- Dislocation scattering
- Boundary scattering
- Point defect scattering
- The construction of nanostructures
- Introduction of interfaces
- Embedding of nanoparticles

In practice, microstructural parameters such as the presence of grain boundaries and dislocations can be controlled via growth conditions, whereas the anharmonic interaction is an intrinsic feature of the material and therefore can only be controlled by altering the basic chemical/crystal structure, which is not always practical.

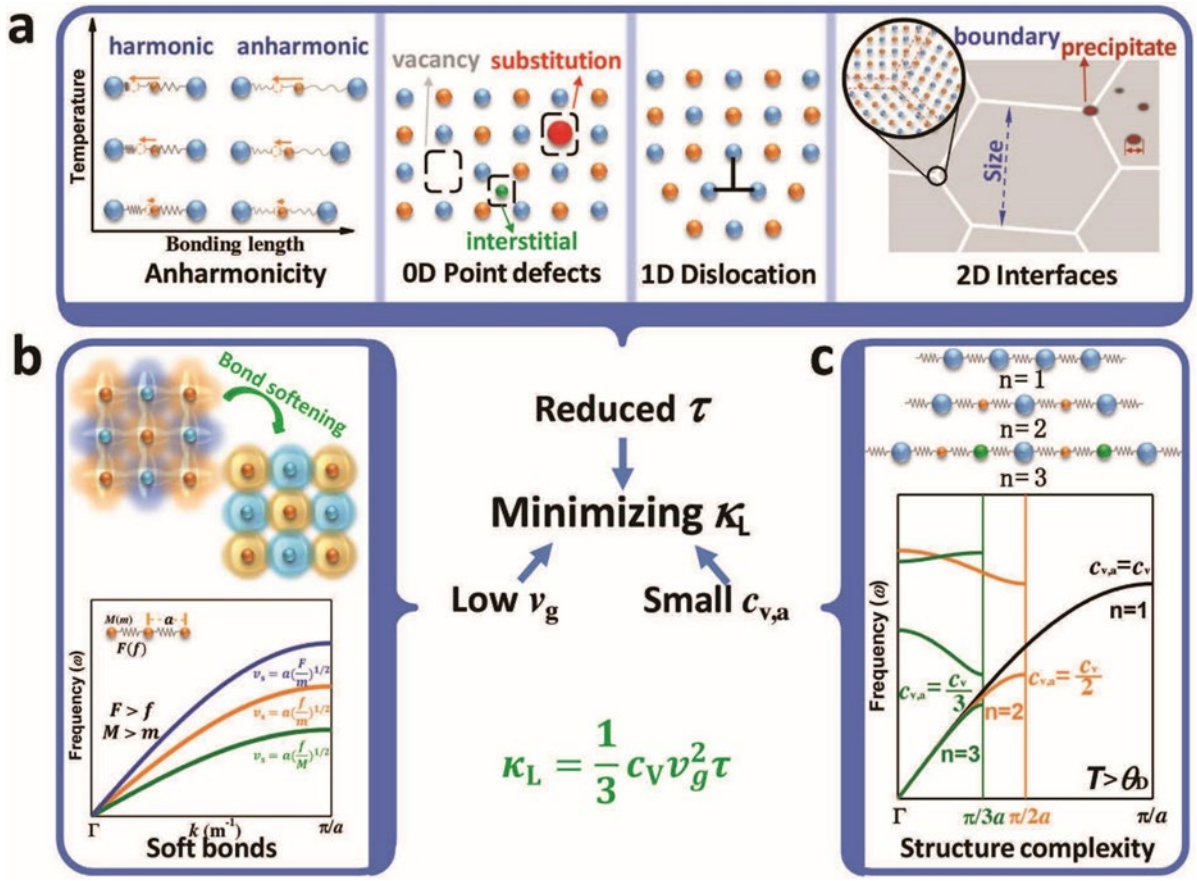

Figure 2.1: A schematic illustration of strategies for minimising lattice thermal conductivity, including phonon scattering due to: a) anharmonicity, multidimensional defects, b) low group velocity resulting from soft bonds and heavy atomic mass, and c) small specific heat of acoustic phonons stemming from crystal structural complexity [20].

For this reason, microstructural control or a moderate amount of doping to form 0D defects are attractive options to modify an existing phase. The effect of microstructure and defects varies in

different classes of materials and needs to be optimised for each case. For example, in the following figure, researchers have been exploring the increase or reduction of thermal conductivity depending on the inclusion of different carbon allotropes and their derivatives. The sections below discuss how the various control parameters such as 0D defects, interfaces, and boundaries can modify the thermal conductivity.

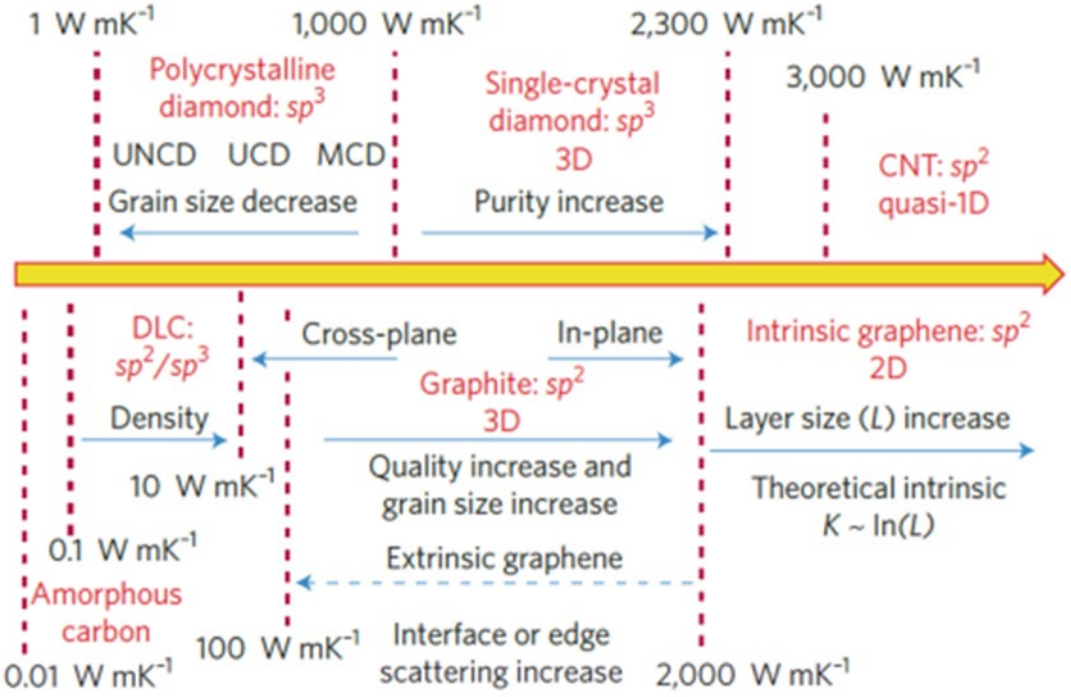

Figure 2.2: Thermal properties of carbon allotropes and their derivatives. Diagram based on average values reported in the literature [21]

2.4.1. Point defects

Point defects can be defined as a missing atom from a crystal, displacements, dopants, impurities in the normal lattice sites, or holes in the lattice structure. Vacancies and interstitials are also considered point defects. Even isotopes with different masses can also be point defects. Due to

point defects in the structure which have a different mass from the surrounding atoms, the phonon scattering rates can be enhanced to higher frequencies. Therefore, introducing impurities/ dopants into crystals or polymer composites is a common way to control thermal conductivity. Point defects can influence phonon scattering in lattice crystals, which impacts the thermal conductivity of the structure.

Mass contrast effects and strain-field fluctuation are considered to be the main mechanisms of point defect engineering. There are three routes to enhance phonon scattering

- Heavy doping, that is, a high amount of substitutional dopants determined by the solubility limit.
- The large mass fluctuation between the dopants and the host elements.
- The large lattice mismatch between the dopant phase and the host phase.

A large lattice parameter difference and ionic size mismatch between the crystal and dopant phase usually leads to low solubility. Therefore there is also a compromise between the solubility limit and a large lattice mismatch. As a result, selecting the best dopant to modify thermal conductivity is challenging. The following figure illustrates different types of point defects in a crystal.

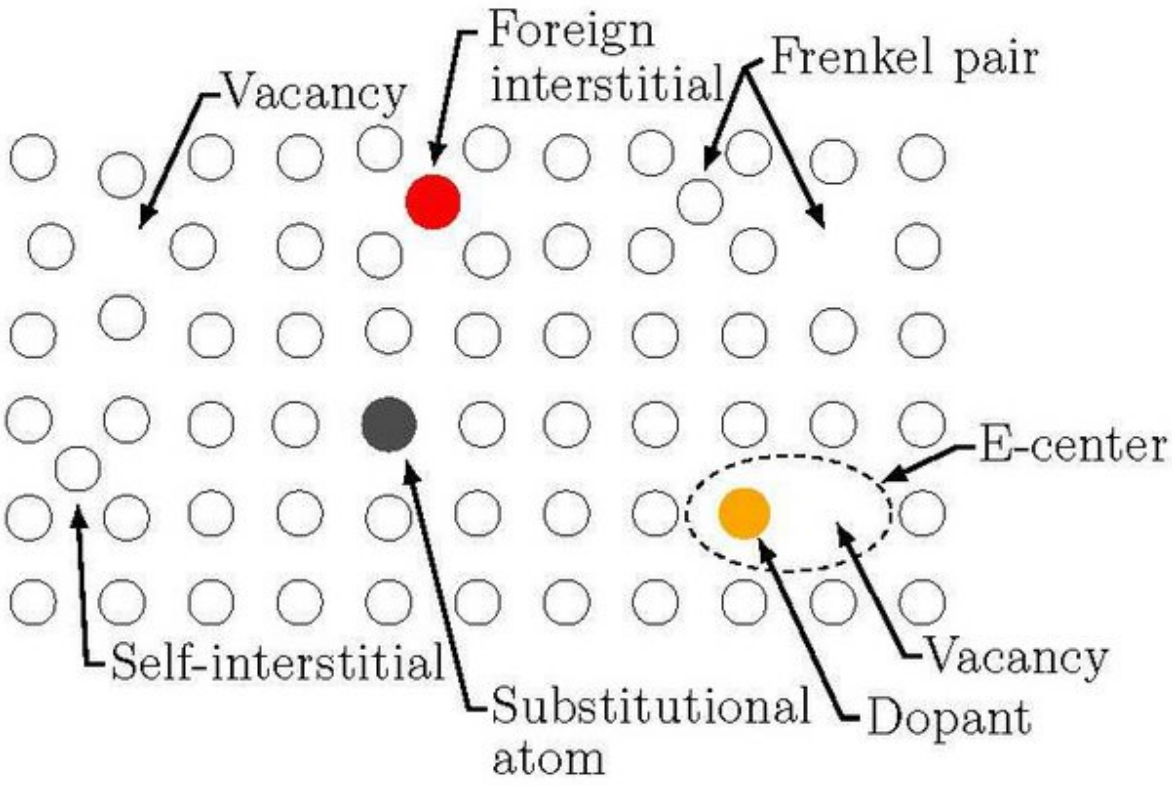

Figure 2.3: Examples of some point defects in a crystal [22].

2.4.2. Boundary scattering

In polycrystalline materials, a grain boundary is an interface between two grains that forms a 2D region in the microstructure. The presence of grain boundaries can decrease thermal conductivity and electrical conductivity in materials [23]. Boundary scattering is considered useful for low-temperature applications as it effectively limits the phonon mean free path at low temperatures. As a result, the materials' thermal conductivity decreases as the phonon mean free path plays a vital role in carrying heat. Boundary scattering mechanisms directly impact the thermal conductivity of composites, as a large part of thermal conductivity depends on low-frequency phonons. Many researchers have proven that boundary phonon scattering reduces thermal conductivity in semiconductor junctions, a major challenge in electronics [24, 25].

The medium and short-wavelength phonons carry the maximum amount of heat in materials. Targeting specific regions to reduce thermal conductivity is possible by a two-dimensional interface scattering mechanism where the interface scattering rate plays a vital role. The interface scattering rates can be modified by using the following techniques:

- Modifying grain size
- Nanoscale precipitation and size distribution
- Nanocomposite volume fractions
- All-scale hierarchical architectures.

2.5.Engineering motivations for nanotechnology in thermal conductivity

- Thermal conductivity can be significantly reduced using nanotechnology because the mean free path of phonons is altered in lower dimensions (Figure: 2.4.1a-d).
- Thermal conductivity can be controlled significantly using nanotechnology through phonon scattering by engineering point defects and boundaries in composites
- Grain boundary engineering can significantly impact thermal conductivity performance, which is different from surface scattering.
- Adding impurities can impact thermal conductivity drastically.

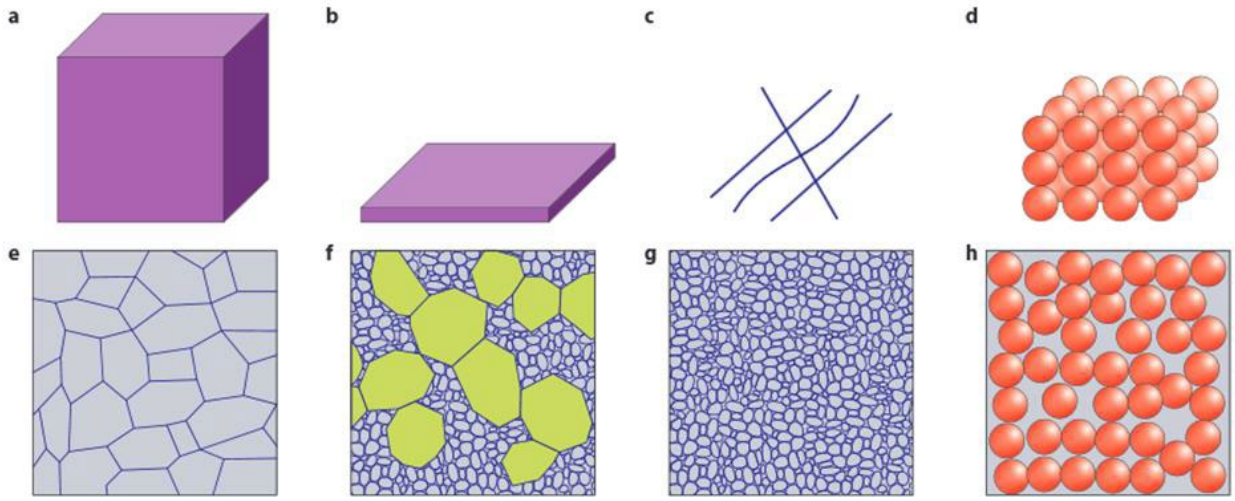

Figure 2.4: TE materials structure in different scales demonstrated in a nutshell. (a–d) Different dimensionalities: (a) bulk (3D), (b) thin film (2D-30nm), (c) nanowire (1D-100nm), (d) atomic cluster (0D-quantum dots). (e–h) variation of grain microstructures (e) micron sized grained only, (f) coarse and fine grained, (g) nanosized grained, (h) amorphous [26].

2.6.Models for the thermal conductivity of composite materials

As discussed in the previous section, introducing a second phase into a material to form a composite effectively modifies the thermal conductivity. This is a well-known strategy, and there are several mathematical models that describe the resulting thermal conductivity with varying levels of complexity. The following models allow one to calculate the effective thermal conductivity (κ) in composites, which are made of a fraction of a filler with thermal conductivity (κ_f) and a matrix with thermal conductivity (κ_m).

2.6.1. Law of Mixtures

According to the Law of Mixtures, the overall properties of composites or hybrid materials should depend on the weighted-average properties of the filler and matrix [27]. In materials science, the Law of the Mixtures is famous for often predicting various properties such as the elastic modulus, mass density, ultimate tensile strength, thermal conductivity, and electrical conductivity of composite materials [28].

The following equation is used to determine thermal conductivity in a composite

$$\kappa_c = \kappa_f V_f + (1 - V_F)\kappa_m \qquad 2.7$$

Where,

κ_c = Thermal conductivity of the composites.

κ_f = Thermal conductivity of the filler materials.

κ_m= Thermal conductivity of the matrix.

V_f = volume fraction of the filler materials.

$(1 - V_f)$= volume fraction of the matrix.

From Figure 2.5, it can be seen that the red line (which is calculated from the Law of Mixtures) can be used to approximately predict the thermal conductivity of the composites of Bi_2Te_3 and polyurethane. This graph indicates that the reduction of thermal conductivity of Bi_2Te_3-PU composites is reasonably well predicted by the Law of Mixtures, although the agreement is not

perfect. This shows that additional effects do occur and modify the conductivity of thermal composites, requiring sophisticated models beyond the simple Law of Mixtures.

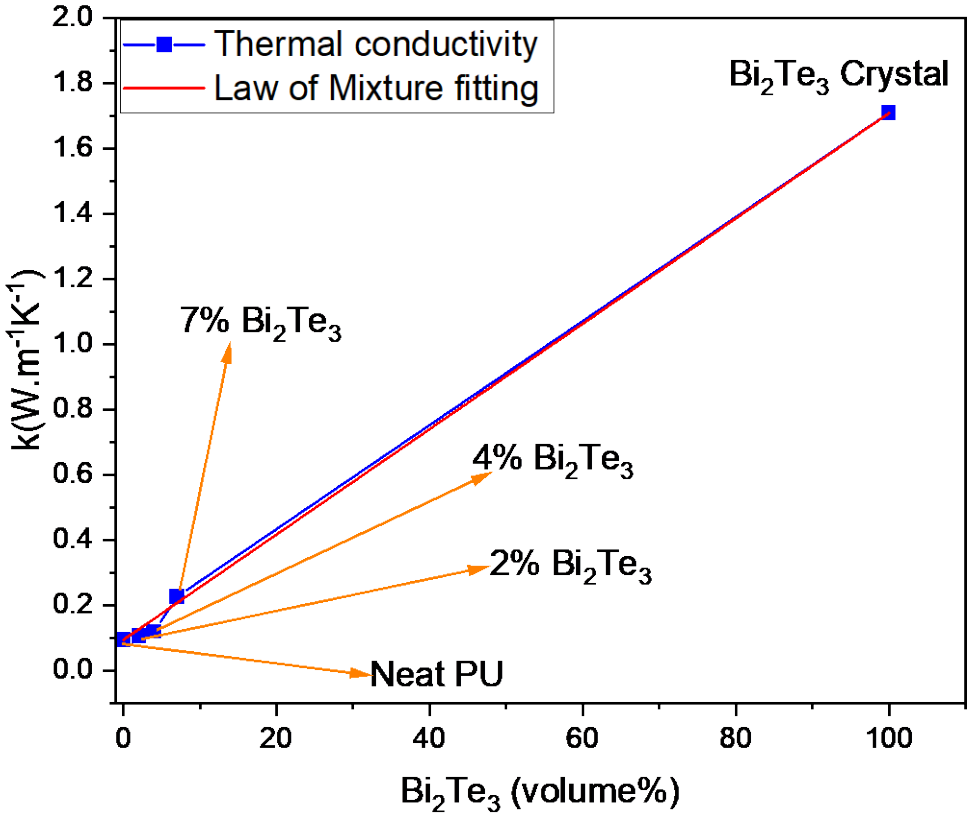

Figure 2.5: Law of Mixtures theory fitting curve with Bi_2Te_3-PU composites, neat polyurethane, and pure Bi_2Te_3 crystal.

2.6.2. Maxwell theory

Maxwell [29] was the first to derive a composite-based theory for electric potential's effective resistivity that satisfies the Laplace equation, and he used the same underlying mathematics to later model thermal composites. The far-field potential is given by initially considering a sphere with radius a_2, and electrical resistivity R_2 in an infinitely extended homogenous medium of electric resistivity R_1, as shown in (Fig. 2.6).

In terms of the condition that considering the sphere's centre as the origin, the first model of the spherical harmonics of the electric potential at a great distance is given by

$$V_\infty = \left(B_0 r + B_1 \frac{1}{r^2}\right) cos\theta \qquad 2.8$$

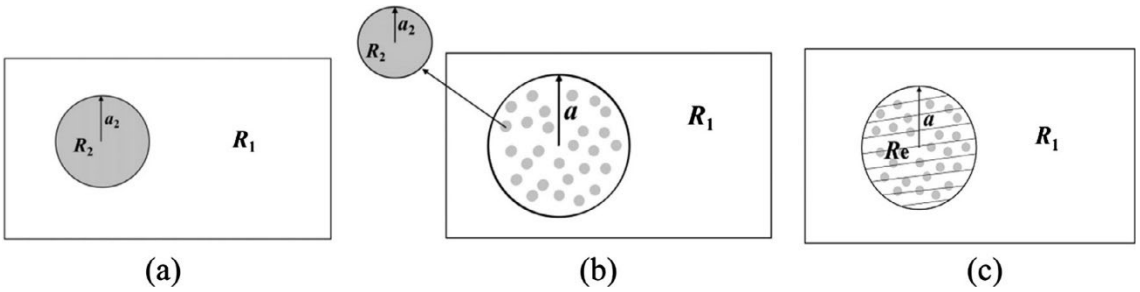

Figure 2.6: Far field potential for spherical shape

Where,

B_0 = Coefficient of the background potential associated with R_1,

B_1 = Coefficient of the potential induced by the sphere with R_2

B_1 is expressed by the following equation,

$$B_1 = \frac{R_2 - R_1}{2R_2 + R_1} a_2^3 B_0 \qquad 2.9$$

Then, Maxwell considered a large sphere with a larger radius and filled it with *n* spheres with radius a_2, as shown in Figure 2.6b. By following the linearity of potential theory, we can calculate the far-field potential B_n as follows:

$$B_n = \frac{R_2 - R_1}{2R_2 + R_1} \emptyset_s a^3 B_0 \qquad 2.10$$

Now, the system consists of *n* number of spheres, which each have an effective resistivity R_e with radius a_n, as shown in figure 2.6c, because of the resistivity of the system. By equating the modified equations, the effective resistivity R_e can be obtained as [29]:

$$R_e = \frac{2R_2 + R_1 + \emptyset_S(R_2 - R_1)}{2R_2 + R_1 - 2\emptyset_S(R_2 - R_1)} R_1 \qquad 2.11$$

The correlation between the electric potential and the temperature of steady heat conduction, Eq. (2.11), is also equally applied for thermal resistivity. In terms of thermal conductivity, $\kappa_1 = 1/R_1$, $\kappa_2 = 1/R_2$ and $\kappa_e = 1/R_e$, and denoting κ_1 and κ_2 by κ_f and κ_m, respectively, where the subscripts *f* and *m* refer to the first(filler) and second(matrix) phases of composites, Eq. (2.11) becomes [30]

$$k_e = \frac{2k_f + k_m + 2\emptyset_m.(k_m - k_f)}{2k_f + k_m - \emptyset_m.(k_m - k_f)}.k_f \qquad 2.12$$

This equation is frequently utilized by researchers studying heat transfer in composite materials. From equation 2.12, the materials' thermal conductivity and volume fraction are the two major factors for effective thermal conductivity. The model is still approximate as it contains no parameter to account for the interfacial particle effect, and thermal interactions between filler particles are ignored [31]. The schematic of such material is shown in Figure 2.7

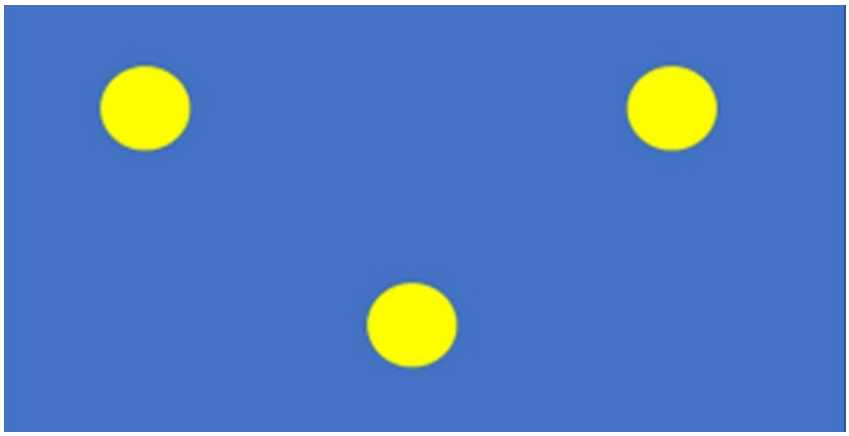

Figure 2.7: Representation of a secondary phase (yellow) embedded in a host matrix (blue)

Maxwell's expression is as follows:

$$\frac{k_{eff}}{k_m} = 1 + \frac{3\phi}{(\frac{k_f + 2k_m}{k_f - k_m}) - \phi} \qquad 2.13$$

Where,

ϕ = Volume fraction filler.

Maxwell's formula was found to be valid only for a low volume fraction of filler ($\lessapprox$ 25%). Several researchers modified the Maxwell formula under different circumstances later.

2.6.3. Rayleigh models

In the modification of the Maxwell formula regarding thermal conductivity, Rayleigh [32] considered the inclusion of the all-spherical material arranged in a simple cubic array embedded in a continuous matrix (See Figure. 2.8).

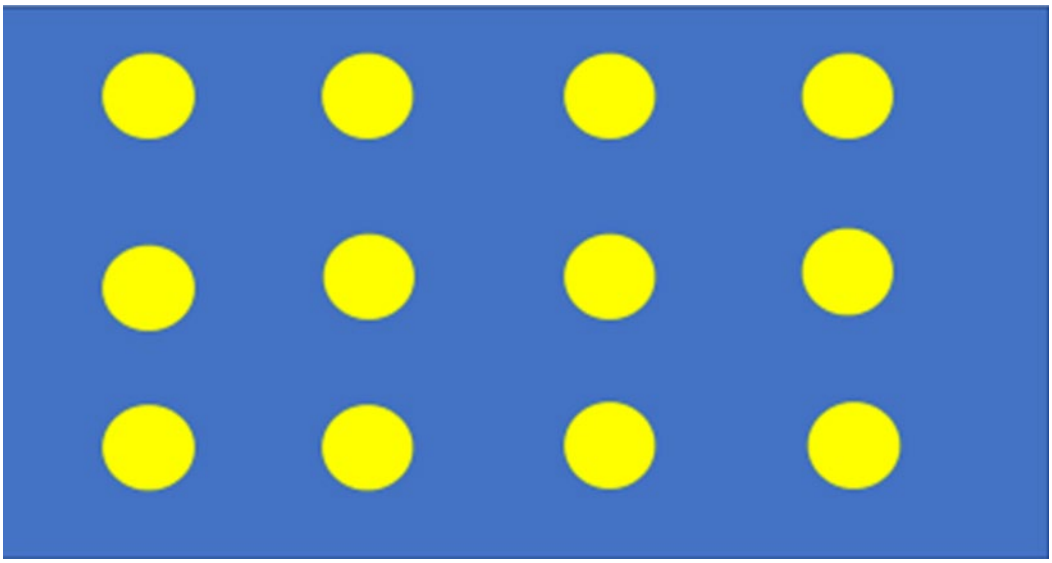

Figure 2.8: Spherical particles arranged in a simple cubic array embedded in a continuous matrix, as considered by Rayleigh

In his calculation, Rayleigh included the thermal interaction between particles in an effort to obtain a more accurate final result than the Maxwell equation, but the results from both formulas are similar. For higher volume fraction filler(ϕ), Rayleigh's formula is [33]:

$$\frac{k_{eff}}{k_m} = 1 + \frac{3\emptyset}{\left(\frac{k_f - 2k_m}{k_f - k_m}\right) - \emptyset + 1.569\left(\frac{k_f - k_m}{3k_f - 4k_m}\right)\emptyset^{\frac{10}{3}} + \cdots..} \qquad 2.14$$

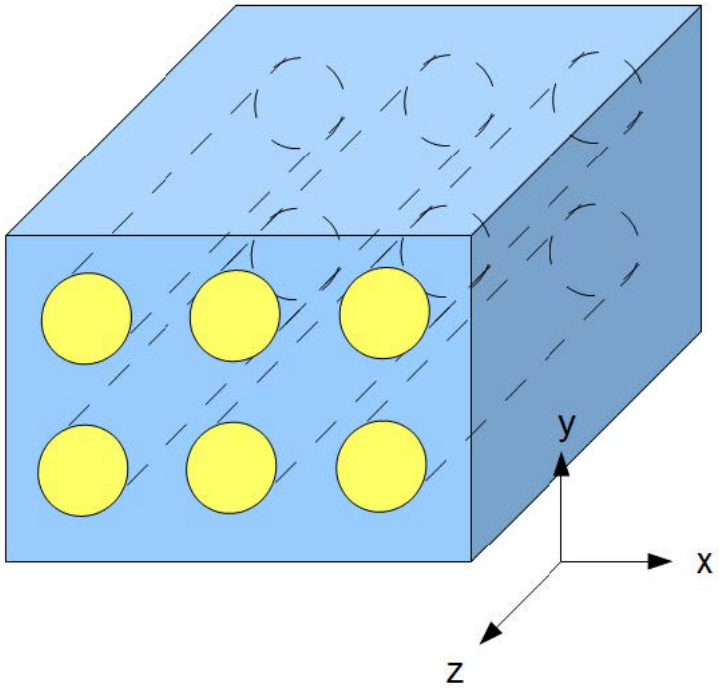

Figure 2.9: The schematic of the second type composite medium considered by Rayleigh, consisting of parallel cylinders embedded in a continuous matrix [34].

Nevertheless, an analytical expression is included by Rayleigh for effective thermal conductivity for different composites, where he considers a continuous matrix reinforcement with parallel cylindrical fibres forming a uniaxial cubic array (see Figure. 2.9).

Considering the z-axis parallel to the fibres, Rayleigh's formulae for thermal conductivity are given as follows, with directional dependence [33]:

$$\frac{k_{eff,ZZ}}{k_m} = 1 + \left(\frac{k_f - k_m}{k_m}\right)\emptyset \qquad 2.15$$

$$\frac{k_{eff,XX}}{k_m} = \frac{k_{eff,yy}}{k_m} = 1 + \frac{2\emptyset}{c_1 - \emptyset + C_2(0.3.584\emptyset^4 + 0.013363\emptyset^8 + \cdots)} \qquad 2.16$$

Where,

$$C_1 = \frac{k_f + k_m}{k_f - k_m}, \quad C_2 = \frac{k_f - k_m}{k_f + k_m} \tag{2.17}$$

2.6.4. Hasselman-Johnson model

According to Hasselman and Johnson, particle size is as crucial as filler volume fraction to improve effective thermal conductivity for composites materials [34]. Additionally, Hasselman and Johnson observed the influence of the interfacial gap between filler and matrix in Ni-glass composites on the thermal diffusivity and thermal conductivity [35]. Then, they tried to connect interfacial thermal resistance with their observations. Shortly after, they modified Maxwell and Rayleigh's models for effective thermal conductivity of composites materials with non-zero interfacial resistance [36]. Hasselman and Johnson insisted on the radius of a particle (a) and the boundary conductivity (h_c), which is the reciprocal of interfacial thermal resistance [37]. The authors derived expressions for a continuous matrix phase with dilute concentrations of dispersions with spherical (equation: 2.18), cylindrical (equation: 2.19), and flat plate (equation: 2.20) geometries. Equations (2.18) and (2.19) express the Maxwell equation's equivalent result for spheres and Rayleigh's result for cylinders perpendicular to the heat flow, where equation (2.20) indicates the perpendicular heat flow for flat plates dispersed in a matrix [36].

$$k_{eff} = k_m \frac{[2(\frac{k_f}{k_m} - \frac{k_f}{ah_c} - 1)\emptyset + \frac{k_f}{k_m} + \frac{2k_f}{ah_c} + 2]}{[(1 - \frac{k_f}{k_m} + \frac{k_f}{ah_c})\emptyset + \frac{k_f}{k_m} + \frac{2k_f}{ah_c} + 2]} \tag{2.18}$$

$$k_{eff} = k_m \frac{[(\frac{k_f}{k_m} - \frac{k_f}{ah_c} - 1)\emptyset + (1 + \frac{k_f}{k_m} + \frac{k_f}{ah_c})]}{[\left(1 - \frac{k_f}{k_m} + \frac{k_f}{ah_c}\right)\emptyset + \left(1 - \frac{k_f}{k_m} + \frac{k_f}{ah_c}\right)]} \quad 2.19$$

$$k_{eff} = k_m \frac{k_f}{[\left(1 - \frac{k_f}{k_m} + \frac{2k_f}{ah_c}\right)\emptyset + \frac{k_f}{k_m}]} \quad 2.20$$

2.6.5. Bruggeman model

Bruggeman proposed a model for many effective properties such as thermal conductivity, electrical conductivity, thermal diffusivity, magnetic permeability, and electrical permeability for heterogeneous materials, which Landauer later refined [38, 39]. The principal approach of the Bruggeman model is to assume composite materials are constructed by introducing infinitesimal changes that already exist in the materials. Because of this approach, this model is called the differential effective medium theory, or differential effective medium scheme (DEM).

Bruggeman's model covers a wide spectrum of materials such as composites, nanofluids, porous materials, aerosols, space dust, etc., which is considered the most valuable part of the model. This model also helps formulate equations for multi-component systems, especially for the classical case of two components. This model is the most accurate among classical effective medium theories (EMT) for high filler volume fractions. Every et al. [40] obtained an expression for effective thermal conductivity of composites by modifying Benveniste's result [41] and analysis from the Bruggeman model. Their formula is:

$$(1-\emptyset)^3 = \left(\frac{k_m}{k_{eff}}\right)^{(1+2\alpha)/(1-\alpha)} \left(\frac{k_{eff}-k_f(1-\alpha)}{k_m-k_f(1-\alpha)}\right)^{3/(1-\alpha)} \quad 2.21$$

Where α = dimensionless parameter depending on ITR between filler and matrix.

2.6.6. The Lewis-Nielsen model

The Lewis-Nielsen model is quite popular for filler volume fractions up to 40%, even though it doesn't include interfacial thermal resistance (ITR). This model becomes unstable at higher values [42]. Its simplicity and covering different materials of various shapes and patterns made this model famous and advantageous. According to the Lewis – Nielsen model, effective thermal conductivity is

$$k_{eff} = \frac{1+AB\phi}{1-B\phi\varphi} \quad 2.22$$

Where,

$$B = \left(\frac{\frac{k_f}{k_m}-1}{\frac{k_f}{k_m}+A}\right) \quad 2.23$$

$$\varphi = 1 + \left(\frac{1-\phi_m}{\phi_m^2}\right)\phi \quad 2.24$$

Here,

κ_m = Thermal conductivity of the matrix,

κ_f = Thermal conductivity of the filler,

ϕ = Filler volume fraction,

ϕ_m = Maximum filler volume fraction

A = Shape co-efficient for the filler particles

2.6.7. Percolation model

When the amount of filler per unit is increased, the composites reach a point when filler particles begin to contact each other. Heat transfer then becomes easier between the particles and the matrix for high conductive fillers. With an increasing amount of filler, the fillers create chains that act as heat conduction channels. As a result, the effective thermal conductivity of the materials increases significantly. This is termed the percolation threshold. The term percolation was originally reserved to describe passing a liquid through a porous medium or small holes, but later its meaning was expanded to describe the phenomenon of formation of conducting channels in many types of transport problems, e.g., electric circuits, public transport or the spread of disease. The example of percolation in composite material is schematically presented in Figure: 2.10, where a chain of highly conductive filler particles enhances heat transfer between the heat source and the heat sink.

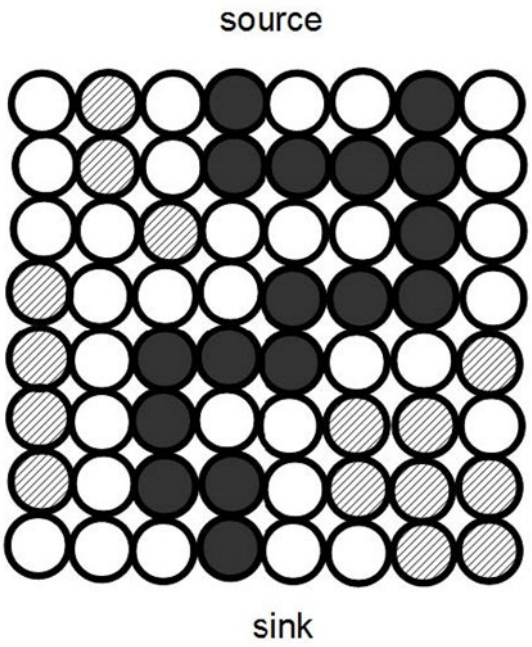

Figure 2.10: A schematic illustration of enhanced heat transfer in a particulate composite material due to percolation. High-conductivity particles, forming a continuous conductive chain from source to sink, are depicted as black. White is for low-conductivity particles, and hatching is for high-conductivity particles which do not form a continuous chain from source to sink [34].

As effective medium approximations such as those described in Sections 2.6.2-2.6.6 are unable to predict the properties of a multiphase medium close to the percolation threshold, numerical simulation is one of the most promising ways to model percolation effects in thermal composites.

2.6.8. Dynamic methods

In extremely high-temperature applications such as the aerospace and automotive industries, non-steady heat flux and extremely high temperature are expected. Modelling such states is rather complex, and therefore, to date, few approaches involving non-steady effective thermal properties have been made. Monde and Mitsutake [43] developed a method using an analytical inverse solution to determine the thermal diffusivity of solids for unsteady heat conduction. In another study, Fang [43] used a combination of a quasi-crystalline approximation and the Percus–Yevick correlation function to investigate the propagation of a thermal wave in matrix composite materials with high volume concentrations of particles.

Fang et al. investigated the unsteady effective thermal conductivity of particular composites with a functionally graded interface and applied the thermal wave method in 2009 [44]. Coated particles were present in the solution they used to analyse the non-steady effective thermal conductivity of the composites [44]. The wave function method was employed to analyse the thermal scattering

waves in those composites. The validation of the dynamic model is often demonstrated by comparison with the steady-state effective thermal conductivity.

2.7.Review of materials explored in the thesis

Using the strategies and methods outlined in Section 2.3 – 2.6, this thesis explored methods to modify the thermal conductivity in several different materials and composites. The sections below briefly review the materials and compounds which were investigated for thermal engineering in this work.

2.7.1. Chalcogenide compounds

A compound with an element from group 16 is called a chalcogenide compound [45]. PbTe, PbS, and PbSe are well-known chalcogenide thermoelectric compounds that maintain the rock salt crystal structure. Bi_2Te_3 and MoS_2 are other thermoelectric chalcogenides with hexagonal crystal structures [46, 47]. Chalcogenide compounds possess high melting points, higher air stability, congruent melting behaviour, and semiconductors. Chalcogenide compounds are also popular for their ability to adapt to other elements, as inorganic thermoelectric devices and as an additive component in thermal polymer composites for a wide range of temperatures.

2.7.2. Bismuth Telluride (Bi_2Te_3)

Bi_2Te_3 has become a prominent candidate for thermoelectric applications. This semiconductor material is considered a promising candidate in the range of 200 K to 400 K thermoelectric applications.

Bi_2Te_3 compound possesses a hexagonal crystal structure. As shown in Figure:2.11, van der Waals interactions bonds along with the c-axis play an important role in stacking five atomic layers (Te1-Bi-Te2-Bi-Te1) [48].

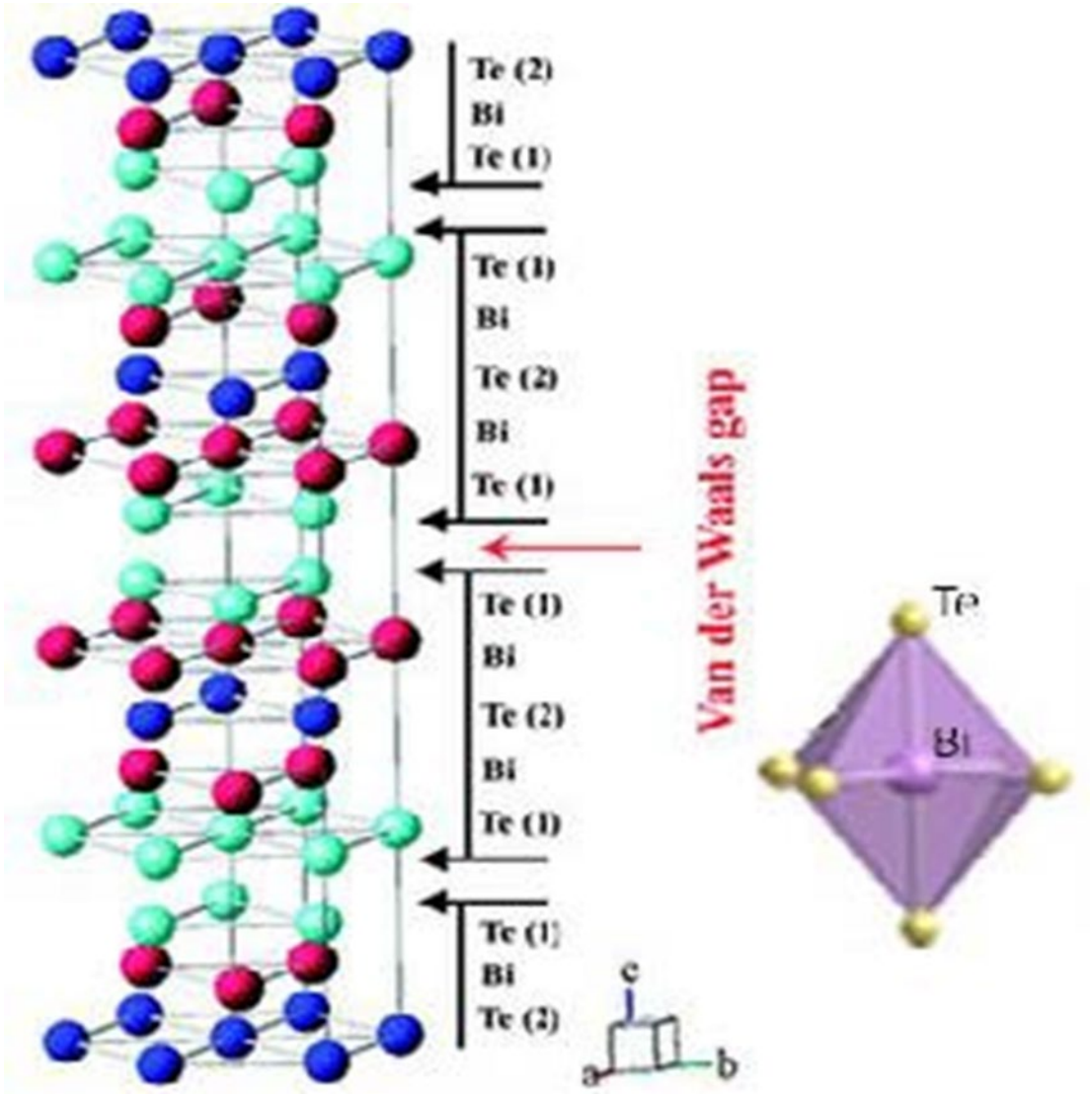

Figure 2.11: Bismuth Telluride (Bi_2Te_3) crystal structure [49]

Several secondary phases such as ZnTe [50, 51], ZnO [51], Zn_4Sb_3 [52], carbon nanotubes [53], graphene [54], metallic particles [55] etc. have been explored individually for incorporation into Bi_2Te_3-based materials to improve its thermoelectric performance by reducing thermal

conductivity. Moreover, Bi_2Te_3 has also been a promising component to add thermoplastic polymers to form nanocomposites. For example, Zhang et al. [56] have incorporated both n and p-type Bi_2Te_3 into commercialized PEDOT: PSS products to improve thermal conductivity by using ball mailing methods.

2.7.3. Copper Selenide (Cu_2Se)

Cu_2Se is well-known for semiconducting applications such as solar cells, photocatalytic applications, thermoelectric applications, and energy conversion. It has a bandgap (1.2 eV) [58] as a chalcogenide-based TE material. Additionally, it has a relatively high melting point (1113°C), higher effective mass, higher mechanical strength, and small hole mobility [59, 60].

Cu_2Se changes its crystal structure at 400 K. At room temperature, it possesses a monoclinic crystal structure (Figure: 2.12), but it turns into a cubic structure above the phase transition at 400 K (Figure: 2.13). As in other semiconductors, the motion of the atoms is primarily responsible for carrying heat in Cu_2Se. The vibration of atoms in the crystal and their amplitudes increase with temperature. Longitudinal and transverse waves are two collective atomic vibrational modes that carry heat (Figure: 2.14).

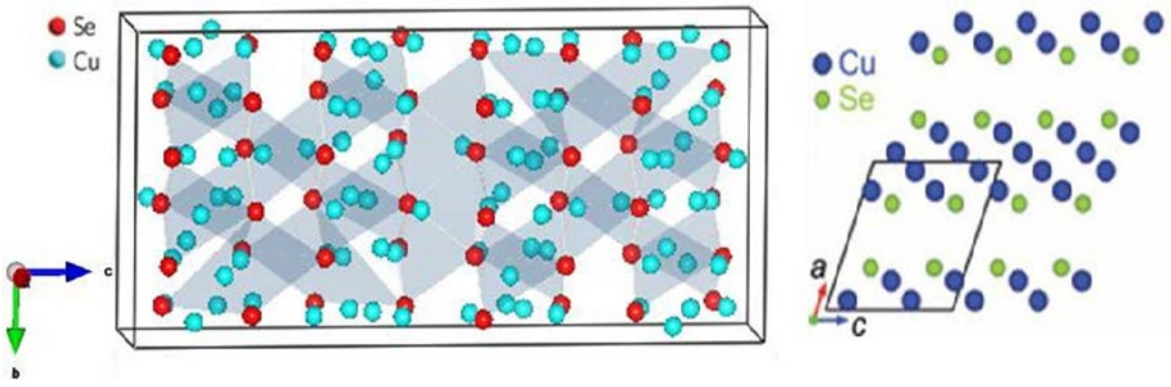

Figure 2.12: Sextuple layers of Se-Cu-Cu-Cu-Cu-Se form a repeating motif in the low temperature monoclinic Cu_2Se phase [61]

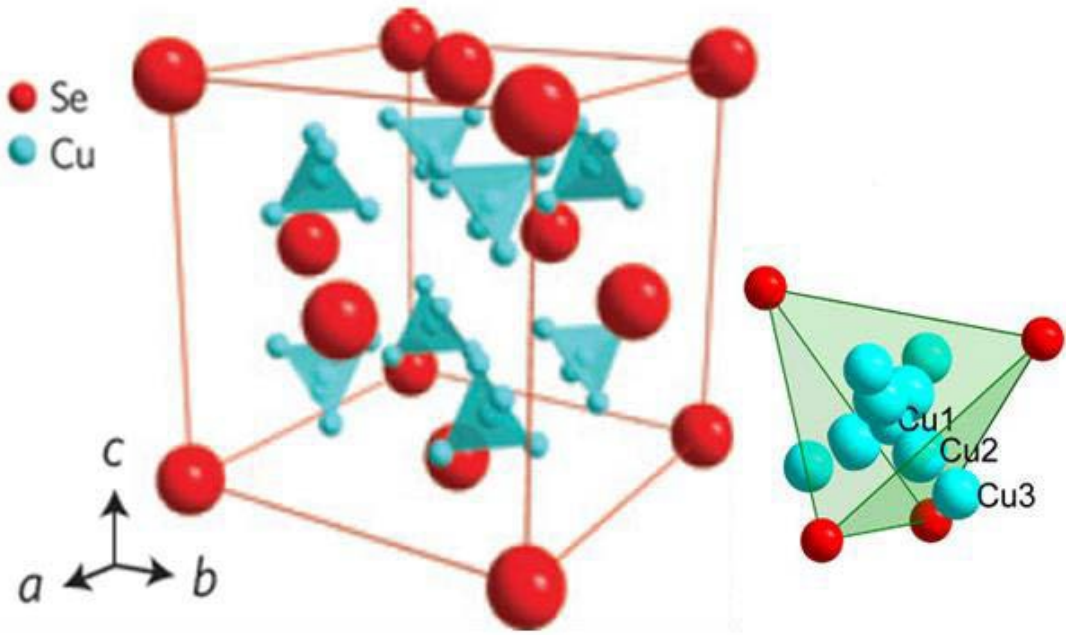

Figure 2.13: Cu_2Se cubic (β-phase) unit cell at high temperatures above 400 K [62]

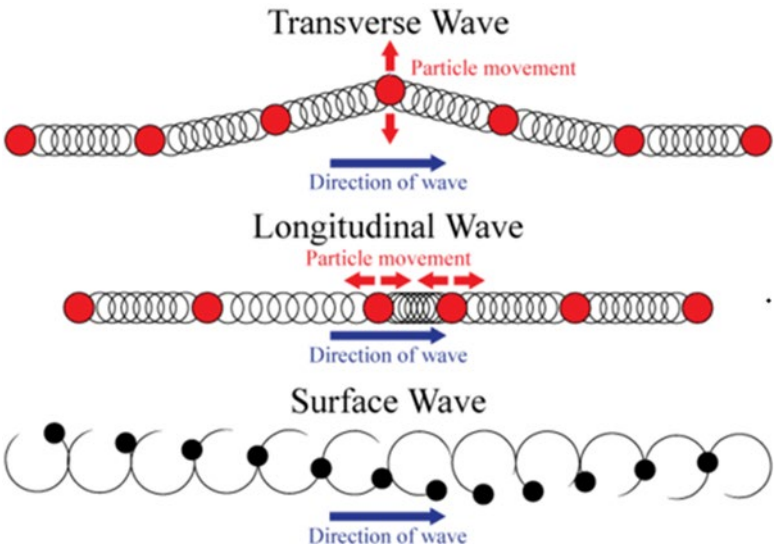

Figure 2.14: Transverse and longitudinal waves (source CK-12 foundation.com)

The interaction between adjacent atoms is the main cause of transverse waves travelling in a solid material. In the case of transverse waves, adjacent atoms move with up and down motions, and

waves propagate perpendicularly to that motion. However, transverse waves do not propagate well in liquids due to the weak bonding between neighbouring atoms.

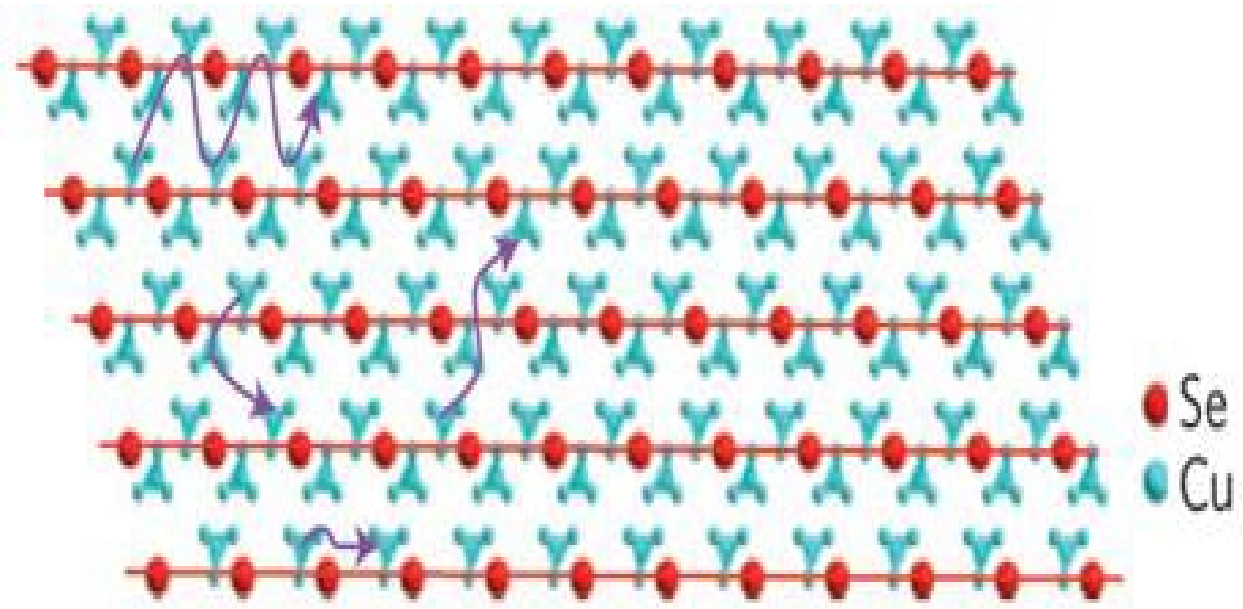

Figure 2.15: The arrows indicate that the Cu ions can freely travel among the interstitial sites in the $Cu_{2-x}Se$ compound, which has a cubic antifluorite structure [63]

Due to the free-flowing copper atoms in Cu_2Se, which have liquid-like characteristics in the high-temperature superionic state, it was initially proposed that transverse waves cannot propagate in Cu_2Se, leading to a reduced thermal conductivity (Figure: 2.14). Recently this point has been examined using neutron spectroscopy [64], and the conclusion is that transverse waves survive in the liquid-like state. It was argued that other mechanisms play a more critical role in the reduced thermal conductivity, including:

- Ultra-low energy optical modes with a low group velocity
- Very strong three-phonon Umklapp scattering from the anharmonic lattice
- Defective crystal structure in the cubic state which naturally forms vacancies and other imperfections

- Dislocation Scattering
- Boundary Scattering
- Point defect scattering

In recent years, the addition of a substitutional element or nanocomposite in Cu_2Se has also become a common trend to reduce thermal conductivity to enhance thermoelectric performance. Examples of 0D dopants in $Cu_{2-x}Se$ include Ag, [65, 66] Sn, [67] In, [68, 69] I, [70] B, [71] Fe, [69] Ni, [69] Mn, [69] Zn, [69] Sm, [69] Li, [72] S, [73] Te [74] and Na [75-77] have been added over the years. Additional graphene, carbon nanotubes and other additives have been investigated for composite formation in Cu_2Se [78]. There has also been increasing interest in using magnetic dopants in thermoelectric phases in recent years, although this approach has not been widely used in Cu_2Se to date [79, 80].

2.8.Magnetic nanoparticles (Fe_3O_4)

2.8.1. Structure of Fe_3O_4

The two major forms of iron oxide are Fe_3O_4 (magnetite) and γ-Fe_2O_3, an oxidised form is known as maghemite. Additionally, another common structure of iron oxide is known as hematite (α-Fe_2O_3). These iron oxides can form nanoparticles on the scale of 1 to 100 nm in diameter.

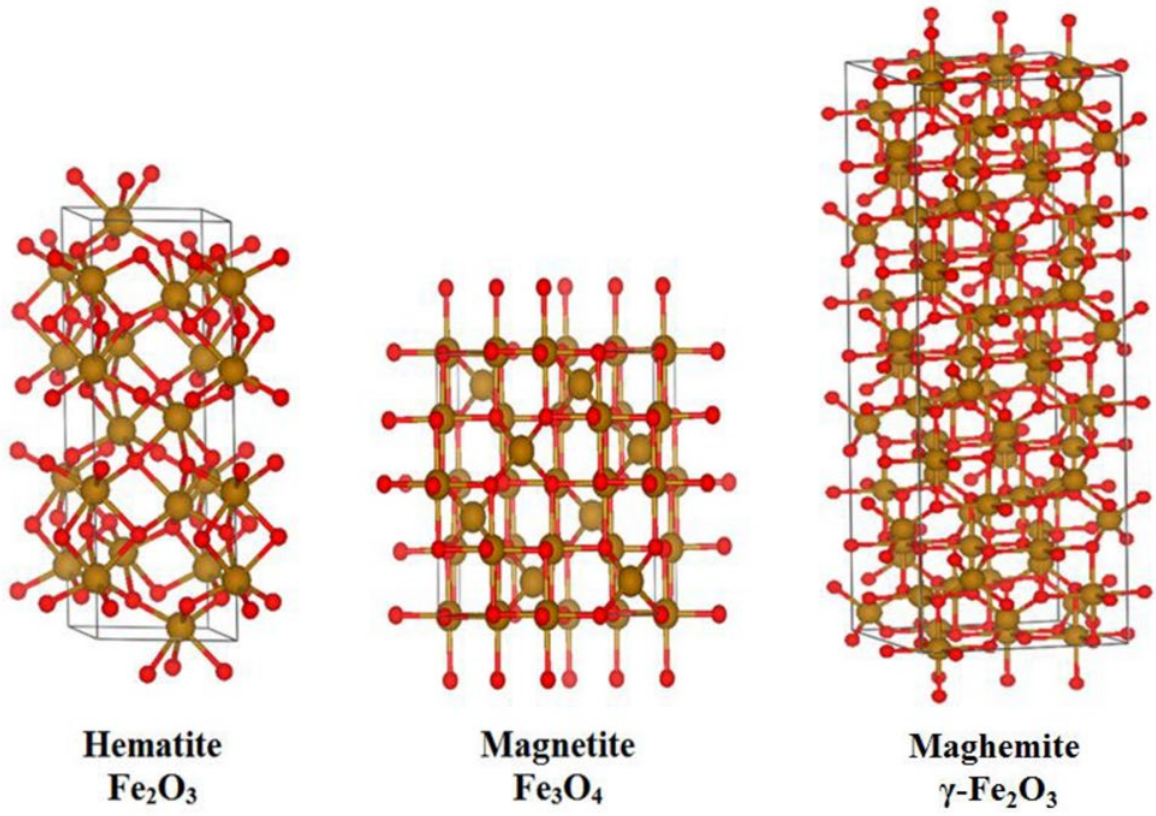

Figure 2.16: Possible crystal structures of superparamagnetic iron oxide nanoparticles [81]

Fe_3O_4 has biocompatibility, good magnetic performance, structural stability, and other promising characteristics. Due to this behaviour, this material is considered the best candidate for biomedical applications, including magnetic resonance contrast agents and hyperthermia treatments [82]. Magnetite behaves like a half-metallic ferromagnet at room temperature because its electrons are 100% spin polarised.

The unit cell of magnetite consists of 24 Fe atoms; among them, eight atoms are tetrahedrally coordinated (Fe^{3+}), whereas the other 16 atoms are octahedrally coordinated ($Fe^{2.5+}$) (Figure 2.16). In the magnetite structure, oxygen atoms are assumed to be non-magnetic, but they mediate super-exchange interactions between the Fe sites.

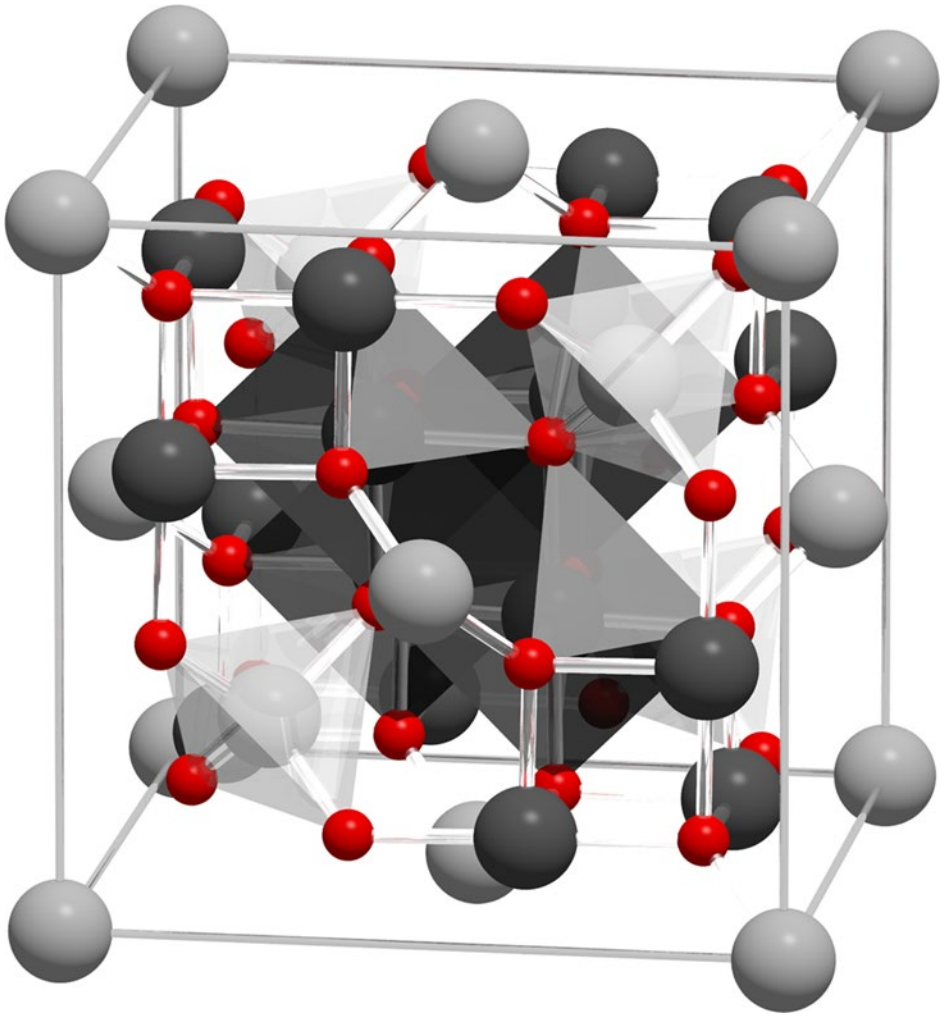

Figure 2.17: Visualization of the magnetite (Fe_3O_4) unit cell identifying octahedral $Fe^{2.5+}$ (dark grey), tetrahedral Fe^{2+} (light grey) and oxygen (red) sites. Octahedra and tetrahedra show the local site symmetries around fully coordinated Fe sites within the unit cell [83].

2.8.2. Thermal properties of magnetic nanoparticles(Fe_3O_4)

Magnetic nanoparticles (MNPs) of Fe_3O_4 possess three types of transitions driven by temperature;

1. **Verwey temperature:** The Verwey transition temperature ranges between 0 K and 119 K. Between 0 K to 119 K, magnetic nanoparticles (Fe_3O_4) transform between a metallic and semiconducting state [84].
2. **Curie temperature:** The Curie temperature ranges from 120 K to 840 K in MNPS [84]. Below the Curie temperature, the MNPS are ferromagnetically ordered and possess a strong magnetic response.
3. **Paramagnetic metal:** This phase appears above the Curie temperature when the MNPs behave like a paramagnetic metal with a weak magnetic response [84]

The thermal properties of MNPs carry significant importance due to their wide range of applications in biomedical fields, especially in magnetic hyperthermia therapy (MHT). MNPs create two distinct curves during magnetization vs temperature cycling, known as zero-field cooling (ZFC) and field cooling (FC). With heating, the magnetic moment starts increasing and then decreases after a certain point in ZFC, called the blocking temperature. Due to being biomedically approved by the FDA and its semiconducting behaviour at a lower temperature, Fe_3O_4 is an attractive candidate for achieving both hyperthermia or targeted heating from magnetic induction and producing smart polymer composites with modified thermal and magnetic properties.

Chapter 3: Methods

3.1.Materials fabrication

Sample fabrication has been done by following two different methods. For the study on the addition of Na_2CO_3 into Cu_2Se, samples were fabricated by the melt solidification technique discussed in Section 3.1.1. For the study of thermoelectric/magnetic phases embedded in polyurethane (Chronoflex), synthesis was done using a solvent-based processing method as discussed in section 3.1.3. In some cases, to prepare nanoparticles (Bi_2Te_3), a simple liquid-phase exfoliation method (section 3.1.2) was deployed before conducting the solvent-based processing method.

3.1.1. Melt solidification technique

Initially, raw materials were mixed by using a mortar and pestle. Then, the well-mixed powder was made into pellets in a stainless-steel die with a hydraulic hand pump. After that, the pellets were sealed using an evacuated quartz tube using an oxyacetylene flame (Figure: 3.1). A vertical mosilli furnace (Figure: 3.2) was then used to heat the samples above their melting point. The copper selenide powders were heated to above 1200℃ with a heating rate of 10 K/min, followed by a furnace cooling to room temperature.

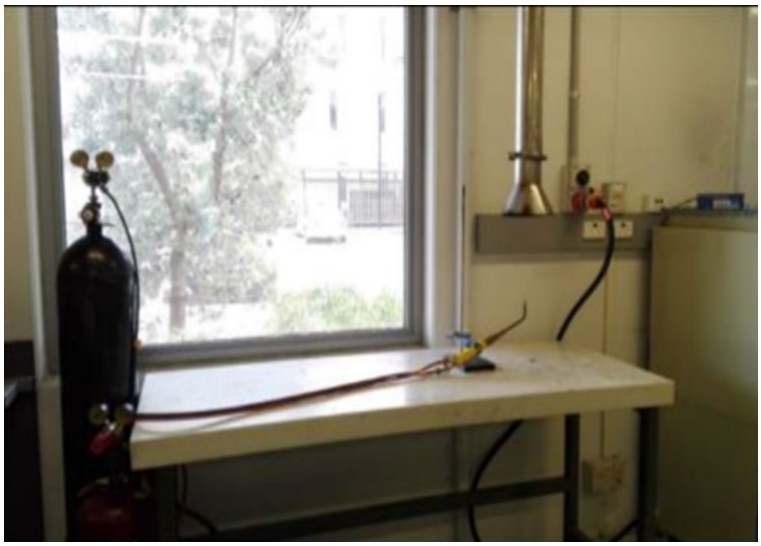

Figure 3.1: Oxyacetylene flame

Figure 3.2: Vertical mosilli furnace

3.1.2. Liquid phase exfoliation and solvent-based method for thermoelectric: polymer thermal composites

Firstly, the raw Bi_2Te_3 flake (0.24g, 0.6g, 1g) was ground with a mortar and pestle with 10ml (for each time) n-methyl-2-pyrrolidone (NMP). Then the ground Bi_2Te_3 bulk powder was sonicated with 20ml (for each sample) NMP for 10 hours in an ultra-sonicated bath. After sonicating the sample, it was heated at 70-degrees to obtain a dry nanopowder. Finally, the dry Bi_2Te_3 was ground again for 10 minutes with a mortar and a pestle.

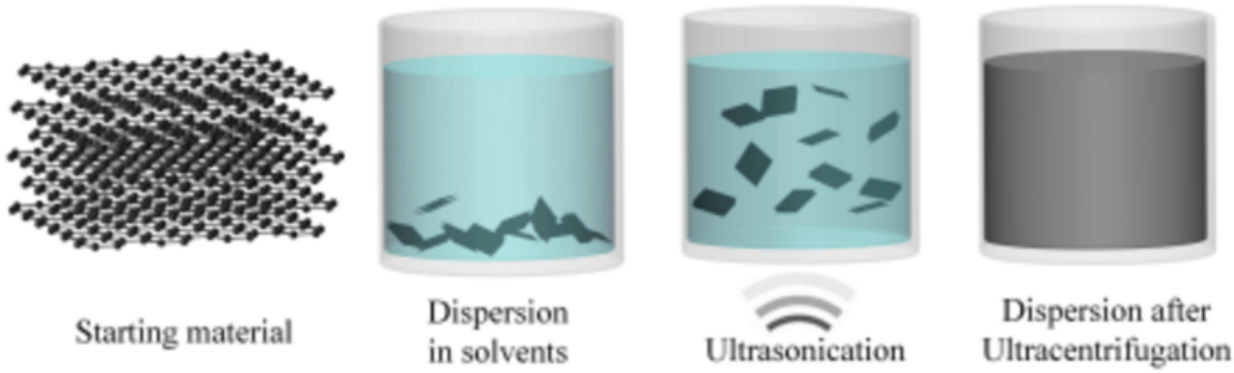

Figure 3.3: Schematic diagram of liquid phase exfoliation [85]

The exfoliated (0.24g, 0.6g, 1g) Bi_2Te_3 was transferred into a glass bottle with (20ml, 20ml, 20ml) tetrahydrofuran (THF), and similarly, 2g polyurethane in 30ml THF solution was also prepared in three separate glass bottles. They were ultra-sonicated for 6-8 hours, and then the Bi_2Te_3+THF and polyurethane+THF solution were mixed in one glass bottle. Finally, the mixture was sonicated for 4 hours. The sonicated hybrid solution mould by pouring it into a petri dish. The THF solvent was evaporated via airflow over the dish automatically.

3.1.3. Solvent-based processing method for magnetic: polymer thermal composites for induction heating applications

Fe_3O_4 nanopowders were weighed (7%, 10% and 13%) and dispersed in glass bottles with 20ml THF. The PU pellets were placed in separate glass bottles with 30ml THF. The solutions were sonicated for 6-8 hours. When the PU pellets and Fe_3O_4 nanopowders were dispersed properly, the two solutions were mixed into one glass bottle. The resulting mixture was sonicated for an additional 4 hours to ensure that the Fe_3O_4 nanopowder was dispersed uniformly into the solution. Finally, the sonicated composite solution was cast moulded by pouring it into a petri dish, and the THF solvent evaporated via airflow over the dish, ultimately resulting in Fe_3O_4: PU composite flexible films.

3.2.Characterisation techniques

3.2.1. Thermal diffusivity by laser flash analysis

This research project focused on using the laser flash analysis technique to measure the synthesised materials' thermal conductivity. LFA has several advantages: the high-temperature range, compatibility with small specimens, fast measurements, and accuracy at high temperatures. The details of the sample preparation and data analysis are discussed below.

3.2.2. Experimental details

The Linseis LFA -1000 (Figure: 3.4) apparatus was used to investigate the thermal properties of the manufactured samples. The measurement was conducted between 25° to 700° for Na_2CO_3-Cu_2Se compounds, whereas Fe_3O_4-PU and Bi_2Te_3-PU composites were analysed at room temperature. Fabricated samples were cut into a thin circular shape and placed inside the instruments using graphite sample holders. I have measured a standard graphite sample during

each measurement to compare with the actual specimen to get the best fitting data and accuracy of experiments. The instrument settings were configured at 300V laser energy during the experiments when Iris was 1, and the amplifier was 200. I have used a combined fitting model at room temperature to achieve accurate fitting. Liquid N_2 was used to cool a silicon detector during the thermal diffusivity experiments; instruments were repeatedly checked.

Figure 3.4: Linseis Laserflash - LFA 1000 [86]

3.2.3. Background and methods

3.2.3.1. Principle of the measurements

Laser flash analysis is a common method for measuring the thermal diffusivity of composites and highly thermally conductive materials. This experimental method uses a short duration radiation energy pulse to illuminate a high-density sample. A laser lamp or a flash lamp can be used as a power source. The specimen absorbs energy which is emitted again from the top side of the sample. The temperature rise is from the radiated energy of the specimen, and it is recorded by an infrared (IR) detector.

The laser flash analysis method detects the increase in temperature over time from the back face of a thin disk sample. The temperature increases on the back of the sample because of a short energy pulse on the front surface of the sample. A 10 mm diameter sample with 1-5 mm thickness is usually placed in the vacuum furnace using a graphite sample holder.

A high-speed detector collects data representing the temperature rise in the sample through a temperature-time curve that considers the sample thickness. This temperature-time curve is known as a thermogram (Figure: 3.6).

The temperature rise at the sample surface is typically normalized, and a detector signal expresses the duration of the measurements. The determination of the baseline and maximum temperature rise time is essential to calculate the thermal diffusivity of any sample.

Using sample thickness, L, and the half-time rise, $t_{1/2}$, a basic formula can calculate thermal diffusivity.

$$\propto = 0.1388 \frac{L^2}{t_{1/2}} \quad 3.1$$

The physical model of the thermal behaviour of an adiabatic slab with constant sample thickness can be explained by this formula, assuming a constant temperature with a short energy pulse. In some cases, the deviation from the simple formula is considered by extending the model to include the effect of the finite pulse length and heat loss from the sample to the environment or radial heat loss across the sample face (for a large sample).

By knowing the density and the specific heat capacity of the sample, the thermal conductivity can be calculated with the following equation:

$$\kappa(T) = \propto (T) \times C_P(T) \times \rho(T) \quad 3.2$$

Where,

κ = thermal conductivity

ρ = density of the specimen

C_P = heat capacity

$\propto$ = thermal diffusivity

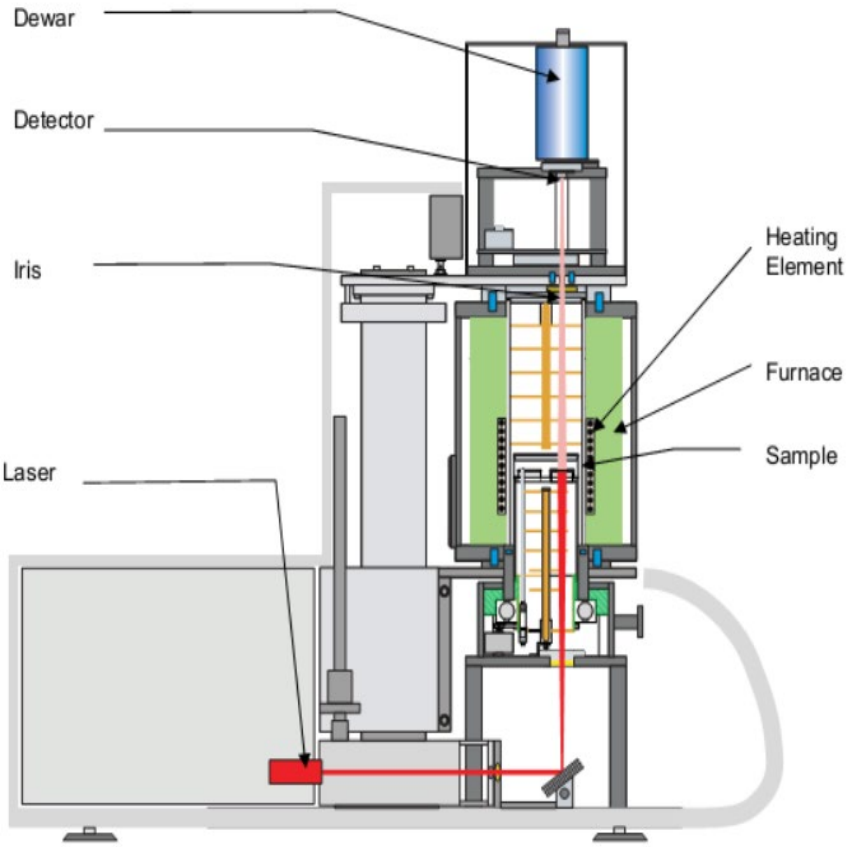

Figure 3.5: Schematic illustration of the Linseis LFA 1000 thermal diffusivity instrument showing the operation in the vertical mode

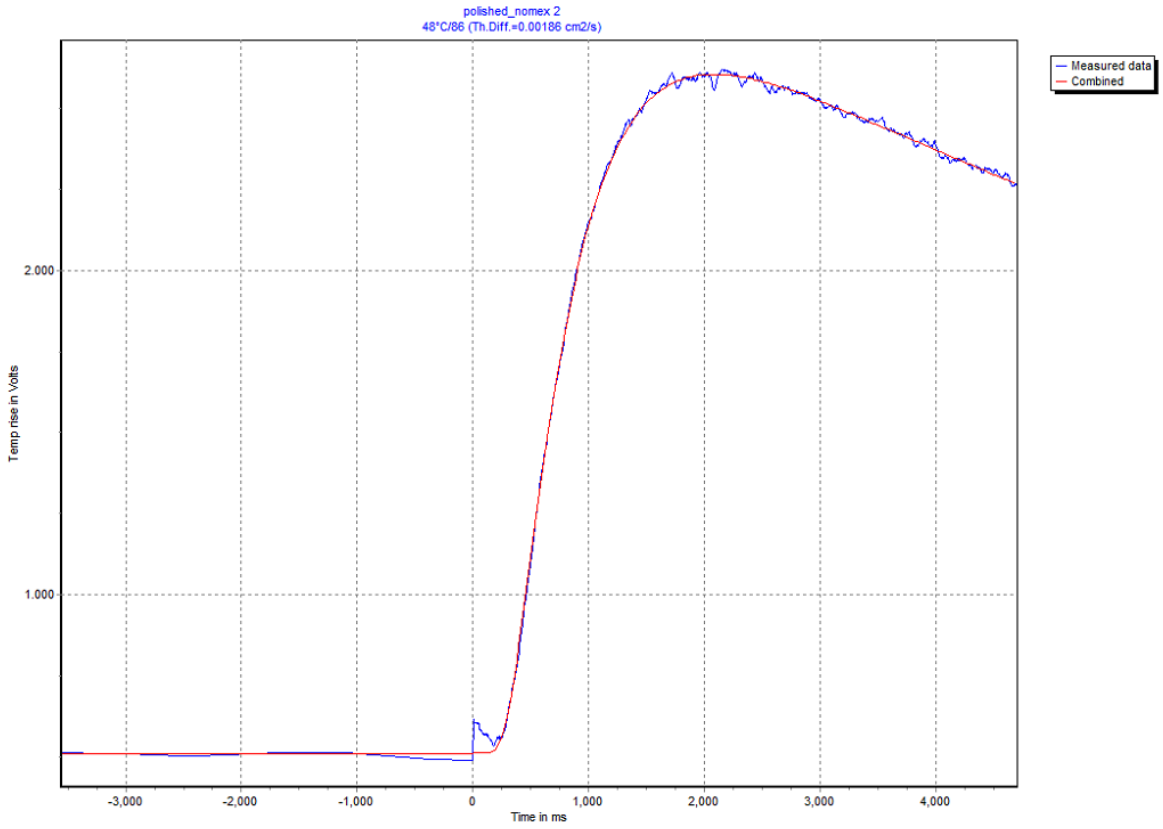

Figure 3.6: Nomex thermal diffusivity measurement (thermogram).

The sample is first heated using a second furnace element to measure a series of temperatures until an isothermal state is reached at the target temperature. After reaching the target temperature, a short laser passes through the specimen. As discussed previously, the additional temperature rise of the opposite sample surface is determined by an IR detector (Figure: 3.7).

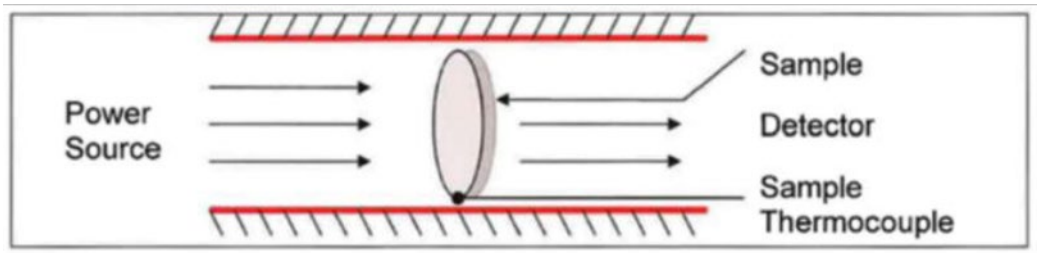

Figure 3.7: Schematic diagram illustrating the determination of thermal diffusivity.

3.2.3.2. Methods for fitting data in laser flash analysis

Thermal diffusivity measurements are usually analysed mathematically from a thermogram based on one of several possible models.

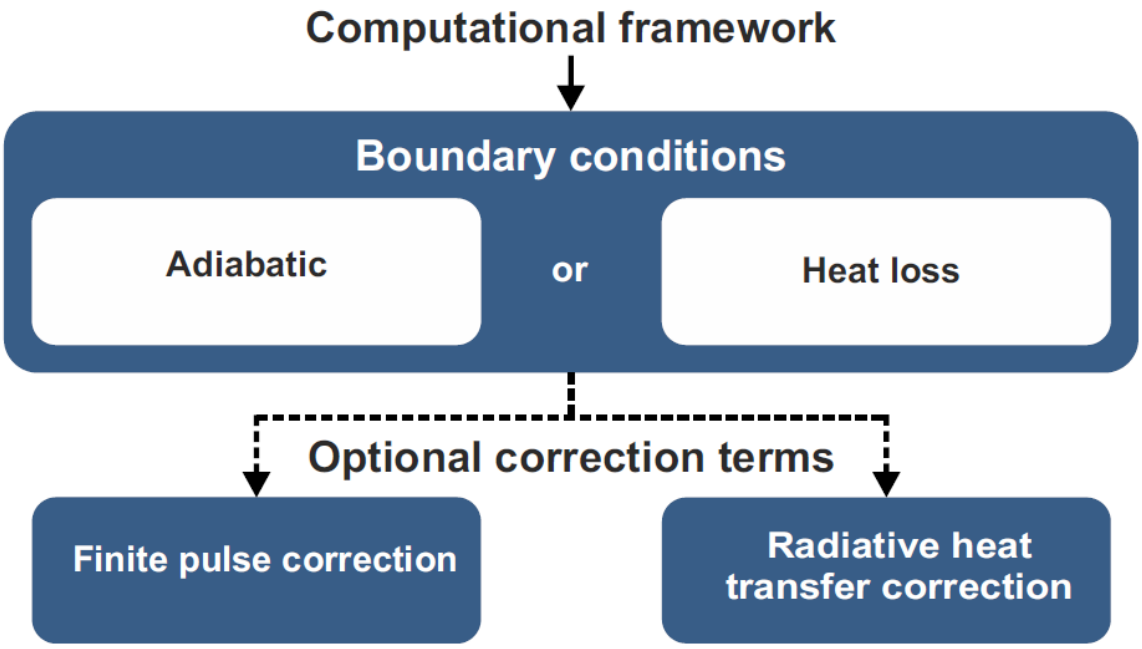

Figure 3.8: Flow chart of different laser flash analysis fitting methods incorporating optional corrections for different physical effects [87].

In my experimental analysis, I have focused on the standard methods described in the sections below.

1. Heat loss method

The heat loss method is used to measure the temperature difference between two faces of the sample by IR detector to measure any fabricated solid sample's thermal diffusivity. Unlike the simple adiabatic approximation in Equation 3.1, the heat loss method also considers the ambient

heat loss to the sample environment. Heat loss of the sample boundary can be analytically evaluated by B_{iot} numbers referring to each face of the analytical sample: $B_{i_0} = h_e/\kappa$,$B_{i_e} = h_e e/\kappa$, and $B_{i_r} = h_r r_s/\kappa$, with h_0, h_e, and h_r respectively heat transfer coefficients for the front, rear, and lateral faces.

The transient temperature is

$$T(t) = T_{lim} \sum_{n=1}^{\infty} A_n(Bi_0, Bi_e) \sum_{m=1}^{\infty} B_m(Bi_r) \exp\left[-\left(u_n^2 + w_m^2 \frac{e^2}{r_s^2}\right)\frac{at}{e^2}\right] \qquad 3.3$$

where, A_n, B_m, U_n and W_m are approximate terms defined in Ref [88]. Regarding the heat loss method, there is a significant difficulty differentiating the quantitative evaluation of heat exchange between the sample and the environmental heat loss, which may have conductive and radiative characteristics [89]. The higher the temperature of the analytical sample, the higher the risk of losing heat to the environment. In other words, a significant amount of heat can be lost from the sample surface during higher temperature measurements requiring the heat loss method for accurate results [90]. On the other hand, the adiabatic approximation could be acceptable at room temperature.

2. Finite pulse method

The finite pulse method improves on the simple adiabatic model to include the effect of the short pulse length. This is important for samples with high thermal diffusivity where the rise time may be comparable with the pulse length. This is developed based on two steps: [91]

1. Adjust the effective irradiation time by using the centre of gravity of the pulse.

2. Correcting the parameters from the ideal value of 0.1388 (equation 3.1)

From the following equation, it is possible to calculate the rear-face temperature vs time by using the following model:

$$T(t) = \frac{\int_0^t \emptyset(t')T_\delta(t-t')dt'}{\int_0^\infty \emptyset(t')dt'} \qquad 3.4$$

Here,

$\phi(t)$ = Shape of the pulse

T_6 = Heat conduction

$T(t)$ = rear face temperature

Instantaneous pulse sources can be easily described using equation 3.4, Where $t = t'$ is the origin of shifted time [88]. The most common pulse shape for this model is square [88, 92], sawtooth [92], or triangular [93-95].

Compared with other models, the main advantage of this method is that the applicable temperature range will exceed 1000°C, considering measuring time and sample size [95]. The finite pulse model will take longer to observe temperature changes (front and back phase temperature) at the rear face of the sample, and this model provides less accuracy of fitting than the combined model [96, 97].

3. Combined method

The combined model is unique for Linseis and is used in most cases as a fitting function in this thesis. This model is more reliable than any other model, and it gives a more correct than the

adiabatic, finite pulse, and heat loss models. The significance of the model is that no operator choice between the different models and correction is necessary, and the fit can be checked by plotting the model curve. Heat loss and finite pulse are effects that lead to deviations from the ideal heat transport assumed in the general working principle. In contrast, Combined means that it takes both effects (finite pulse and heat loss) into account during the correction technique.

Figure 3.9 is a fitting example between the heat loss and the combined models. The figure shows that fitting is not perfect enough with the heat loss model during sudden temperature rise. On the other hand, the unique combined model can adjust the curve fitting maximum even in sudden temperature rises.

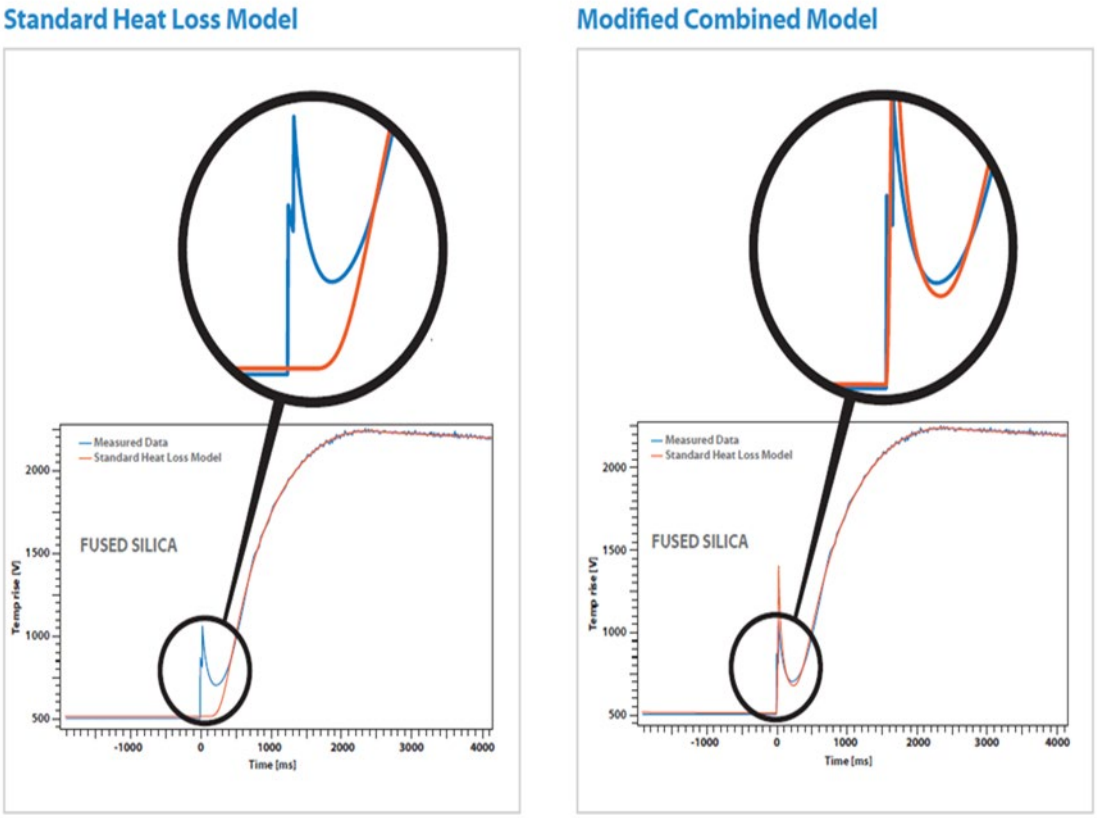

Figure 3.9: Fitting comparison between the heat loss model and combined model.

For a translucent sample, the temperature rise at early times in the graph is generated by induced optical energy in the pulse, which is radiatively transferred, which causes an immediate signal increase in the detector. The initial signal may distort the measurement resulting in an incorrect high thermal diffusivity being determined. For example, the heat loss model cannot sufficiently fit data for the sudden rise in temperature, as shown in Figure: 3.9. On the other hand, the combined model provides a good fit, as it includes both the radiative and conductive components, along with heat loss. It includes correction of sample data, adjustable and justified fitting, and improves the output of the measurements.

3.2.4. Instruments requirements and issues (Linseis LFA 1000)

3.2.4.1. Requirement of specimen and sample holder

This thesis used a Linseis laser flash analysis system (LFA 1000) for thermal diffusivity measurements of the specimens. The LFA-1000 measurement temperature range is from 298 K to 1000 K. Fabricated samples need to be cut in a specific round shape or according to the sample holder shape to conduct the measurements. Additionally, sample thickness also plays a vital role in obtaining accurate measurements, as samples that are too thick or too thin may give a $t_{1/2}$ that lies outside of the measurable range (0.01–30 s). The fabricated samples should follow the recommended thicknesses shown in Table 3.1 below to get measurable thermal diffusivity information

In some cases, an anti-reflective coating is also advantageous. For example, shiny metal samples (copper) need a diffuse homogeneous reflection, and graphite coating is recommended. In addition, samples like glasses; and polymers are also recommended for graphite coating.

Table 3.1: Standard sample thickness for laser flash analysis

Thermal Diffusivity	Suggested Sample Thickness
Low Diffusivity ex: Plastic (0.01 – 1 mm^2/s)	0.05 to 3 mm
Medium diffusivity ex: ceramics (1-50 mm^2/s)	0.5 to 5 mm
High Diffusivity ex: metals (50-1200 mm^2/s)	1 to 5mm

There are usually several sample holders and thermocouples (Table 3.2) to conduct thermal diffusivity measurements. These few limitations should be considered before running the measurements as described in Section 3.2.4.2.

Table 3.2: Types of Thermocouple

Thermocouple Type	K-Type	S-Type	C-Type
Temperature Range	-125 to 500 (°C)	25 to 1100 (°C)	25 to 1600 (°C)
Sample holder	SiC, Alumina, Stainless steel	SiC, Alumina	Graphite
Atmospheric Condition	Oxidizing, Inert, Vacuum	Oxidizing, Inert, Vacuum	Inert, Vacuum

3.2.4.2. Precautions before initiating a measurement

Besides preparing samples, a few vital factors should be considered carefully before conducting any measurements.

- The liquid nitrogen level should always be sufficient such that the detector is below 0°C
- The sample should be coated with graphite to get accurate results.
- The laser shouldn't directly hit the detector, which can permanently damage the detector.
- The chamber shouldn't be over-pressurized while changing the sample.
- The filter and the deionized water in the laser must be changed together at least once a year or after 1000 hours of operation.

3.2.5. X-ray powder diffraction (XRD)

3.2.5.1. Experimental details

X-ray diffraction (XRD) patterns of the fabricated materials were measured with an Empyrean diffractometer (Malvern Analytical) using monochromatic Cu Kα radiation (λ=1.54178 Å). The scanning angle (2θ) ranged between 10-90 degrees (^{o}) at 40 kV and 40 mA with a scan speed of 0.0954^{o} per second and a step size of 0.0286^{o}. The Match 3, PDF-4 + 2020 RDB software was used to analyse the measured data.

The main reason to produce diffraction patterns is to identify the unique crystallite structure of materials. For example, the crystal's atomic structure produces a specific pattern for cristobalite. On the other hand, atoms are differently arranged for quartz and will therefore give a different XRD pattern (Figure: 3.10).

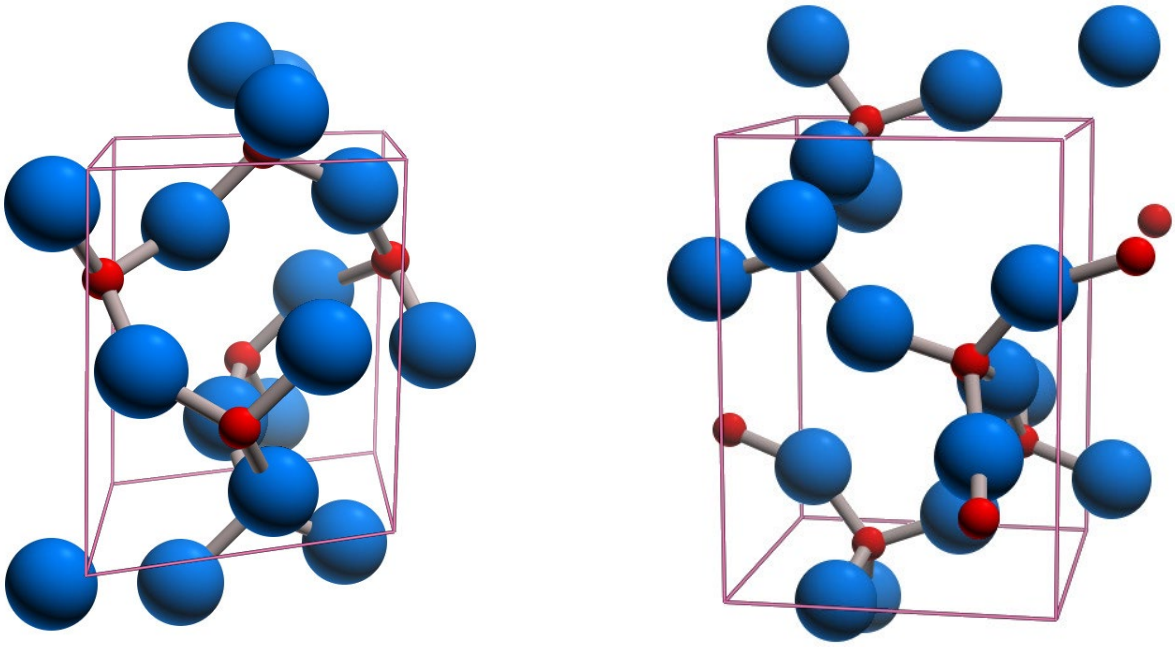

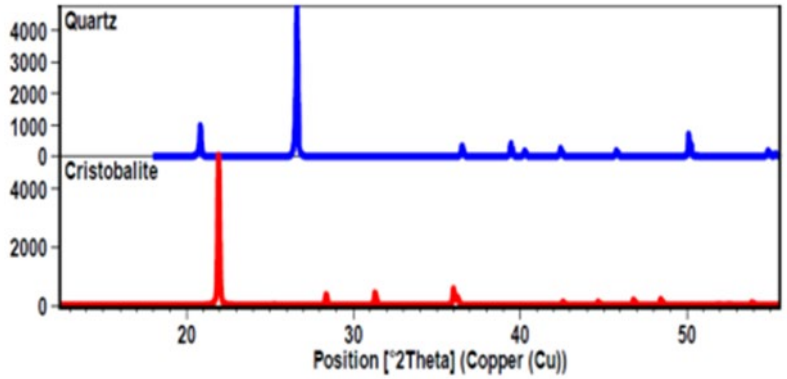

Figure 3.10: Structure of Quartz and Cristobalite. The XRD pattern represents SiO_2

3.2.5.2. Application of XRD analysis

XRD analysis is crucial for several applications, and it can identify useful structural properties of fabricated and raw materials such as:

- The crystalline phases present in a sample
- Unit cell lattice parameters via Bragg's Law (see next section)

- Bravais lattice type
- Residual strain
- Atomic positions within the crystal structure
- Texture
- Crystallite size and Macrostrain
- Dimension of the grains or crystallite of the materials.
- Atomic arrangements can be defined by analysing symmetry elements of a crystallite structure from the XRD pattern.
- Many different crystal lattice systems, as shown in 3.11, can be studied and identified by analysing symmetry elements.

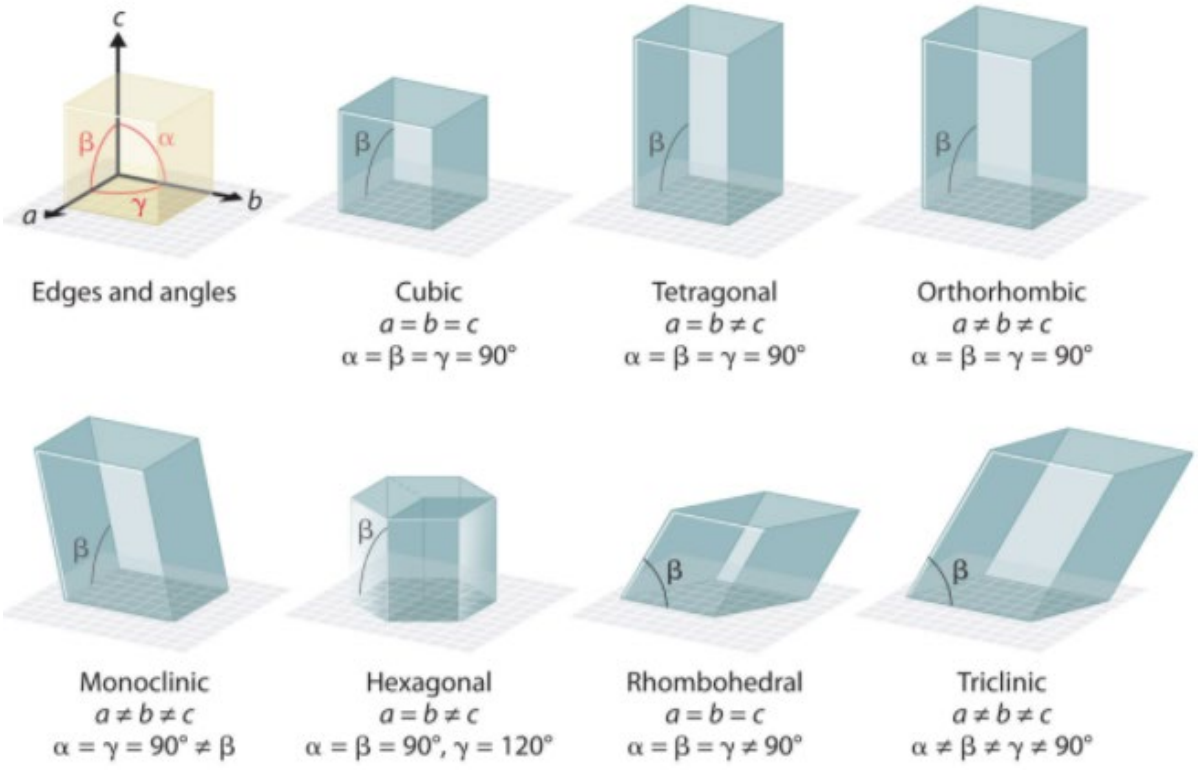

Figure 3.11: The general features of the seven basic unit cells. The lengths of the edges of the unit cells are indicated by a, b, and c, and the angles are defined as follows: α, the angle between b and

c; β, the angle between a and c; and γ, the angle between a and b (Source:https://chem.libretexts.org/)

3.2.5.1. Braggs Law in X-ray diffraction

Different planes of atoms can be identified by using Miller indices (hkl), which helps investigate the atomic structure and microstructure of a sample. Following Bragg's law, XRD produces diffraction peaks from scattered X-rays according to the equation below, which can be used to calculate the distance between parallel planes.

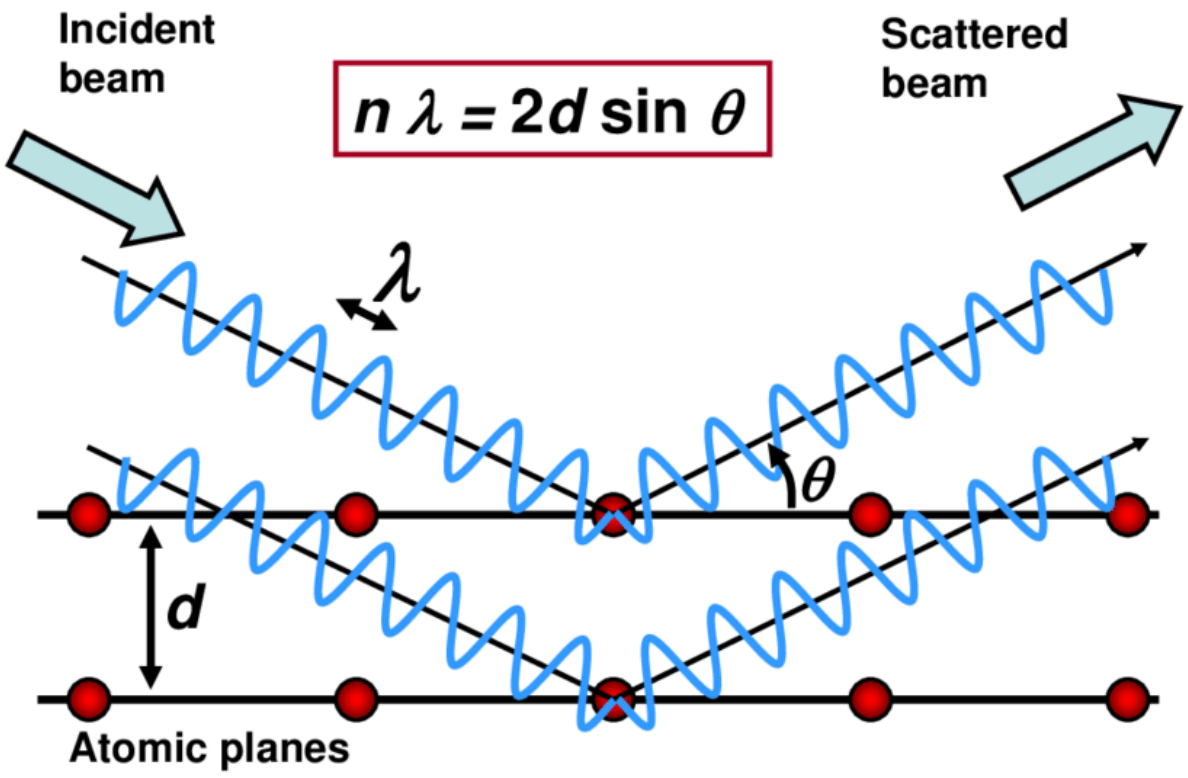

Figure 3.12: Bragg's Law

Here,

λ = wavelength of diffractometer, which has a fixed value of 1.54°Å in this work

D = distance between two parallel atomic planes / interplane spacing spacing

θ = angle between the wave vector of two incident planes.

2θ = diffraction angle, calculated between the incident beam and the detector.

To obtain an X-ray diffraction pattern, a sample can be in different forms, including powder, sintered pellets, coating on a substrate, etc. An ideal powder sample can contain billions of randomly orientated crystallites for a polycrystalline sample, such that the diffraction pattern is an average overall possible orientation. This requires sufficient sample mass to obtain good statistics.

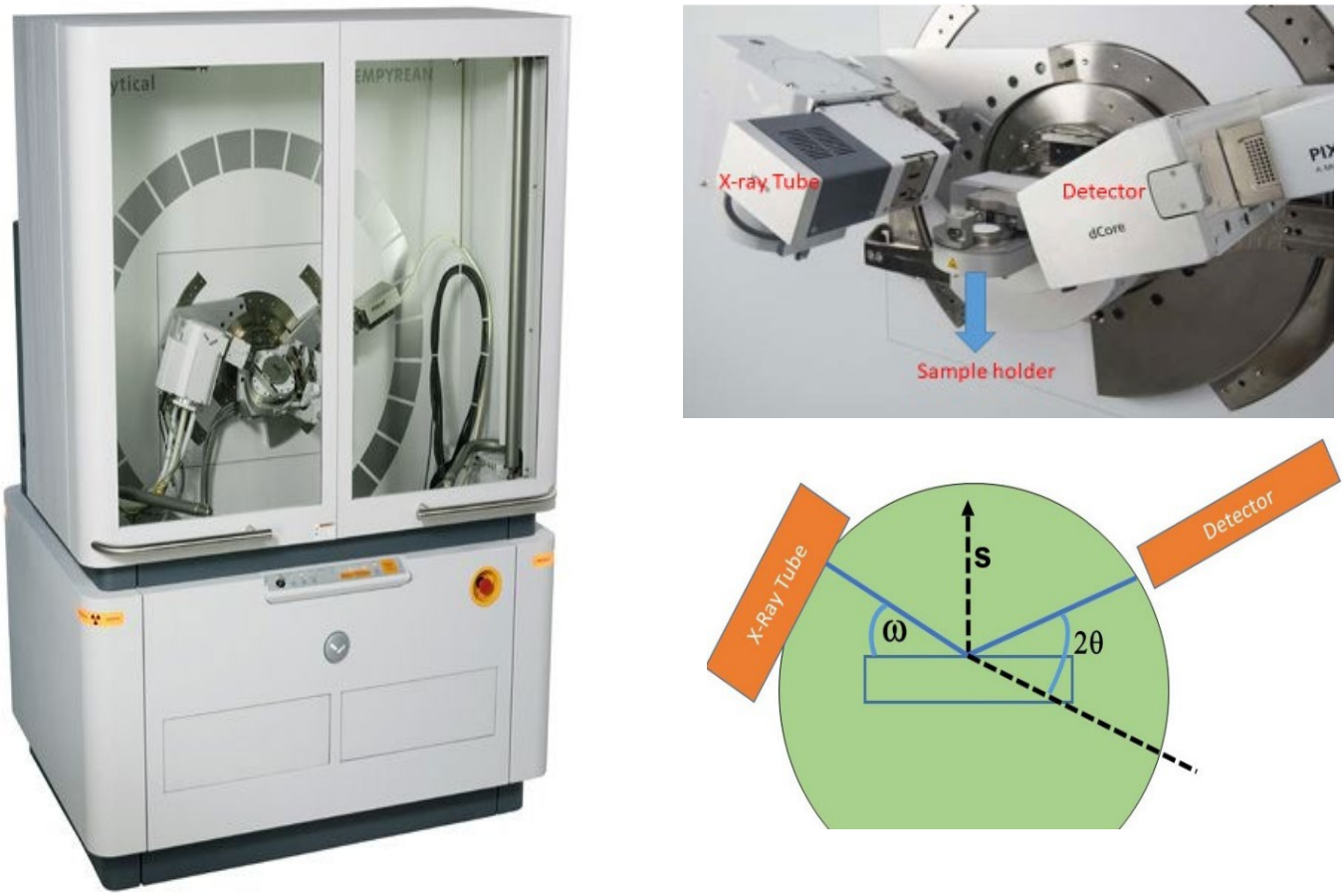

Figure 3.13: PANalytical Empyrean XRD.

3.2.6. Scanning electronic microscopy (SEM) and EDS

3.2.6.1. Experimental details

In this thesis, scanning electron microscopy (SEM) on the JEOL JSM-6490LV microscope (Figure 3.15) was used to reveal the specimen's morphology at room temperature under a vacuum condition. Carbon tape was used to place the sample on the sample holder. Then, the offset is measured using a small ruler to set up the specimen height properly to avoid an unwanted accident with the electron beam. Then, using 15kV voltage and a beam current of 60 mA, it is used to scan for specimen surface morphology.

Additionally, the sample's composition is measured using energy-dispersive X-ray spectroscopy (EDS), which provides a map of elements of the specimen (Figure: 3.14), including contaminants. Users can easily gather chemical characterization and elemental distribution on small (nano-scale) specimen areas using EDS imaging tools. Producing an X-ray from the electron beam helps characterize the elements present in a sample. Several factors can affect EDS spectrum accuracies, such as overlapping peaks and sample topology (surface smoothness). The number of X-rays, energy level, and sample density can be significant factors for the accuracy of EDS analysis. No coating is required for conductive samples; otherwise, for insulating, the sample must be coated with a conducting film to get an undistorted signal from the electron beam by avoiding unwanted charging of the surface.

3.2.6.2. Principles of scanning electron microscopy

A high-energy-focused electron beam is used in the scanning electron microscope to produce various signals from the surface of a solid specimen. Information such as external morphology (texture), chemical composition, sample crystallinity, and the orientation of raw materials to make up a sample can be revealed from the generated signal of a high energy focus electron beam. The incident beam is scattered from a selected specimen area and produces secondary electrons and X-rays. These are collected to create two-dimensional images to reveal the variation of the sample properties.

A significant amount of kinetic energy is carried by SEM's accelerated electron. The carried kinetic energy can be transferred when the high electron beam interacts with the solid specimen surface. Various types of signals are produced from kinetic energy. These signals are the main reason for making secondary electrons with SEM images and backscatter electrons (BSE). The secondary electron produces sample images, and the backscatter electron illustrates the contrast of the composition of any multiphase samples (i.e. for rapid phase discrimination). The energy of the generated X-rays produced as a byproduct of the electron interactions also provides information on the element present in the sample. This signal is collected to perform EDS mapping.

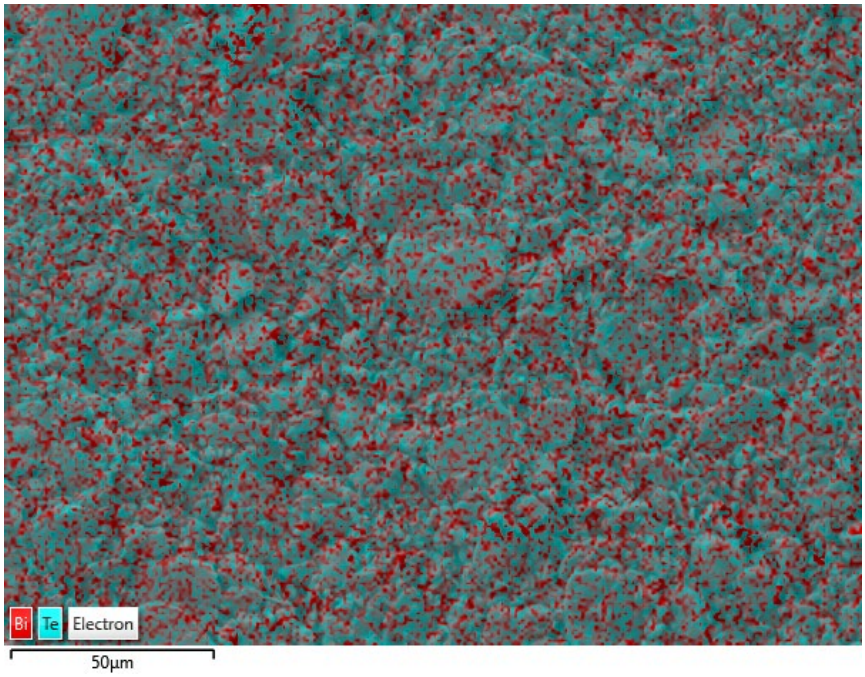

Figure 3.14: Elemental analysis using EDS technology.

Figure 3.15: Scanning electron microscope (JEOL JSM-6490LV).

3.2.7. Differential scanning calorimetry (DSC)

3.2.7.1. Experimental process

In this work, the fabricated samples' heat capacity (C_P) was determined using the differential scanning calorimetry (DSC) analytical technique. Initially, data was collected from a blank crucible and reference samples (a single crystal of Al_2O_3) by a DSC-204F1 Phoenix calorimeter under an argon gas flow, with a 50 ml/min rate. Then under the same conditions, the fabricated samples were characterised, and the specific heat capacity was calculated via comparison with the reference sample data.

3.2.7.2. Background

Differential scanning calorimetry (DSC) is a thermal analytical technique conducted to determine the sample's heat capacity. In this analytical technique, the reference and analytical samples consume different amounts of heat to increase their temperature. The reference and experimental samples experience nearly identical temperature steps during the measurements. In the DSC

measurement system, the program is designed so that the sample holder temperature will rise linearly as a function of time. The program uses a reference sample in which heat capacity is predefined at the different temperature steps.

There are a few main applications that are conducted through DSC analysis. These are given below:

1. Phase Transition
    - Melting Point
    - Glass Transition
    - Crystallization Time
    - Crystallization Temperature
2. Melting Point
3. Crystallisation point
4. Percent of Crystallization
5. Compositional analysis
6. Thermal stability
7. Heat Capacity

According to the operational mechanism, there are two types of DSC: heat flux DSC and power compensated DSC. For the heat flux DSC, the empty reference pan is placed on a thermoelectric disk, and, on the other side, the sample material is enclosed in a pan. A furnace surrounds both pans. The furnace transfers heat to the sample and the reference pan through the thermoelectric disk at a linear rate. The thermocouple measures the temperature difference between the reference pan and the sample, and the heat flow is determined by a thermal equivalent of Ohm's law:

$$q = \Delta T / R \qquad 3.5$$

Here, q = Heat flow

ΔT = Temperature difference between a sample and the reference

R = Resistance of the thermocouple.

On the other hand, in power compensated DSC, the reference and the sample are placed in two different furnaces and heated by two different heaters. The reference and the analytical sample require different thermal power to maintain the same temperature level in both specimens. Additionally, the temperature differences are measured and plotted as a function of temperature. A thin flake with a flat bottom is required to conduct the measurements to get high heat transport inside the crucible. Aluminium crucibles are chosen according to their temperature profile.

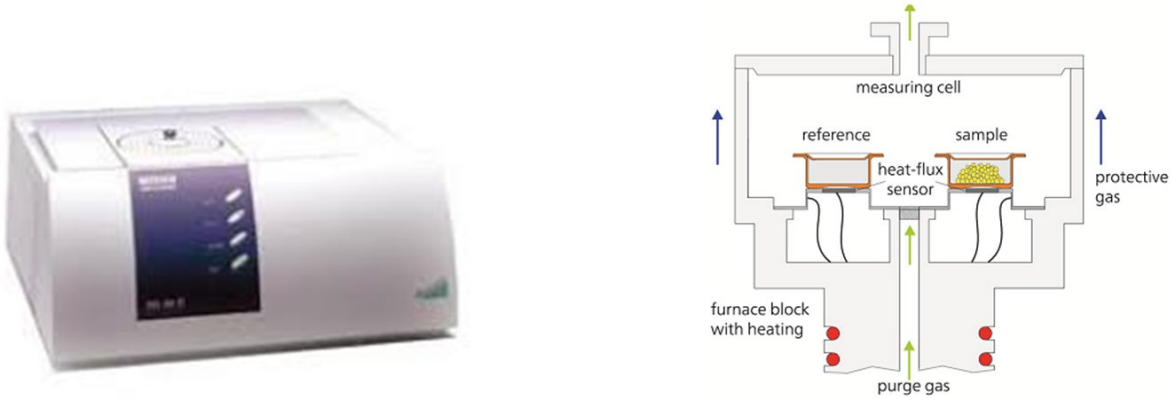

Figure 3.16: (a) Differential scanning calorimetry (DSC) device (Model: Netzsch 204F1), and (b) the operational principle of the DSC technique.

Chapter 4: Significant reduction of thermal conductivity in the Cu_2Se thermoelectric doped using a chemical reaction with Na_2CO_3

4.1.Introduction

Heat management plays a crucial part to improve thermoelectric performance for harnessing electric power from heat. Thermoelectric generators are gaining continuous interest in energy extraction technology to produce renewable green energy, especially with their ability to produce energy from low-grade heat sources. For proof of this, a thermoelectric energy extraction device is able to extract power from the exhaust system [98, 99]. Even through body heat management, TE devices can convert human body heat into energy via close contact between the skin and a wearable device [100]. Among several vital factors related to thermoelectric system efficiency, thermal conductivity is considered one of the major factors influencing the devices' working efficiency (zT) at high temperatures. The efficiency of thermoelectric materials is normally calculated from the figure-of-merit (zT) equation which is given as:

$$zT = \frac{\sigma S^2 T}{\kappa} \qquad 4.1$$

Where,

$\sigma(T)$ = is the electrical conductivity,

$S(T)$ = is the Seebeck coefficient,

T = is the absolute temperature and

$\kappa(T) =$ is the thermal conductivity.

The equation shows that, with reducing thermal conductivity, the value of the figure-of-merit increases, giving maximum thermoelectric efficiency. The typical strategy for reducing heat transport in a solid system is to maximise phonons scattering and minimise phonon mobility. For instance, studies on Cu_2Se (a *p*-type thermoelectric compound recognised since the mid-1970s) [65] identified that it has low phonon mobility. Later studies suggested this was due to the liquid-like state of Cu atoms above the β- phase transition, where the superionic nature may suppress vibrational modes [63]. A separate study proved that, in contrast, it was primarily the anharmonic phonon interactions that produce the low κ, which maximizes zT value up to 1.5 at 1000 K [64]. To further improve the performance, several groups have looked at two other strategies in Cu_2Se: nano-doping to form composites or substitutional chemical doping.

Inclusion of graphene, graphene oxide, carbon nanotubes, copper oxide, carbon dots or other insoluble nanostructures into Cu_2Se structure to form nanocomposites has also been shown to significantly reduce thermal conductivity through additional scattering or attenuating of the phonons [67, 101-104].

The addition of a substitutional element in this thermoelectric compound to replace either Cu or Se in the lattice has also become a common trend in recent years to reduce thermal conductivity. The following "dopants" have been investigated in $Cu_{2-x}Se$: Ag, [65, 66] Sn, [67] In, [68, 69] I, [70] B, [71] Fe, [69] Ni, [69] Mn, [69] Zn, [69] Sm, [69] Li, [72] S, [73] Te[74] and Na [75-77]. The primary effect of these dopants is to act as point defects that scatter phonons whilst also enhancing the number of electronic carriers in some cases. To a lesser degree, dopant engineering is also associated with microstructure defects on grain boundaries and dislocations responsible for further reducing heat conduction. Based on past results, it seems alloying with Na is a prospective

candidate to get the desired thermal conductivity from Cu_2Se, and as a relatively cheap and earth-abundant material, it has the advantage in this regard.

Alloying Na for hydrothermally prepared $Cu_{2-x}Se$ for improving properties has been reported in several journals [75-77]. However, all the three references presented Na inclusion in $Cu_{2-x}Se$ prepared by the *hydrothermal route* and followed by solid-state heat treatment. Here, an alternative synthesis method using melt-solidification with a Na_2CO_3 precursor was explored, which can produce large mass yields.

4.2.Experimental section

Synthesis: Using a mortar and pestle, 0.09, 0.18, 0.35, 0.70, and 1.40 wt. % anhydrous Na_2CO_3 (Sigma-Aldrich, >99.5% purity) powder was mixed with Cu_2Se. Then, the sample was heated up by a vertical mosilli furnace to ~1473 K in Ar-5 vol. % H_2 flow at a heating rate of 10 K/min, with a 20-minute dwell at 1473 K. After that, the furnace was left for a while to return to room temperature. Then the final dense polycrystalline products were shaped into round disks using a Struers Accutom-50 cutting machine for getting the sample form suitable for thermal analysis.

Crystal Structure: The phase and crystallite structure were studied by room temperature X-ray diffraction (XRD) patterns analysis using a Bruker D8 discover XRD system using Cu Kα radiation. X-ray diffraction patterns were collected in the range of 10–60° with a step size of 0.02°/s. using a fitting method determined the lattice parameters for pure Cu_2Se and the Na_2CO_3/Cu_2Se products.

Temperature-dependent X-ray diffraction measurements: High-resolution synchrotron powder diffraction data were collected on the powder diffraction beamline at the Australian synchrotron using λ = 0.58973 Å, where the detectors angle was 2.5°-80°, rotation speed at ~2

Hz/min. The heating rate was 4 deg. /min under helium gas flow at a 300−774 K temperature range.

Data processing: The XRD peaks positions were extracted using the FITYK0.9 [105] software, and scripts were also generated from these calculations to assemble the consecutive synchrotron scans into iso-intensity maps. For the low temperature α phase, the peaks examined were the characteristic 004 (d=6.82 Å), and 139 (d=2.27 Å). The areas were normalized to a value of 1.0 at 303 K for comparison purposes.

Field emission scanning electron microscopy (FE-SEM): Sample morphology was studied by using field emission scanning electron microscopy (Zeiss EVO SEM).

TG and DTA: To investigate the decomposition of pure Cu_2Se, and Na_2CO_3 doped Cu_2Se, TG–DTA techniques were used when the temperature ramp rate was 10 K per minute.

Thermal conductivity: A Linseis LFA 1000 system as used to determine the thermal diffusivity (D) measurements under vacuum conditioning. A Netzsch DSC-204F1-Phoenix calorimeter was used to determine the specific heat (C_p) capacity under an argon atmosphere with 50 ml/min flow rate. Finally, manually, sample density was calculated by measuring weight and dimensions. Then thermal conductivity was calculated using Equation 3.2.

4.3.Results

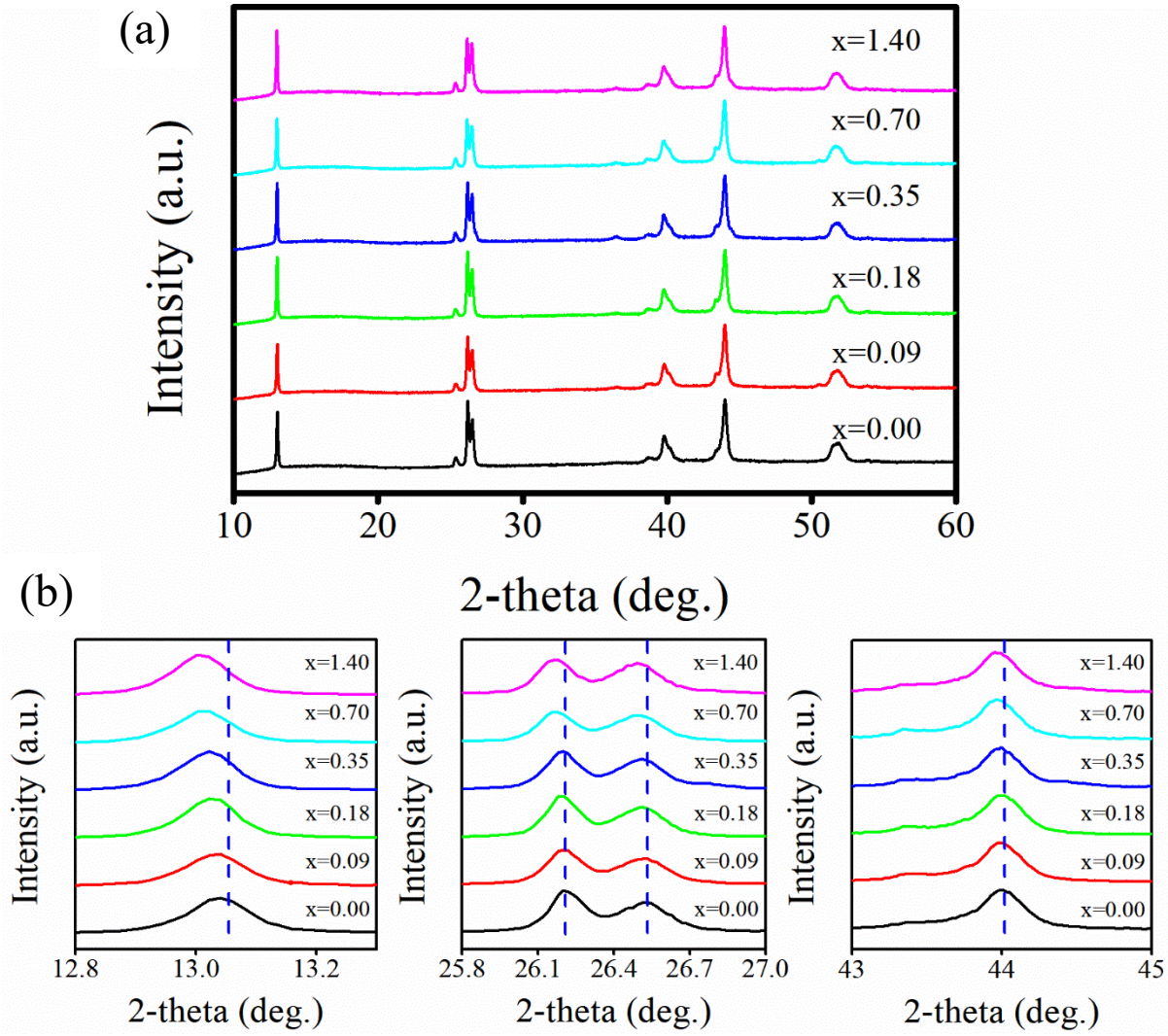

Figure 4.1 (a) Room-temperature powder x-ray diffraction patterns of $Cu_2Se{-}x$ wt. % Na_2CO_3 samples (x = 0, 0.09, 0.18, 0.35, 0.70, and 1.40). (b) The bottom sides are the enlarged view of a selected region.

X-ray diffraction patterns for pure Cu_2Se and doped samples were collected at room temperature (Figure 4.1a). The patterns match with the low-temperature monoclinic form of Cu_2Se (PDF 04-018-3523, C2/c (#15), designated α-Cu_2Se)[106]. The fits and data from Figure 4b show that peak positions are all shifted to smaller 2-theta values, indicating that lattice parameters are increasing. The peak shift implies that the reaction of Na_2CO_3 into Cu_2Se has a notable effect on the crystal lattice parameters of α-Cu_2Se attributed to the substitution of Na and O ions.

For exploring further details of adding Na_2CO_3 in Cu_2Se, variable-temperature synchrotron XRD measurements were performed. Figures (4.2a, 4.2b) illustrate the pure Cu_2Se and 1.40% Na_2CO_3-Cu_2Se iso-intensity image in the range of room temperature to 774 K . The α-phase peaks at a 5° and $\sim 15^{\circ}$ gradually started to become weaker as the temperature increased, showing that the sample has begun the transformation to the cubic phase (Fm-3m (#225), designated β-Cu_2Se. The transition temperature in (Na, O) doped samples is shifted in temperature compared to the pure sample.

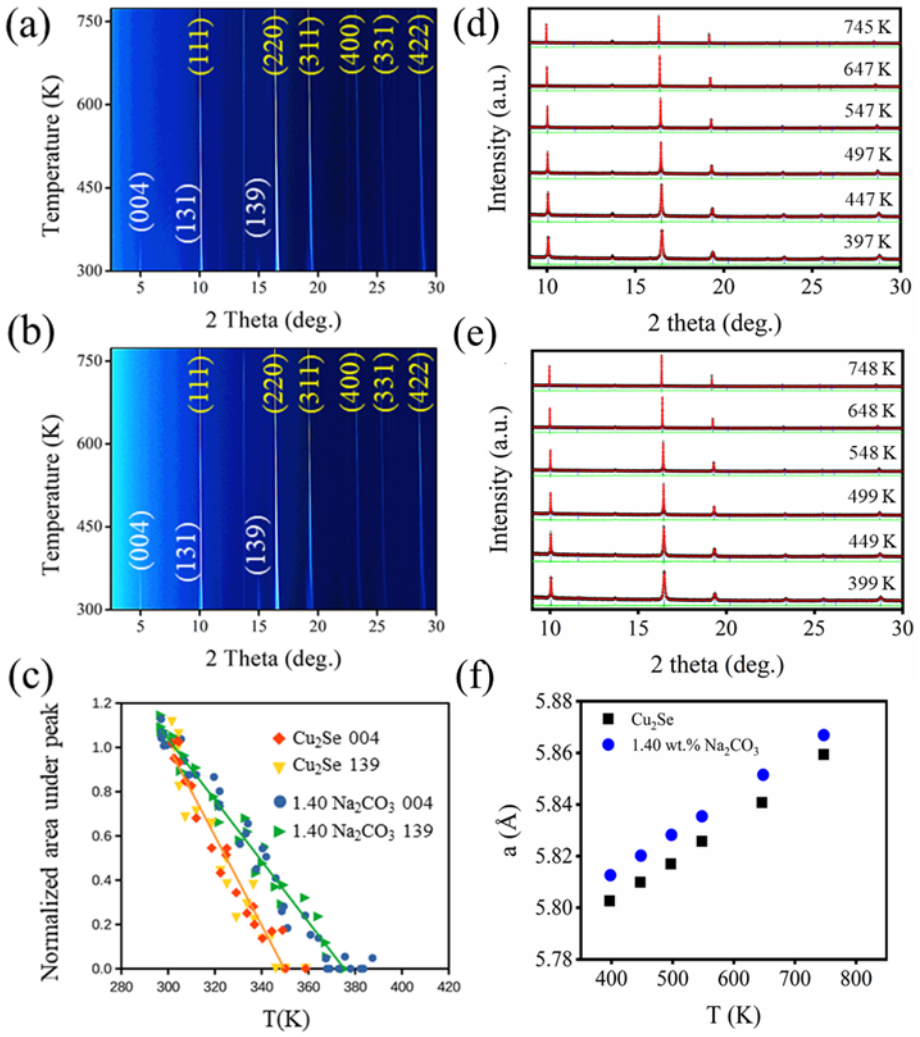

Figure 4.2: Iso-intensity images of a series of variable-temperature X-ray diffraction patterns of the (a) pure Cu_2Se and (b) 1.40 wt.% Na_2CO_3 sample. The wavelength is 0.58973 Å; c) Normalized area under selected peaks of the Cu_2Se alpha phase of the pure and 1.40 wt.% Na_2CO_3 Cu_2Se with temperature. (d,e) fitting of synchrotron powder diffraction patterns of Cu_2Se and 1.40 wt. % Na_2CO_3 incorporated Cu_2Se (+ data points,–calculation line, | marker points,–difference line); (f) Lattice parameters for high-temperature forms of pure Cu_2Se and 1.40 wt.% Na_2CO_3.

Table 4.1: Parameters for the refinement of pure Cu_2Se and Na_2CO_3 incorporated Cu_2Se samples at 398 K, 448 K, 498 K, 548 K, 648 K, and 747 K. R_p and R_{wp} are the profile and weighted profile R-factors, respectively, χ^2 is the goodness-of-fit, and Derived Bragg R-Factor.

Temp (K)	Lattice parameter / Sample	a (Å)	R_p	R_{wp}	χ^2	Derived bragg r-factor
398	1.40 wt% Na_2CO_3	5.8126 ±0.0004	8.58	11.2	1.20	0.96
448		5.8202 ±0.0003	8.68	11.24	1.21	0.75
498		5.8282 ±0.0002	8.95	11.69	1.31	0.54
548		5.8354 ±0.0002	8.52	11.75	1.95	3.44
648		5.8515 ±0.0001	9.9	12.9	1.56	5.34
747		5.8669 ±0.0001	8.88	12	1.98	7.07
397	Cu_2Se	5.8026 ±0.0003	7.58	10.46	1.69	0.71
447		5.8099 ±0.0003	7.78	10.49	1.663	0.83
497		5.8170 ±0.0002	7.91	10.76	1.713	0.89
548		5.8258 ±0.0001	7.51	10.34	2.05	2.61
646		5.8408 ±0.0001	9.42	12.61	2.32	2.63
747		5.8594 ±0.0001	9.76	13.34	2.538	3.35

To measure the thermal conductivity, laser flash data analysis was performed while comparing several fitting methods to find out the best models to avoid experimental errors during measurements. From Figures 4.3 and 4.4, the combined model showed an excellent fit to the data, whereas the adiabatic and finite pulse method showed less data fitting than the combined model. The calculation of thermal diffusivity (Figures 4.3 and 4.4) indicated that the finite pulse method provided 25% less fitting accuracy, whereas the adiabatic model provided 22.5% less fitting than the combined model. The combined model was implemented by Linseis uniquely for its LFA system. This model is more reliable than any other model, and it gives a more correct fit than the adiabatic, finite pulse, and heat loss models. The significance of the combined model is that no operator choice between the different models is necessary, as it includes all of the major correction terms. Figures 4.3 and 4.4 are the data from 1.4% Na_2CO_3- Cu_2Se at 554 K temperature, and all the data analysis has been done using baseline: baseline slope fitting with 25 filter points to obtain accurate fitting of the thermal diffusivity.

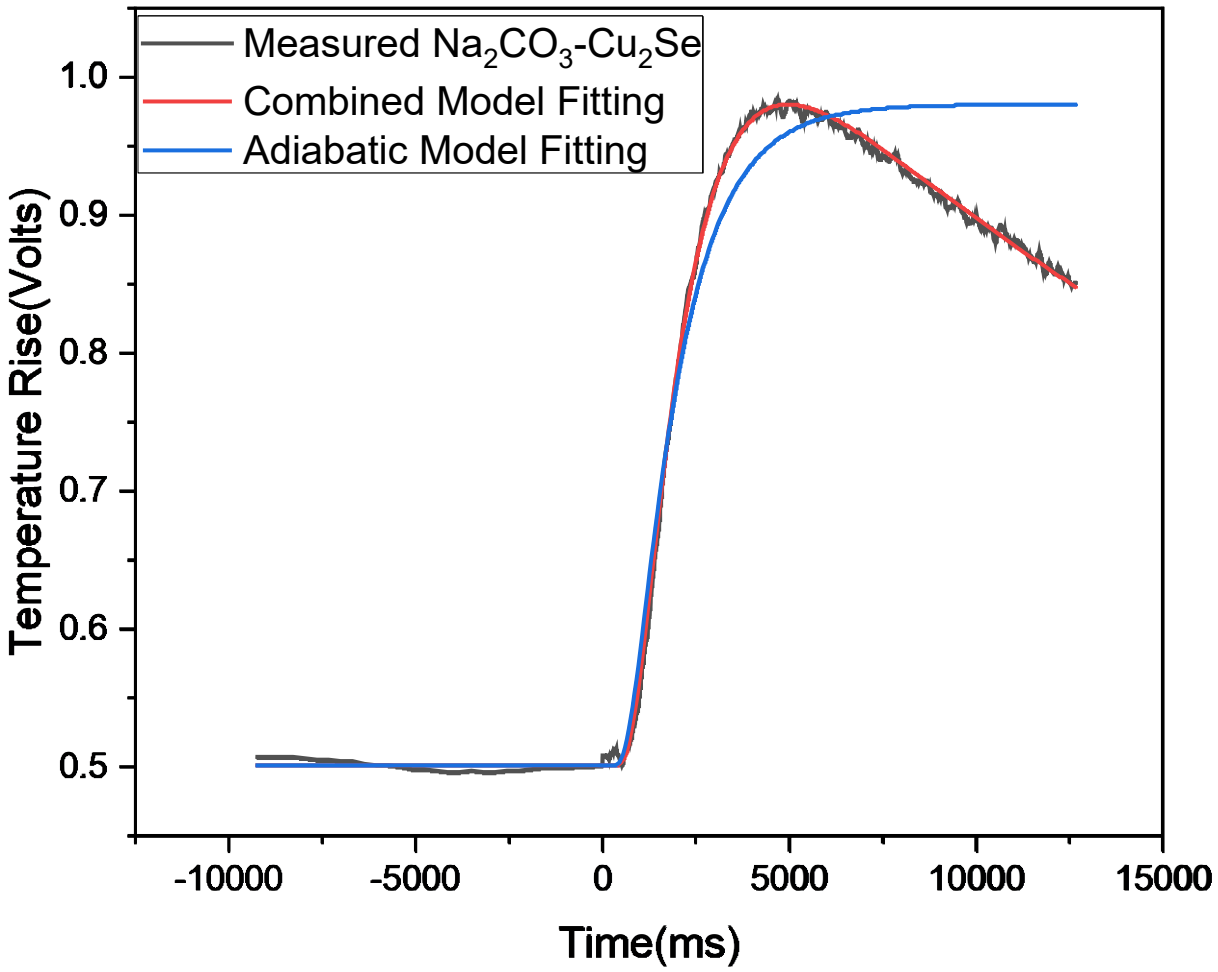

Figure 4.3: The thermal diffusivity data for 1.4% Na_2CO_3-Cu_2Se, along with a comparison of the fitting method between the adiabatic model and the combined model.

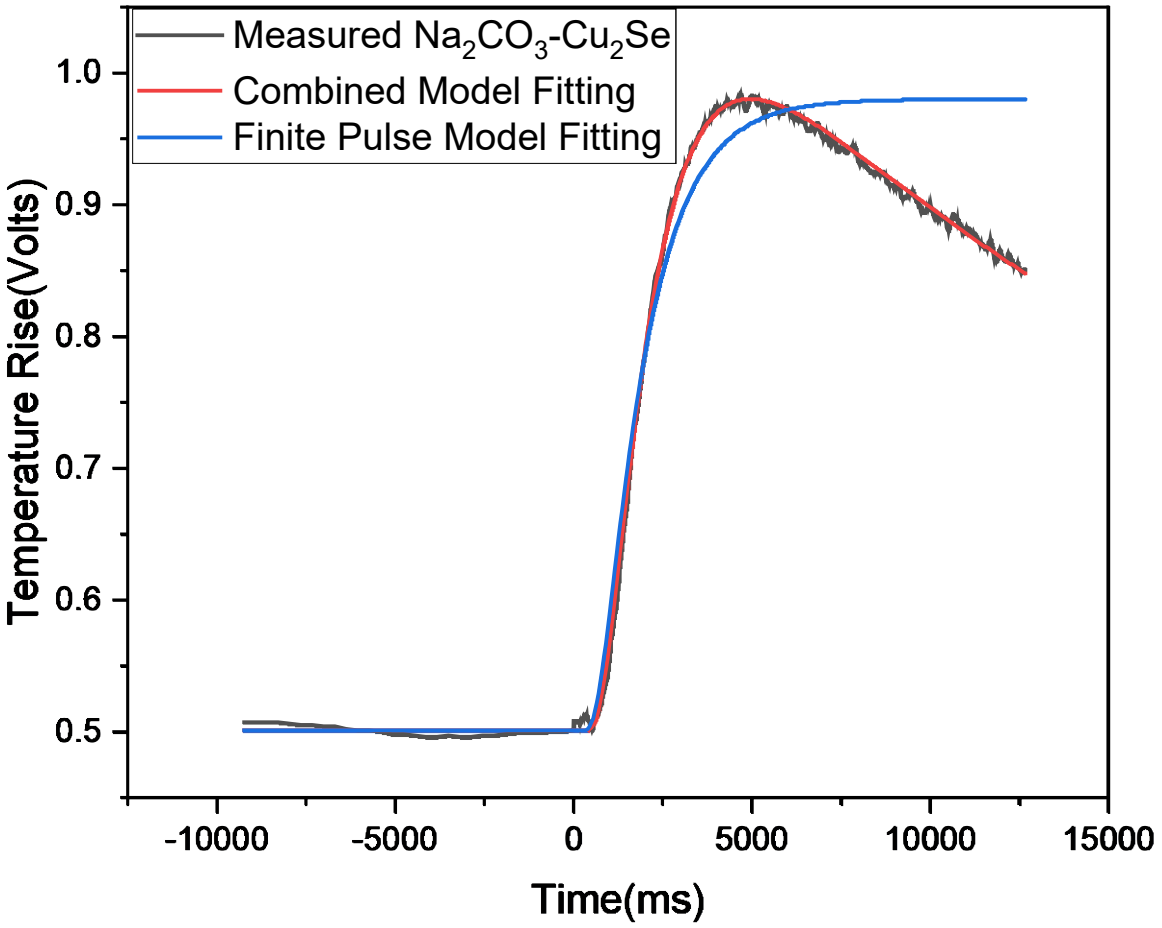

Figure 4.4: 1.4% Na_2CO_3-Cu_2Se thermal diffusivity LFA data fitting analysis comparison between the finite pulse model and the combined model.

Using Equation 3.2 to convert the thermal diffusivity into κ, the thermal conductivity (κ) of pure and samples reacted with Na_2CO_3 is presented in Figure: 4.5. Thermal conductivity followed a linear trend with the increasing amount of Na_2CO_3 in Cu_2Se, thermal conductivity decreased. The sample had the highest amount of Na_2CO_3 (1.4wt %), showing ~34% lower thermal conductivity than pure Cu_2Se at 554 K.

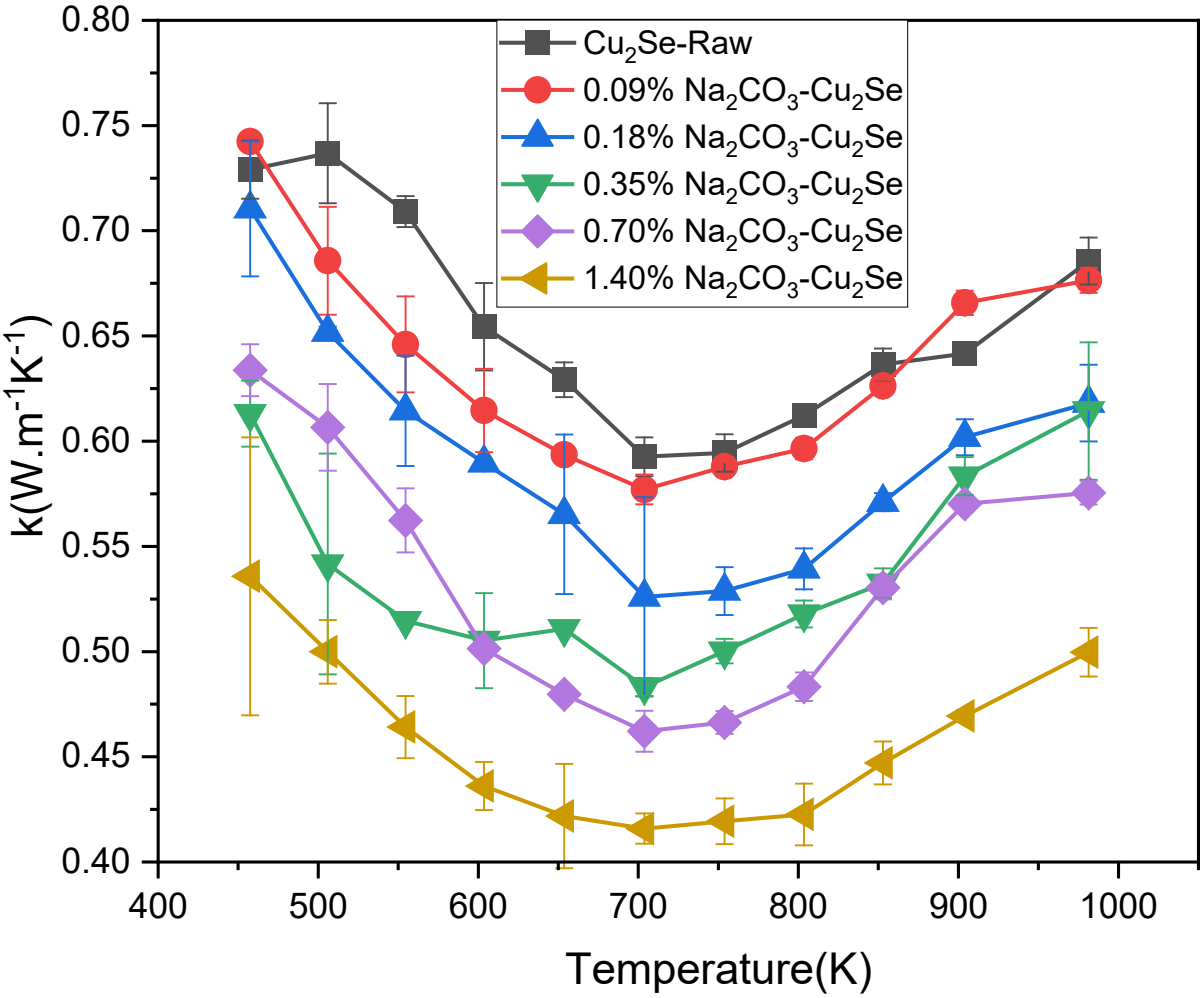

Figure 4.5: Thermal conductivity (κ) (including error bar) of pure Cu_2Se and Cu_2Se reacted with additional Na_2CO_3.

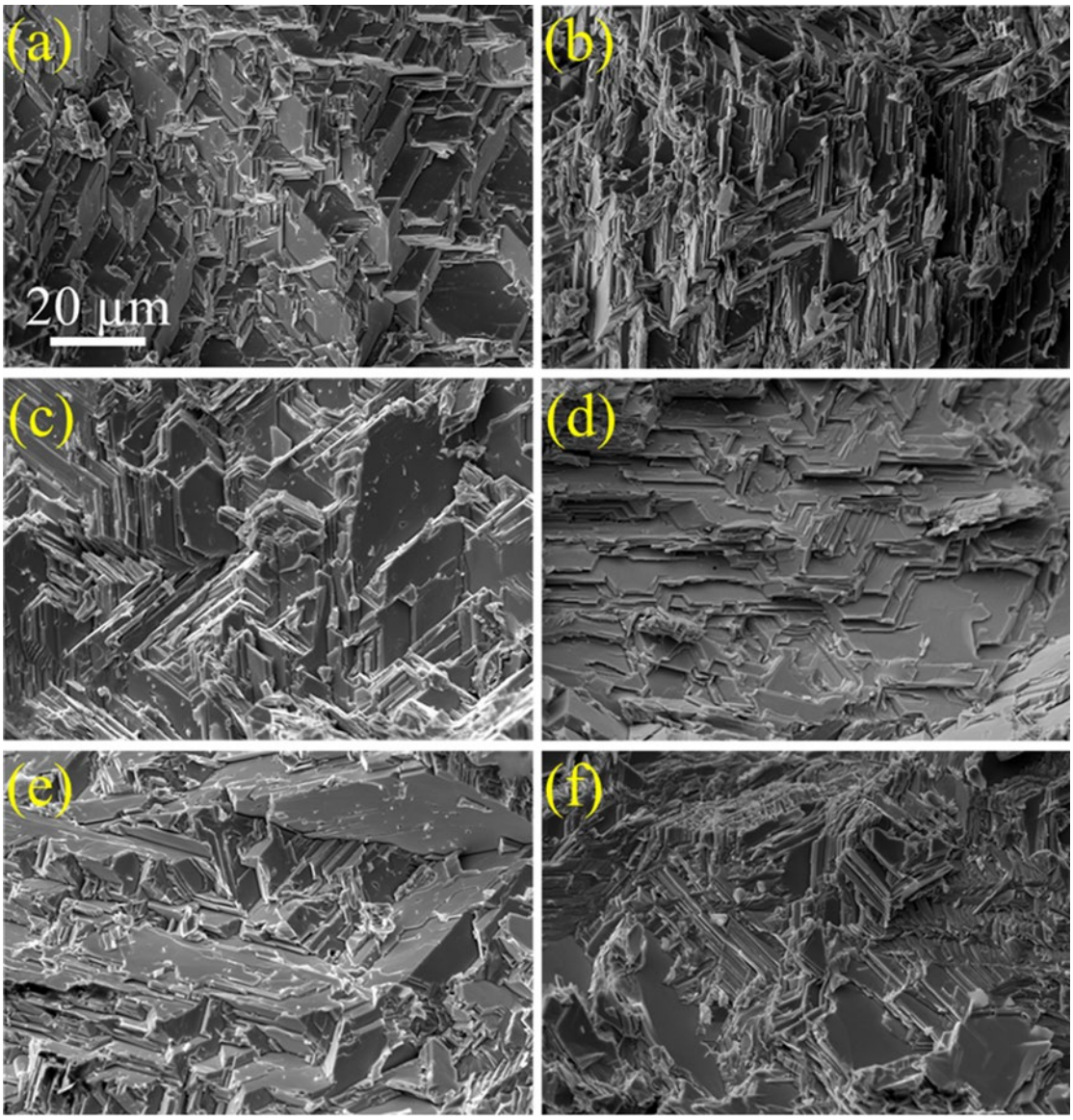

Figure 4.6: SEM image of fresh fractured cross sections of (a) pure Cu_2Se; (b) 0.09 wt.% Na_2CO_3; (c) 0.18 wt.% Na_2CO_3; (d) 0.35 wt.% Na_2CO_3; (e) 0.70 wt.% Na_2CO_3 and (f) 1.40 wt.% Na_2CO_3 samples.

The phase morphology of all samples has been observed by field emission scanning electron microscope (FE-SEM) (Figure 4.6). We found that the samples appear to be fully dense without any observable porosity. Phonon transport in Cu_2Se is explained in Figure 4.7 [107-109]. The Na and O act as point mass defects which will induce scattering as described in Section 2.5.1.

Additionally, secondary defects may also be present; for example, vacancies and modified grain boundaries could each induce extended strain fields and result in phonon scattering.

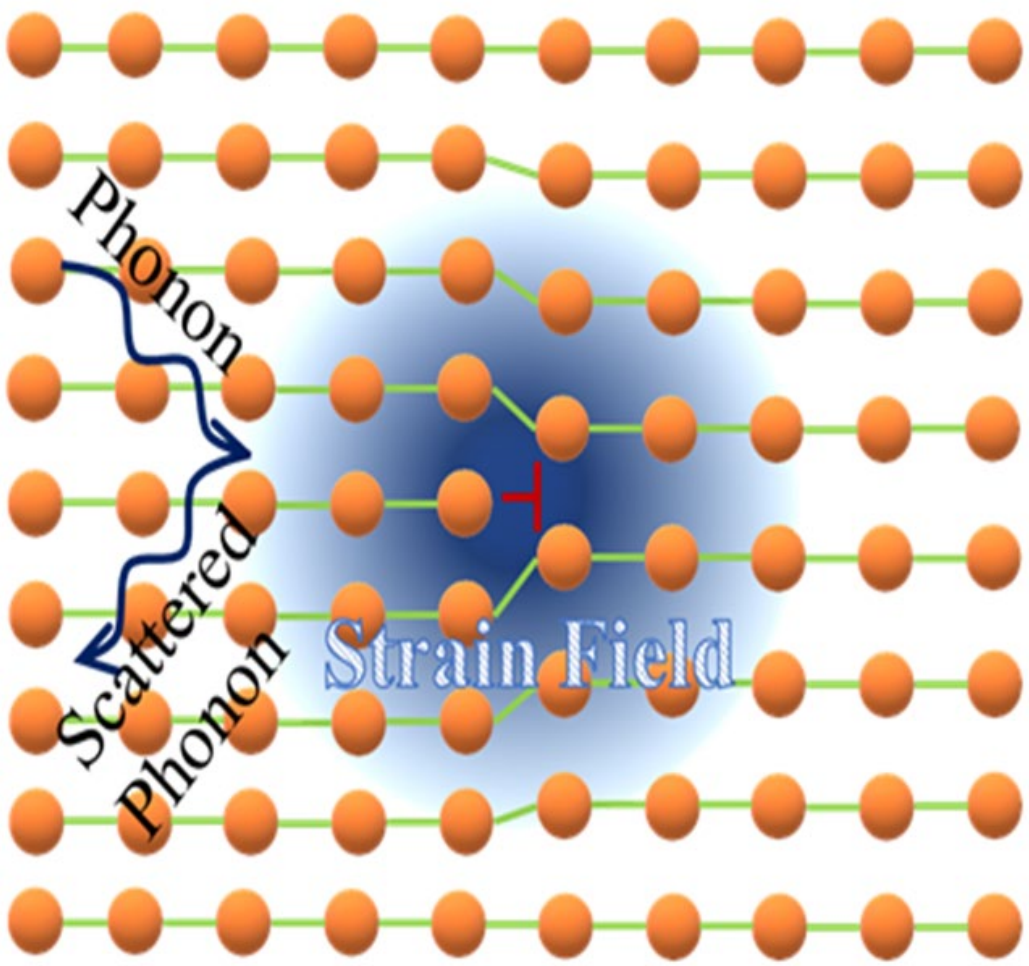

Figure 4.7: A schematic diagram of the mechanism of phonon transport [107]

4.4.Discussion

When Na_2CO_3 reached its melting point of 1123 K (850 °C), it started decomposing [110]. The decomposition chemical reaction is given below

$$Na_2CO_3 \rightarrow Na_2O\ (s) + CO_2(g) \qquad 4.2$$

$$Na_2O \rightarrow 2Na\ (g) + \frac{1}{2}O_2(g). \qquad 4.3$$

In the above reaction, the decomposition of Na_2CO_3 is extremely slow [110, 111]. It is expected that Na_2CO_3 underwent 10% to 20% decomposition when it was treated at 1473 K [112, 113].

Equations 4.2 and 4.3 indicate that during the chemical reaction, CO_2 reduction has occurred, and oxygen has been produced as a byproduct. As a result, Na and oxygen are available to be doped into the Cu_2Se lattice. Sodium substitution into the lattice impacts the $\alpha \rightarrow \beta$ transition temperature (observed from experiments) due to lattice parameter increase occurring with the substitution of the larger ion. In past work on Na doping, some groups, such as Zhu et al. [76], were unable to find any changes in lattice parameters, whereas other groups, such as Jin et al. [77], detected a 5% increase after adding Na in some samples. In our work, we have shown that the lattice constant increased with the addition of Na_2CO_3 in the Cu_2Se structure, which is indicated by an increase of volume by 0.5% in the 1.40wt% reaction. The relatively small change in the unit cell size may indicate the synergistic effect of oxygen addition unique to the reaction outlined in Equations 4.2 and 4.3.

In this present work, due to a considerable size/mass mismatch of Cu and Na atoms and oxygen substitution with Se, there is the possibility of increased phonon scattering, which might be considered the main reason for reducing the thermal conductivity.

4.5.Conclusion

Cu_2Se is a well-known thermoelectric material with an intrinsically low thermal conductivity resulting in promising thermoelectric performance. The addition of Na_2CO_3 during the melt route process leads to a significant reduction of thermal conductivity with the increased % of Na_2CO_3. This is attributed to the mass defects (Na, O), which hamper phonon propagation affecting phonon scattering in the Cu_2Se structure. Due to increased phonon scattering, thermal conductivity decreased significantly in the final product. The inclusion of Na might slightly substitute Cu, causing a reduction of carrier concentration [81, 83], which leads to electron injection from Na. Another effect on thermal conductivity is changing mobility [75], which happens with Na addition.

In this work, I have only focused on the thermal properties (thermal conductivity) of Cu_2Se after Na and O addition to the lattice. Still, a separate collaborative work studied the overall thermoelectric performance (see Paper 1 in my list of Publications).

Chapter 5: Towards flexible thermoelectrics using Bi_2Te_3 in a nanocomposite with a polyurethane matrix.

5.1.Introduction

Global energy uncertainty and increasing renewable energy demand provide the impetus for improving the efficiency of energy conversion technologies [114]. Thermoelectric technology offers a promising way to convert heat into usable energy using a solid-state device without the need for mechanical components [114, 115]. However, the performance of thermoelectric materials needs to be improved. This is evaluated by the dimensionless figure-of-merit (zT), $zT = \sigma S^2 T/\kappa$, where σ is the electrical conductivity, κ is the thermal conductivity, T is the absolute temperature, and S is the Seebeck coefficient. The figure-of-merit (zT) equation clearly states that obtaining a highly efficient thermoelectric material requires high electrical conductivity, high Seebeck coefficient, and low thermal conductivity. It is challenging to produce a composite with high electrical conductivity and low thermal conductivity concurrently as they are directly proportional in most materials [116]. In this work, I have introduced a polymer (polyurethane) as a matrix for the well known thermoelectric Bi_2Te_3 to face the challenge by minimising the thermal conductivity of Bi_2Te_3 via the introduction of a nanostructured composite. Similar strategies have been used in past thermoelectric materials to either increase the electrical conductivity or decrease the thermal conductivity [26, 117]. One new aspect is this study used exfoliated Bi_2Te_3 produced via a liquid-phase exfoliation method and then added the nanosized Bi_2Te_3 into a 3D printable polyurethane (trade name 'ChronoFlex C®') matrix. The target was to produce lower thermal conductive nanocomposite forms of Bi_2Te_3 as a search for flexible future thermoelectrics.

5.1.1. Liquid phase exfoliation of Bi_2Te_3

Since graphene was discovered in 2004 by Andre Geim [118], two-dimensional (2D) materials, have become a hot topic for researchers. More and more 2D materials have been developed in the last few years, and new techniques such as mechanical exfoliation, chemical vapour deposition (CVD) and liquid-phase exfoliation have been used to prepare 2D materials. For example, graphene, the first 2D material, was initially prepared by mechanical exfoliation methods [119]. In that experiment, they used a simple adhesive tape to prepare desired materials. Later, this mechanical exfoliation method became popular among researchers because it is simple and has high-quality products. Although it was very simple, it was hard to get a large mass yield of uniform flakes this way. Moreover, lots of flakes containing different layers are randomly dispersed onto the substrates, and a time-consuming method is needed to sort them [120]. On the contrary, chemical vapour deposition (CVD) is also a useful method to prepare 2D materials, especially for large scale production on different substrates. Using the chemical vapour deposition method, Ambrosi et al. [121] prepared Bi_2Te_3, a thermoelectric with a 2D layered structure. Although the CVD method is suitable for large scale production, it requires expensive equipment and accurate control of experimental conditions, and there are many influential factors during the whole experiment [122]. As a result, many people consider it a complicated and expensive method. The liquid-phase exfoliation method has a high yield with minimal cost compared with mechanical exfoliation and chemical vapour deposition methods. It is possible to get a dispersion of smaller, thinner flakes from bulk powder using the liquid phase exfoliation method. Usually an alcohol is mixed with bulk powder and intense sonication is applied which cracks and disperses the bulk phase (precursor powder).

Exfoliated layered materials are optimal for some properties such as components in nanocomposites, applications requiring high specific surface area, catalysis, sensing, energy storage applications, and exotic electronic properties. Apart from primarily popular 2D layered materials such as graphene, transition metal dichalcogenides (TMDs), transition metal oxides (TMOs), other 2D compounds such as boron nitride, Bi_2Te_3, Bi_2Se_3, SnTe, and SnSe are also considered as prospective candidates for liquid-phase exfoliation to explore versatile properties [123]. In the first step, this chapter explored the sonication-based liquid-phase exfoliation method on Bi_2Te_3 to produce a precursor suitable for nanocomposite formation. Liquid-phase exfoliation methods are cost-effective, simple, and convenient for bulk production to provide high yields compared with other mechanical exfoliation methods.

5.1.2. Nanoinclusion of Bi_2Te_3 in polyurethane

Using a polymer with inorganic thermoelectric has become of interest to control thermal conductivity and produce flexible thermoelectric devices. Using a polymer matrix, it is possible to achieve ultra-low thermal conductivity of thermoelectric materials, which plays a vital role in obtaining high-performance thermoelectric. Care must be taken, however, to ensure electrical percolation of the thermoelectric compound so that electrical conductivity is retained. If a uniform distribution of the secondary particles can be achieved, homogenous filaments for 3D printing can also be developed. The latter typically requires a nanosized additive phase, such as those produced by liquid-phase exfoliation described in Section 5.1.1. Due to low-cost manufacturing, easy availability, and convenient manufacturing process, polymer: inorganic nanocomposites are becoming popular for laboratory and industrial uses, medical purposes, and so on. The work in this chapter explored the popular thermoelectric (Bi_2Te_3) combined with commercial polymer with the brand name Chronoflex. Moreover, polyurethane (Chronoflex) is a thermoplastic polymer with

a high melting point (~200 C), excellent chemical resistance, stability in cryogenic environments, low coefficient of friction, good impact resistance, excellent wear and fatigue resistant, and it is medically approved by the FDA/USDA [124, 125].

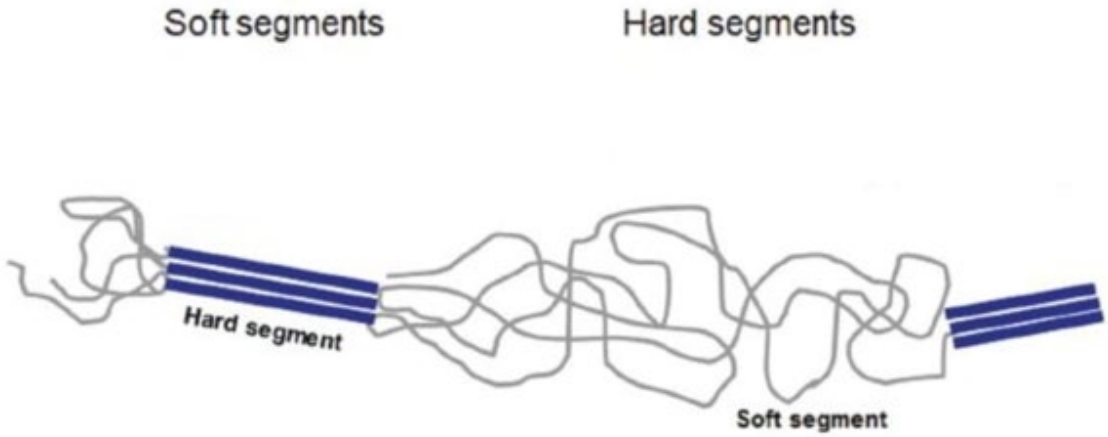

Figure 5.1: Segment of polyurethane (source: www.medicaldesignbriefs.com)

Polyurethane has two multi-block segments (Figure: 5.1). One is soft, and the other is hard, which means it has moderate hardness and excellent elasticity to develop promising flexible devices. Due to these characteristics, I consider it a promising candidate for heat management in future flexible thermoelectric devices and energy extraction applications using thermoelectric Bi_2Te_3. Due to the flexibility and stretchability of Bi_2Te_3-PU composites, such composites are potentially interesting for wearable thermoelectric devices and smart devices. The resulting composites were investigated by LFA, XRD, SEM and resistivity measurements.

5.2.Materials and methods

5.2.1. Materials

A bulk Bi_2Te_3 powder was used as the starting point to synthesise the exfoliated nanomaterials: Thermoelectric bismuth (III) telluride (Bi_2Te_3, 99.99%, 325 mesh, Sigma-Aldrich). This was exfoliated using a solvent: N-Methyl-2-pyrrolidone (NMP) (ChemSupply Australia).

5.2.2. Preparation of Bi_2Te_3 flakes

Initially, the required amount of bulk Bi_2Te_3 powder was ground using a mortar and pestle. Then, 10ml NMP was added to assist in further grinding the flakes. After 30 minutes of grinding, the resulting powder was transferred to a glass bottle with NMP for sonication.

5.2.3. Sonication for liquid phase exfoliation

The nanomaterials dispersion quality depends on processing parameters such as sonication time and proper solution with an appropriate solvent. After investigating various solvents, I have found NMP was effective. For this purpose, 0.5 g of ground Bi_2Te_3 and 20ml NMP were mixed in a glass jar. The solution was sonicated for 10 hours to get properly disperse Bi_2Te_3 in NMP. After sonication, I took the solution to a glass petri dish and then heated it at 70°C to evaporate NMP. All work was performed in a fume hood. After getting the sonicated dried Bi_2Te_3, I ground the film that was formed for 10 mins by using a mortar-pestle to obtain a fine powder. X-ray diffraction confirmed that the treated powder had a smaller crystallite size as expected, based on Scherrer analysis.

5.2.1. Solution-phase preparation of the Bi_2Te_3: PU composite

The exfoliated Bi_2Te_3 was mixed in a glass bottle with THF (see section 3.1.2), and similarly, polyurethane with tetrahydrofuran (THF) was also taken in a separate glass bottle. They were ultra-sonicated for 6-8 hours, and then the Bi_2Te_3+THF solution and polyurethane+THF solution were mixed in one glass bottle. Finally, the mixture was sonicated for 4 hours. The sonicated composite solution was moulded by pouring it into a petri dish. The THF solvent was evaporated via airflow over the dish.

5.2.2. Composites preparation for laser flash analysis measurements.

The final flexible composites film was cut into small pieces and mounted in a square ($1cm^2$) aluminium holder. Then using a manual heat press technique, samples were heated for a minute at about 142°C temperature to get a glass transition state of the polymer composites. Composite pieces were kept under approximately 6 kg/m^2 pressure during this heating process (Figure: 5.2). Then the sample was taken out from the device and was kept under 6 kg/m^2 pressure for 5 minutes during the cooling process. Finally, the sample obtained the desired density.

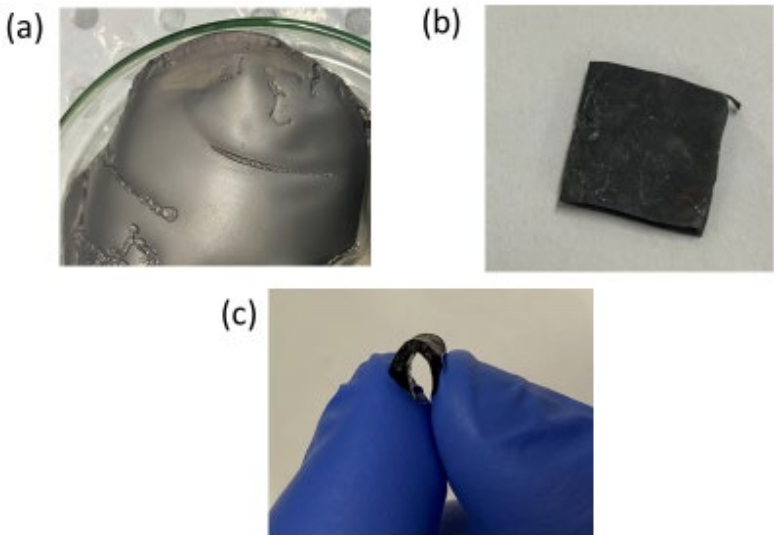

Figure 5.2: Bi_2Te_3-PU composite and its flexibility. (a) Flexible (0.3-1 mm) as-cast product before heat press. (b) Heat pressed sample for thermal conductivity measurements. (c) Heat pressed sample's flexibility.

5.3.Experimental section

X-ray diffraction (XRD) patterns of the raw Bi_2Te_3, exfoliated Bi_2Te_3 and Bi_2Te_3-PU composite samples were measured with an Empyrean diffractometer (Malvern Analytical) using monochromatic Cu Kα radiation (λ=1.54178 Å). The scanning angle (2θ) ranged between 10-90 degrees at 40 kV and 40 mA with a scan speed of 0.0954° per second and a step size of 0.0286°. Match 3 and PDF-4 + 2020 RDB software was used to analyse the measured data.

Scanning electron microscopy (SEM) (JEOL JSM-6490LV electron microscope) was used to reveal morphology and to perform energy dispersive spectroscopy (EDS) mapping. The samples were pre-coated with platinum using an Edwards sputter coater to avoid charging during this process. The Aztec software suite (version 4.2) was used to analyze the EDS data.

Laser flash analysis (Linseis LFA 1000) was used to understand the thermal behaviour of neat polyurethane, Bi_2Te_3-PU composites and pure Bi_2Te_3 crystal. The experiment was done under vacuum conditions at room temperature.

5.4.Results and discussion

The most crucial task was to determine the best solvent for Bi_2Te_3 for the liquid phase exfoliation step. A successful solvent must fulfil two criteria.

- It must be able to disperse/suspend the material for a reasonable amount of time.
- The dispersed material must be highly exfoliated.

During my experiments, I have tried to focus on fulfilling both criteria. In the beginning, I tried several solvents to check which one fulfilled the first criteria. I have used isopropanol, ethanol, THF, water, and NMP to finalize the right solvent. Then I have done XRD analysis with crystallite size analysis (via a Scherrer calculation) to check the second criteria. After experiments with several solvents to disperse Bi_2Te_3, it is observed that only NMP can fulfil both criteria.

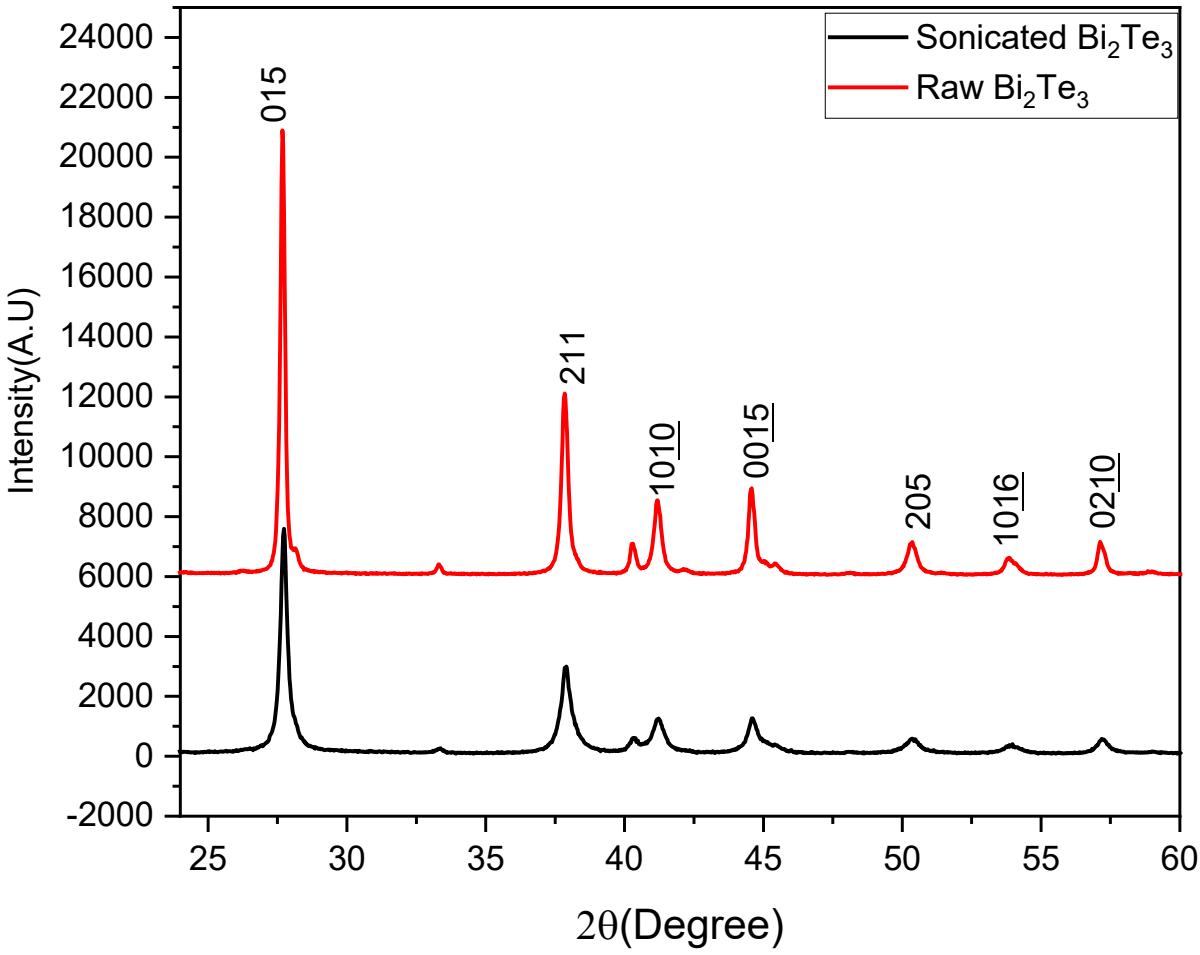

Figure 5.3: XRD analysis and crystallite size calculation on exfoliated and untreated Bi_2Te_3.

The X-ray diffraction patterns in Figure 5.3 indicated that the Bi_2Te_3 particles have the expected crystallographic phase before and after the exfoliation of nanopowders. The average crystallite size of Bi_2Te_3 was 102.7nm (including microstrain) before exfoliation. After exfoliation, the

crystallite size turns 37.6nm (including microstrain). The crystallite size calculation has been determined using Scherrer analysis (equation: 5.1). From Figure 5.3, it's clearly indicated that the average crystallite size decreased to below 50 nm based on the additional broadening. This can be quantified using the formula:

$$D = \frac{K\lambda}{\beta Cos\theta} \qquad 5.1$$

Where,

D = Crystallite size (nm)

K = 0.9 (Scherrer constant)

λ = 0.154 nm (wave length of X-ray source)

β = Full width half maxima (FWHM) broadening (radians)

θ = Peak positions (radians)

Even from Figure 5.4, we can see that the peak has been broadened, and the grain size has been decreased on average below 50 nm (Figure 5.3). However, the grain size (102.7nm before exfoliation and 37.6nm after exfoliation) has been calculated using the Scherrer equation (equation 5.1). Additionally, from Figure 5.4, it is seen that the peak (015) has been slightly shifted, implying a very small change in the lattice constant which is difficult to resolve accurately within the current instrument resolution. For the rest of the peaks, there is no observable shift.

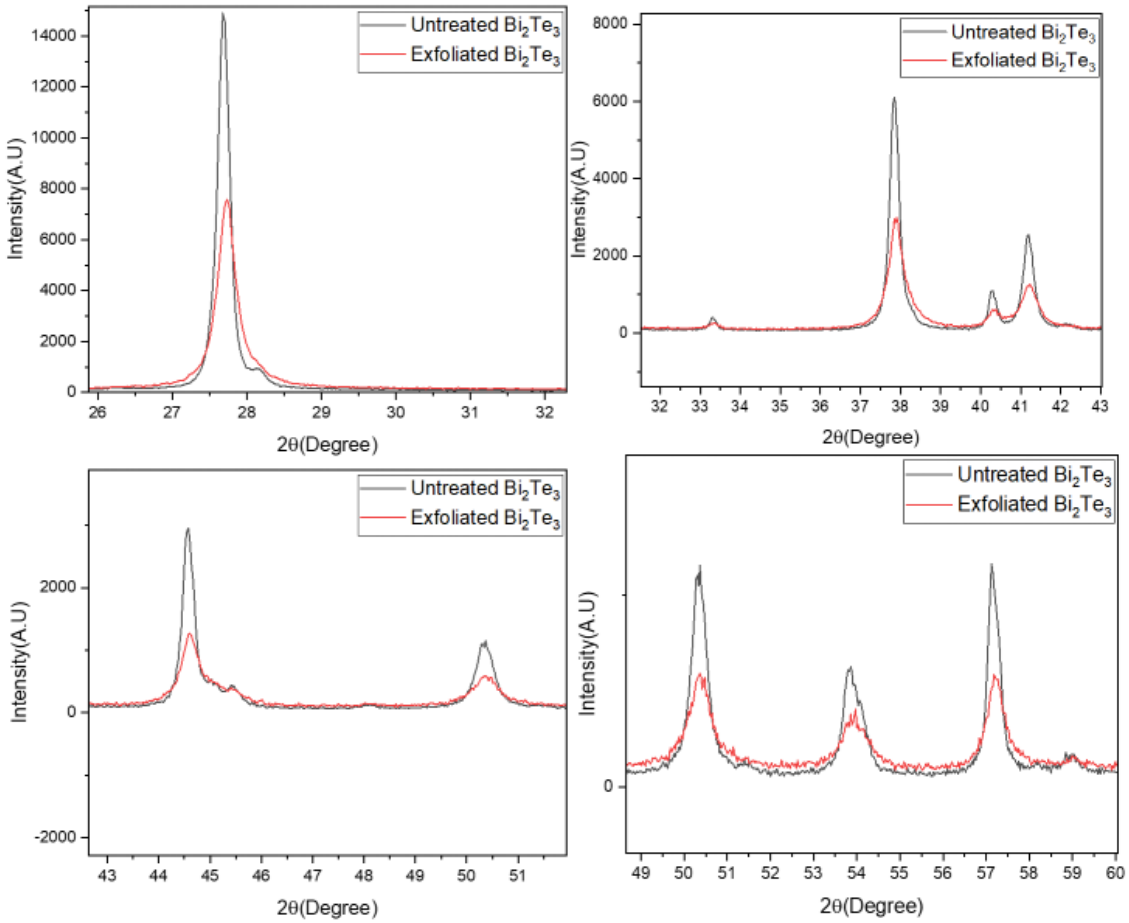

Figure 5.4: Peak broadening analysis of liquid-phase exfoliation on Bi_2Te_3.

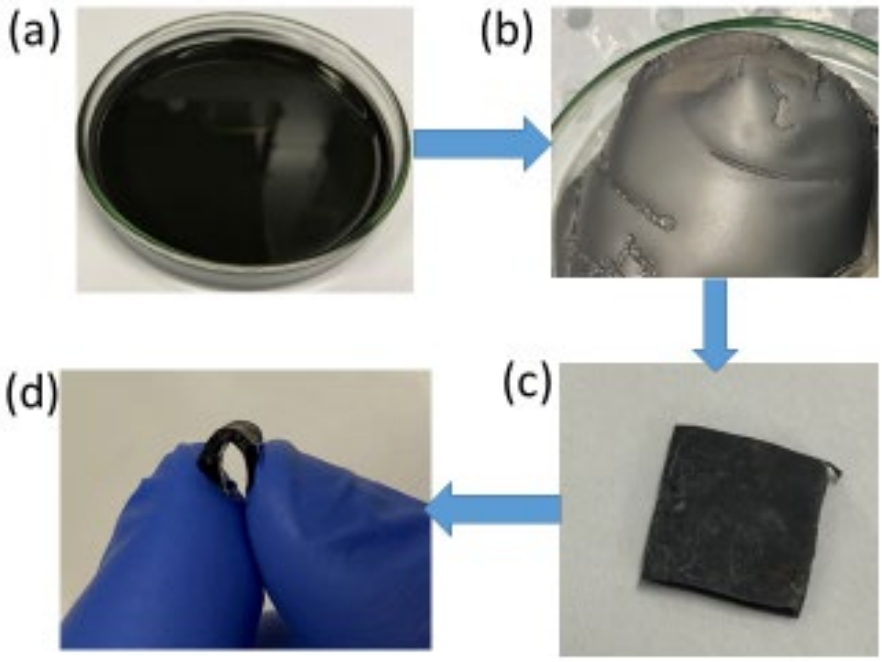

Figure 5.5: Bi_2Te_3-PU composite and its flexibility. (a) Final composite solution. (b) Flexible (0.3-1 mm) thick flexible final product. (c) Heat pressed sample for thermal conductivity measurements. (d) Heat pressed sample's flexibility.

Figure: 5.5 illustrates the transformation of the solvent into flexible composites. The final product is flexible even after heat presses densification.

After the combination with the PU, the X-ray diffraction patterns are shown in Figure 5.6. They indicate that the Bi_2Te_3 particles retained their crystallographic phase during processing steps into the Bi_2Te_3: PU composites. All the Bragg peaks above 25 degrees (Figure: 5.6) are present in the pure Bi_2Te_3 nanopowder and Bi_2Te_3: PU composites. This implies the exfoliated Bi_2Te_3 particles maintain their crystallographic form during processing and can be indexed to Bi_2Te_3 (Crystallography Open Database 96-101-1121). Moreover, there is no dependency between the peak broadening and the change of concentration of Bi_2Te_3 in polyurethane, which can be confirmed in Figure 5.6.

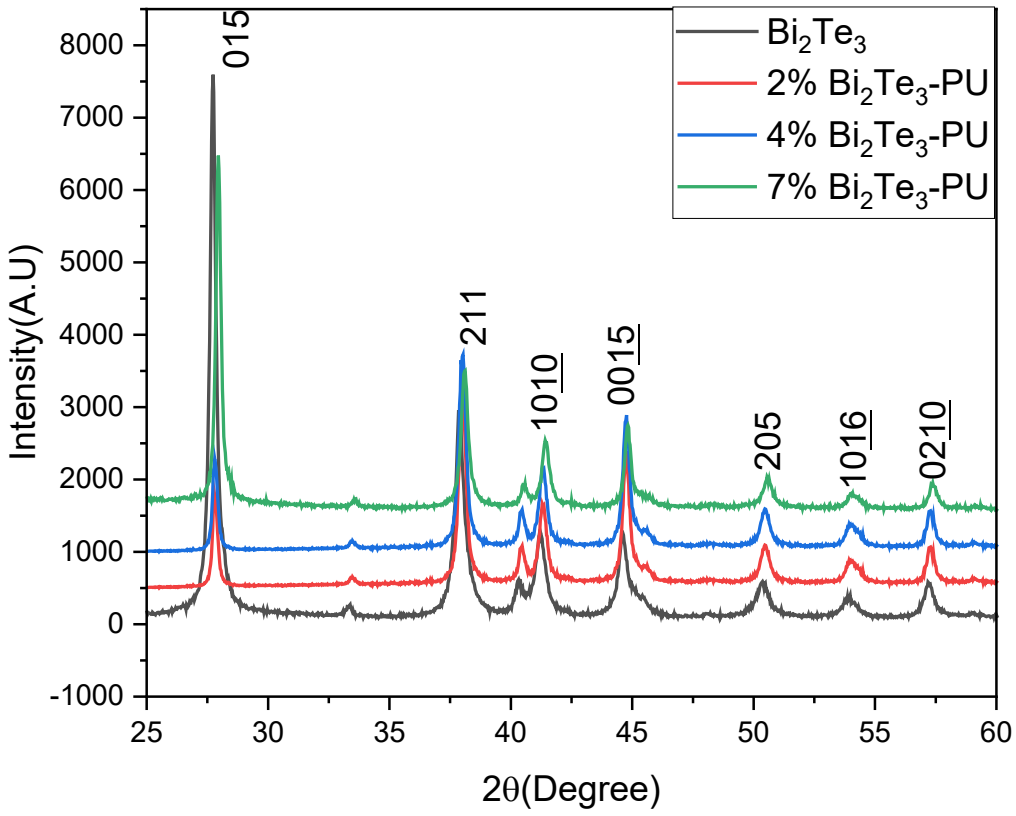

Figure 5.6: XRD pattern of Bi_2Te_3-PU nanocomposites. (the black pattern shows the pure Bi_2Te_3 nanopowder, red indicates the 2 v.% Bi_2Te_3-PU composite, the blue pattern is for the 4 v.% Bi_2Te_3-PU, the olive pattern for the 7 v.% Bi_2Te_3-PU.

Scanning electron microscopy was performed on the sample surfaces to assess the uniformity and distribution of the Bi_2Te_3 nanoparticles incorporated into the PU. This was combined with the EDS technique to perform the elemental mapping. Figures 5.7 a and b show the surface of the 2% and 7% Bi_2Te_3: PU composites. Overlaid in Figure 5.7 c and d are the Bi and Te EDS maps, showing the relatively uniform distribution of the Bi and Te, particularly in the more highly loaded sample. From Figure 5.7, we can see that the distribution of Bi_2Te_3 is uniform in the surface area of polyurethane; however, the relatively rough surface introduces some topological artifacts into the

EDS map-making accurate quantification impossible. A lower distribution is observed in the lower nano included composites, whereas more Bi_2Te_3 particles can be seen in the highest % containing composites.

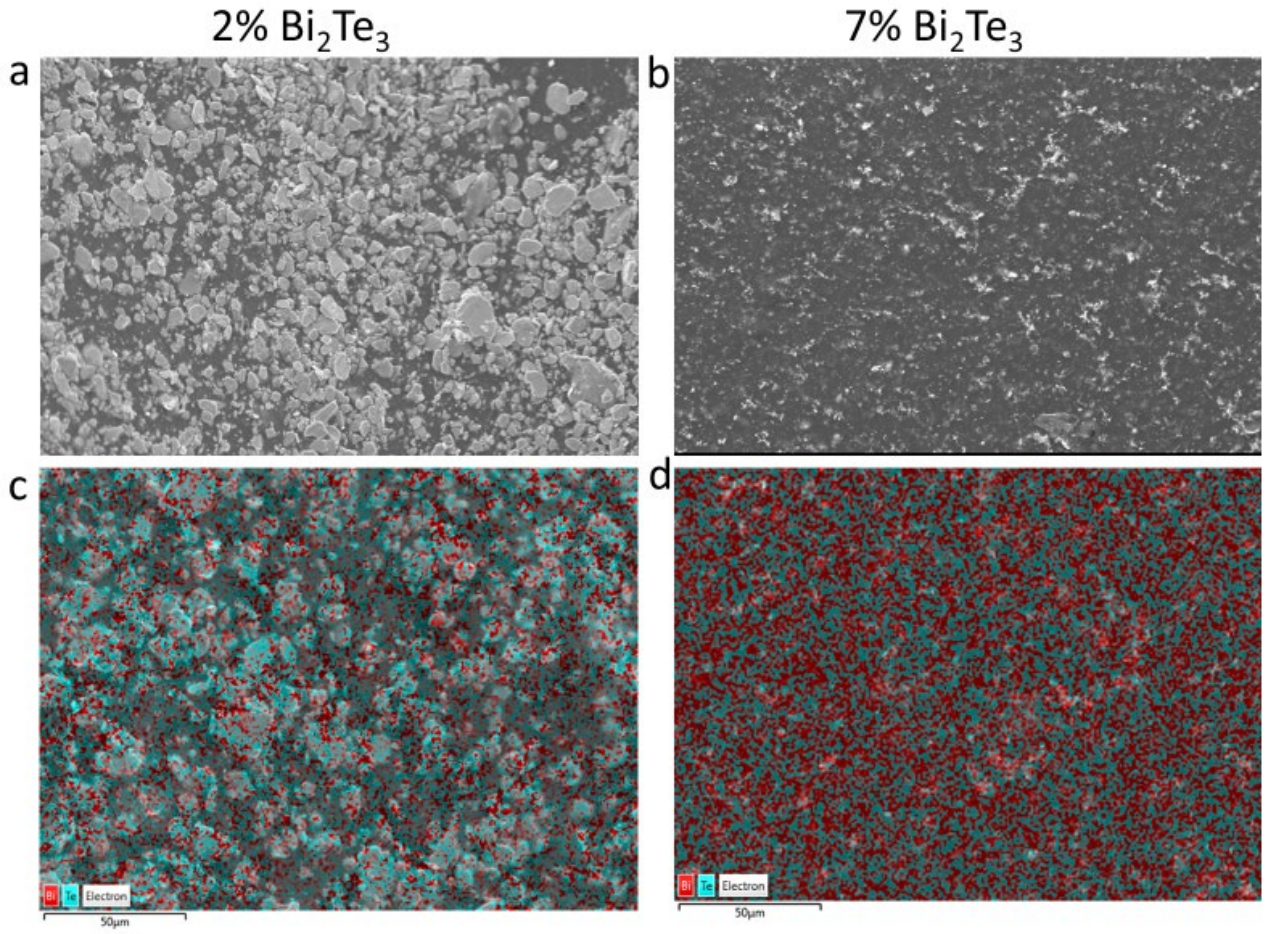

Figure 5.7: Plane-view low magnification SEM and EDS images of the composites. (a), and (b) indicates SEM image of 2 v% and 7% Bi_2Te3-PU composites, where (c) and (d) reveal Bi_2Te_3 dispersion for 2 v% of Bi_2Te_3-PU and 7 v% Bi_2Te_3-PU composites.

Laser flash data analysis has been done to quantify the thermal diffusivity of the composites. Several fitting methods were compared to find the best fitting models and avoid experimental errors during measurements. Figures 5.8 and 5.9 show that the dedicated combined model showed

100% data fitting, whereas the adiabatic showed 4.4% less fitting, and the finite pulse method showed 5.12% less accurate fitting than the combined model. The combined model is more reliable than any other model. It gives more accurate fitting than the adiabatic, finite pulse, and heat loss models as it combines several correction terms. Figures 5.8 and 5.9 are the 7% Bi_2Te_3-PU composite data at room temperature. All the data analysis has been done using baseline slope fitting with 25 filter points to obtain accurate fits.

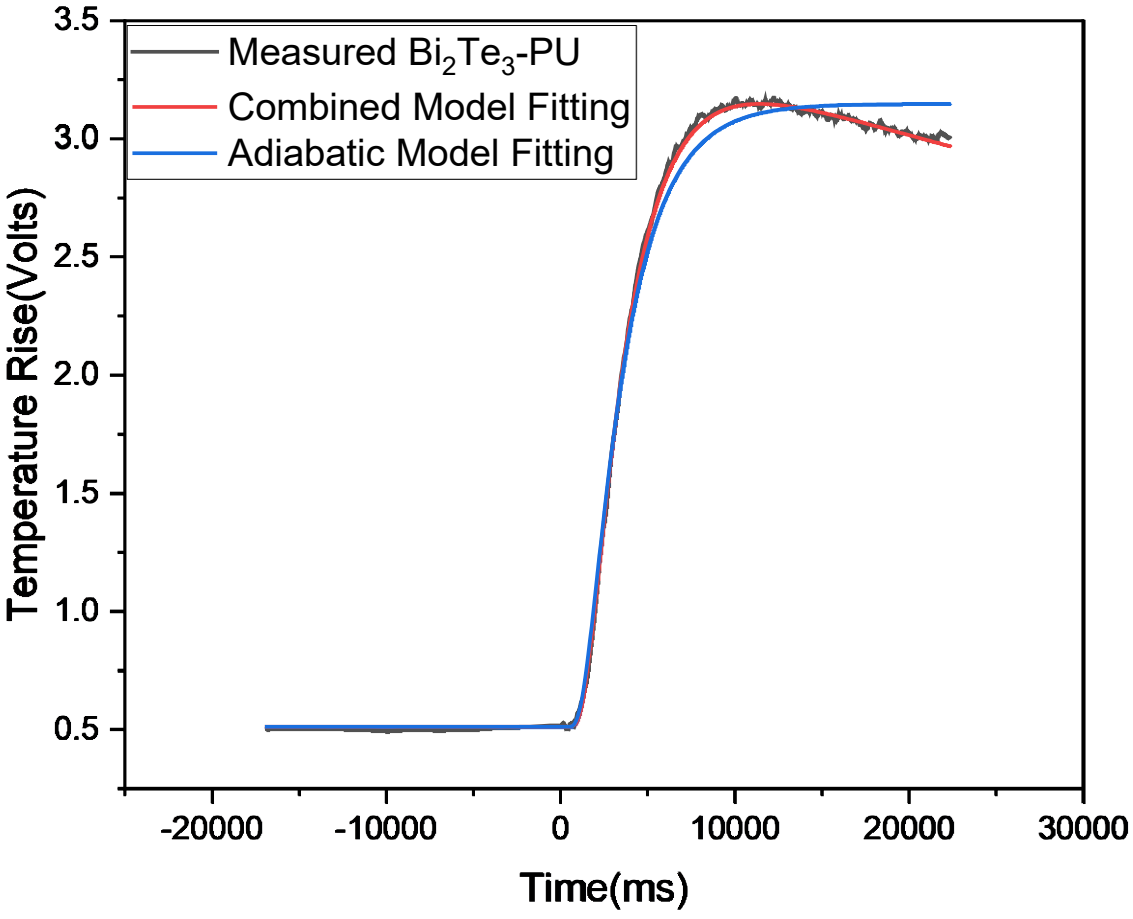

Figure 5.8: 7% Bi_2Te_3-PU LFA data comparison at room temperature between the adiabatic and combined models

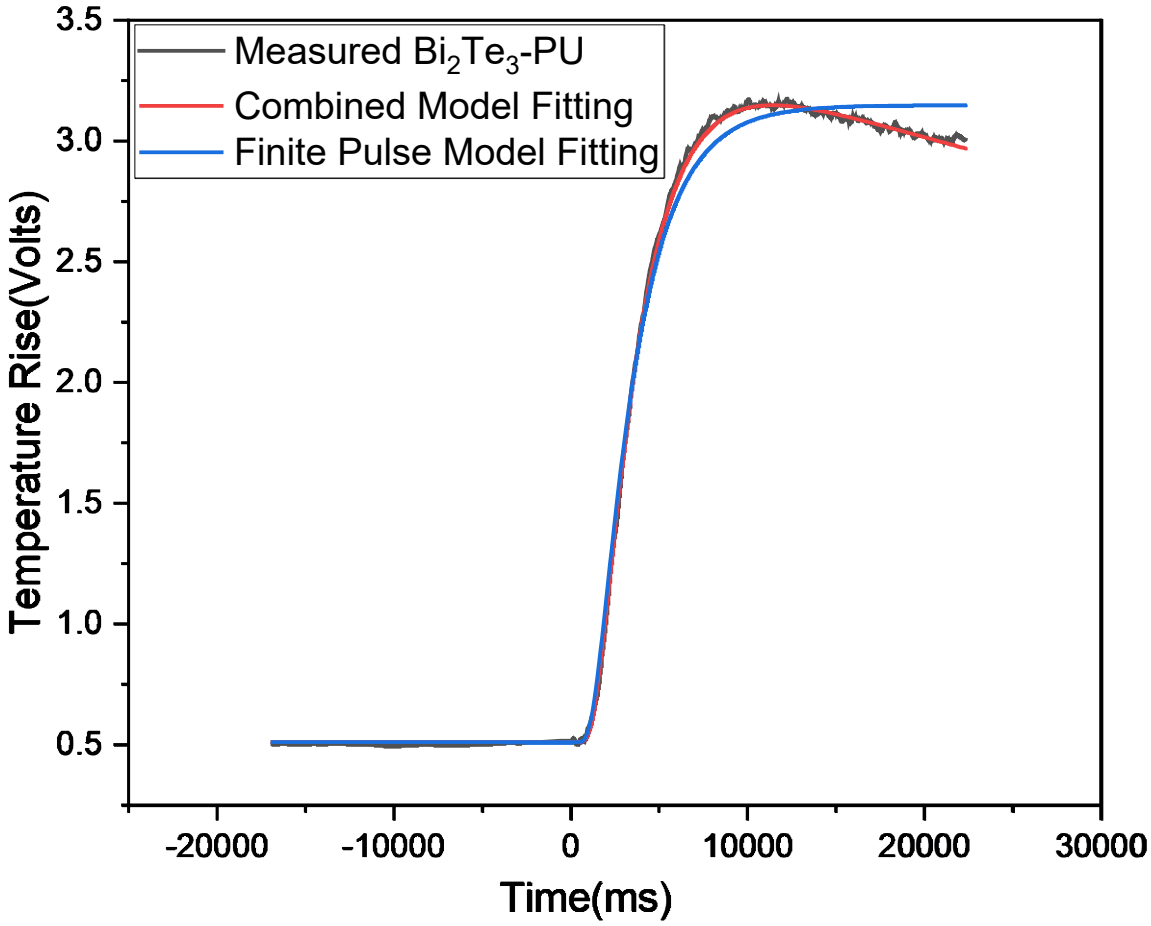

Figure 5.9: 7% Bi_2Te_3-PU LFA data comparison at room temperature between the finite pulse and combined models.

Laser flash analysis was used to conduct thermal conductivity analysis on neat PU and Bi_2Te_3-PU and pure Bi_2Te_3 crystal samples. All the measurements were performed under vacuum conditions, and the experiments were done at room temperature. The Bi_2Te_3-PU composites showed a clear trend in their thermal transport properties. There is a significant reduction of thermal conductivity relative to the single crystal, exactly as 94% in 2 v% Bi_2Te_3-PU, 93% in 4 v% of Bi_2Te_3-PU, and 87% in 7 v% Bi_2Te_3-PU composites. Figure 5.10 illustrates the trend of descending order of thermal conductivity among composites, and Table 5.1 provides the actual thermal conductivity values measured.

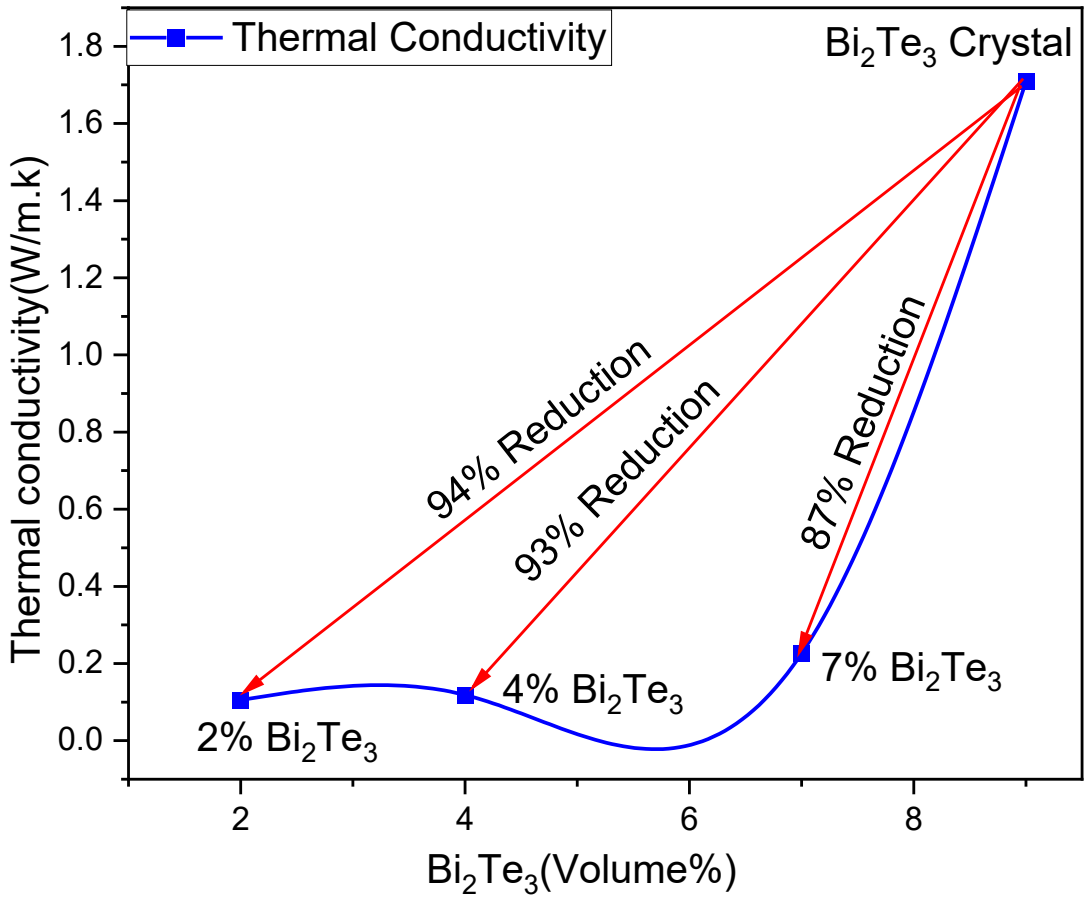

Figure 5.10: Summary of thermal conductivity on 2%, 4%, 7% (V%) Bi_2Te_3-PU and Bi_2Te_3 crystal.

According to the Law of Mixtures, the Bi_2Te_3-PU composites' thermal conductivity is lower at lower volume percents, shown in the red trend line in Figure 5.11. Although this captures the trend, the composites actually show a considerable additional decrease in thermal conductivity than the expected outcome. For instance, 2% Bi_2Te_3-PU thermal conductivity reduction has a 16% lower thermal conductivity compared to the Law of Mixture prediction. The result for 4% Bi_2Te_3-PU composites is 24% lower than the expected thermal conductivity (calculated from the Law of Mixtures). This suggests the "Law of Mixtures" neglects some important physical effects.

Regardless, these composites can be considered prospective candidates for highly efficient future flexible thermoelectric devices or for low thermal conductance substrates.

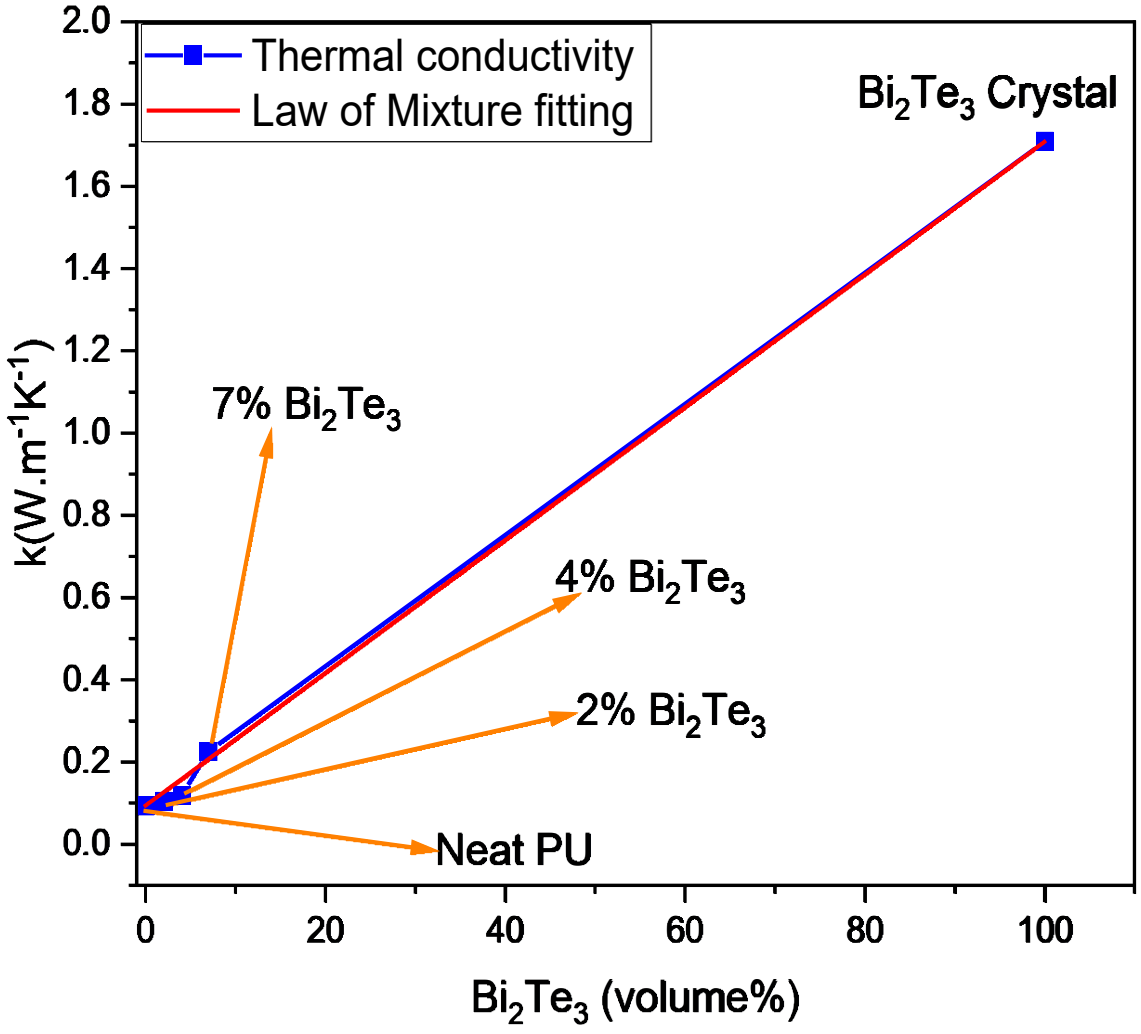

Figure 5.11: Thermal conductivity analysis of Bi_2Te_3 crystal, Bi_2Te_3-PU composites and neat polyurethane compared with the Law of Mixtures.

Table 5.1: The calculation of thermal conductivity of Bi_2Te_3-PU composites

Measurements / Sample	Density (kg/m^3)	Heat Capacity (J/kg.k)	Thermal diffusivity (m^2/s)	Thermal conductivity ($W.m^{-1}.K^{-1}$)	The error of thermal conductivity	Thermal conductivity reduction %
Neat PU	932.79	983	1.02E-07	0.0935	8.94E-7	-
2% Bi_2Te_3-PU	969.57	1013.92	1.07E-07	0.1052	7.87E-7	94
4% Bi_2Te_3-PU	1003.0	1056.31	1.12E-07	0.1187	1.53E-06	93
7% Bi_2Te_3-PU	1369.10	1258.85	1.31E-07	0.2257	7.07E-7	87
Bi_2Te_3 Crystal	7600	126	1.78E-06	1.7089	2.88E-02	-

To measure the impact on the electrical properties, I have attempted to measure the resistivity; however, the composites showed a high resistivity exceeding 10M Ω/cm. Further studies are needed to enhance the electrical conductivity by exploring additional dopants or an intrinsically conductive polymer matrix. Nevertheless, the basic methodology used in this chapter could be applied similarly to explore other polymers and nanodopants as a route toward high performing flexible thermoelectrics.

5.5.Conclusion

The inclusion of 2D Bi_2Te_3 into polyurethane has shown a promising trend in the case of controlling the combined thermal conductivity of Bi_2Te_3 and the polyurethane matrix. The main reason for reducing the thermal conductivity of Bi_2Te_3 in the polymer matrix is the amorphous structure of the polyurethane which provides an intrinsically low thermal conductivity, as described in Section 2.2.2. At 2% Bi_2Te_3 inclusion, the experiments showed that composites reduced the thermal conductivity by a maximum of 94% compared to a Bi_2Te_3 crystal. In summary, the composites tuned thermal conductivity with their embedded Bi_2Te_3 % into polyurethane. From the result, it can be said that the minimal inclusion of Bi_2Te_3 into polyurethane is a way to achieve the lowest thermal conductivity of Bi_2Te_3 composites, which is one of the criteria to produce high-performance thermoelectric generators. Though the electrical conductivity was not noticeably improved with the filler inclusion, further studies will be focused on improving the composites' electrical conductivity.

Chapter 6: Interplay between thermal, electronic and magnetic properties of polymer nanocomposites with superparamagnetic Fe_3O_4 nanoparticles

6.1.Introduction

Researchers and industries are continuously looking for multifunctional materials that can be used in different environments for various purposes. This chapter explores a Fe_3O_4/polymer composite that could potentially be useful in several contexts ranging from human health applications to inductive heating and thermoelectricity. Producing materials covering a wide range of applications is challenging due to their various requirements, such as being medically approved and non-toxic. As Fe_3O_4 and polyurethane (Chronoflex) are FDA approved for medical use, non-toxic and environmentally friendly, they offer attractive options. This section aimed to apply similar methods to those developed in the earlier chapters to produce a composite that enables magnetic functionality, including induction, actuation, remote heating (potentially for killing pathogens) and modified thermal/electrical conductivity for future thermoelectric devices. Previously, T. Kajitani et al. [126] explored $CuFeO_2$ and Fe_3O_4 to create low thermal conductive devices for thermoelectric applications, where they have found a dramatic decrease in the thermal conductivity at temperatures below 500K. Another study found that the Seebeck coefficient of the Fe_3O_4/$Bi_{0.5}Sb_{1.5}Te_3$ nanocomposites increased remarkably. At the same time, the thermal conductivity significantly decreased because of the multiple carrier scattering and the enhanced phonon scattering induced by the Fe_3O_4-NPs, respectively [127]. Despite producing low thermally conducting devices with higher electrical performance, those composites were unfit for medical devices as Cu, and $Bi_{0.5}Sb_{1.5}Te_3$ are toxic. Keeping this in mind, non-toxic Fe_3O_4 and polyurethane are considered worthwhile candidates for further exploration.

Aside from possible TE effects, magnetic composites offer some additional novel possibilities. Alternating magnetic fields have the ability to heat magnetic objects remotely over large distances without requiring physical contact. Many industrial and medical processes use or produce such magnetic fields as a byproduct. Using an AC magnetic field, or the mechanical oscillation of an element through a DC magnetic field, it is possible to convert energy into heat. Combining magnetic elements with thermoelectrics is, therefore, an interesting concept for dual inductive-TE modules. The underlying heating phenomenon is induction, where a time-varying magnetic field induces dissipative current motion (in metals) or magnetization dynamics (in a non-metallic magnet). Unlike other forms of remote heating, such as microwaves, magnetic fields are also transmitted through the body as water and insulators are effectively transparent. This method for remote heating is the basis of magnetic hyperthermia treatment involving killing cancer cells by heating to above 40^{o} C using injected magnetic nanoparticles. Thus magnetic composites could be used in a variety of contexts, including as a way to kill pathogens or generate heat/electricity in medical settings.

Purely magnetic induction using a magnetic insulator has the advantage that it does not require eddy currents and, therefore, can occur using ultra-small regions surrounding a nanoparticle embedded in an environment. In addition to induction, magnetic fields can also cause the mechanical displacement of magnetic nanoobjects, and this offers other potential modalities to achieve heating via friction and enables magnetic guidance of objects. Seeking to broaden the application of magnetic Fe_3O_4 composites, several recent studies have explored how superparamagnetic iron oxide (SPIO) magnetic nanoparticles can be incorporated in a variety of matrices, including gels, polyaniline, fluids, synthetic talc, polylactic acid (PLA), polyurethane, and naphthalene diisocyanate [128-132]. In this context, high-temperature polymers, such as

polyurethane, are attractive as they potentially enable moulding and additive manufacturing of robust components. Several custom-designed polymer/particle composites have been developed with a view toward applications in biomedical contexts or soft robotics, with ongoing work to optimize the key properties (usually porosity, mechanical strength or thermal conductivity) [133, 134]. A high-temperature plastic with high magnetic susceptibility is required for targeted field-heating applications. Lin et al. [135] have tuned thermal conductivity 101% higher than pure solid-solid phase change materials(SSPCMs) using Fe_3O_4. In another study, Sundar et al. [136] improved the thermal conductivity by 48% using 2 v% nano inclusions at 60 °C temperature. Therefore, the inclusion of Fe_3O_4 in polyurethane has versatile opportunities along with its remote heating capability.

Such composites may also be suitable for additive manufacturing. Additive manufacturing, which includes techniques such as 3D printing, has a number of emerging medical and industrial applications, including recreating anatomic models, patient-specific custom implants, prosthetics, orthotics and bone or cartilage bioprinting as well as wearable thermoelectric devices [133]. There is also a growing interest in so-called “4D printing”, where an additional variable (e.g. time, heat, magnetic field) can be controlled to allow the part to change shape or functionality in response to a specific stimulus. The commercially available magnetic plastic composites for 3D printing are generally based on PLA polymers that are vulnerable to degradation/melting at relatively low temperatures, making them unsuitable for high-temperature (or long-term applications in the body). Polyurethane (PU) is more suitable in this regard; however, to the best of our knowledge, no studies directly report the heating efficiency of magnetic polyurethane composites using alternating magnetic fields and thermal transport techniques concurrently. This chapter reports a new type of polyurethane magnetic composite based on a biocompatible, high melting point

polyurethane thermoplastic (trade name 'ChronoFlex C®'), which is also currently one of the materials of choice for 3D printing specialised components

6.2. Methods

6.2.1. Synthesis

The following components were used to synthesize the magnetic and thermally conductive plastics: superparamagnetic iron oxide nanopowder (Fe_3O_4, 99.9%, 8 nm, US Research Nanomaterials Inc.), polyurethane (PU) (ChronoFlex C®, AdvanSource Biomaterials) [137], Tetrahydrofuran (THF) (ChemSupply Australia) [137]. Fe_3O_4 nanopowders (SPIO) were weighed and dispersed in glass bottles with 10 mL THF. The PU pellets were placed in separate glass bottles with 20 mL THF per gram PU. The solutions were sonicated for 6-8 hours. When the PU pellets and Fe_3O_4 nanopowders were dispersed properly, the two solutions were mixed with weights 10:100, 15:100, and 20:100 of Fe_3O_4: PU (for theoretical weight percentages of 9, 13.1 and 16.6 wt. %, respectively). The resulting mixture was sonicated for an additional 4 hours to ensure that the Fe_3O_4 nanopowder was dispersed uniformly into the solution. Finally, the sonicated composite solution was cast moulded by pouring it into a petri dish, and the THF solvent evaporated via airflow over the dish, ultimately resulting in Fe_3O_4: PU composite flexible films with a thickness of (0.3-1) mm.

6.2.2. Preparing samples for laser flash analysis

The final flexible composites films were cut into small pieces and mounted in a square (1 m^2) aluminium holder. Then using a manual heat press technique, samples were heated for a minute at about 142°C temperature to melt the polymer composites. Composite pieces were kept under approximately 6 kg/m^2 pressure during this heating process (Figure: 6.1). Then the sample was

taken out from the devices and was kept under 6 kg/m^2 pressure for 5 minutes during the cooling process to obtain the desired density.

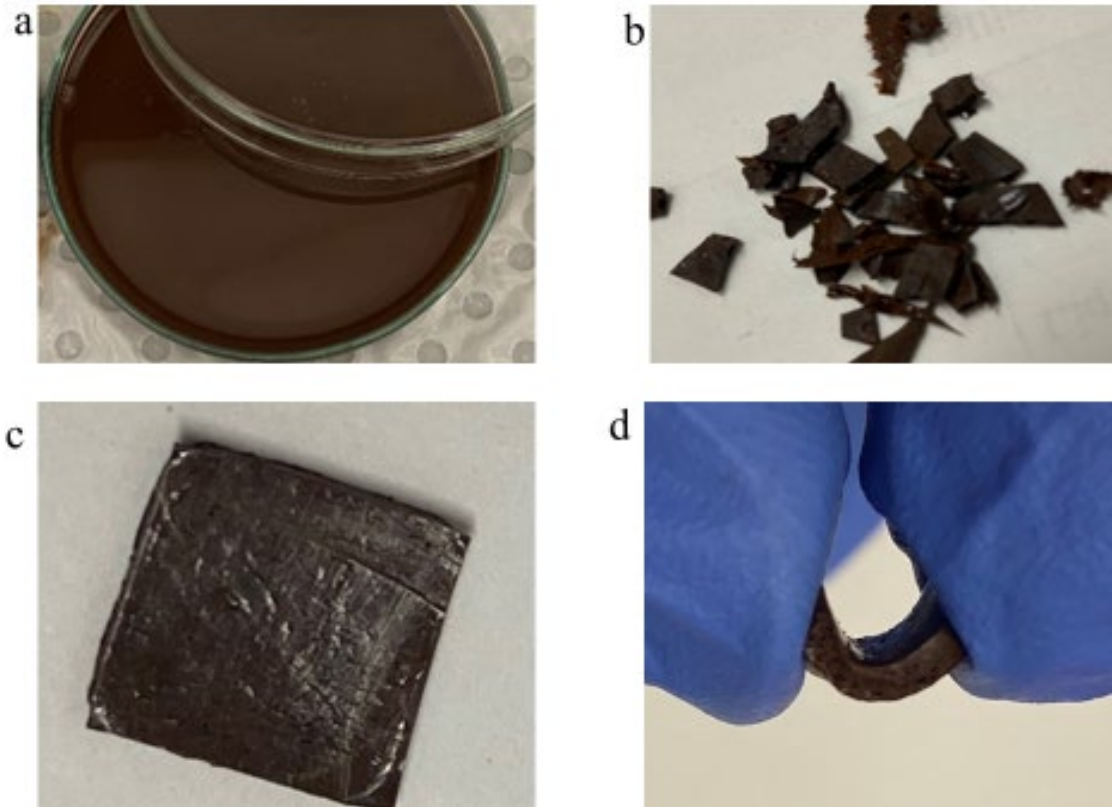

Figure 6.1: Sequence of photos showing how the sample was transformed into a form suitable for laser flash analysis. (a) initial flexible composite film produced after solvation and casting, (b) small pieces of flexible composites cut from the film, (c) Dense sample for LFA analysis formed from heat pressing the small pieces, (d) flexibility of the final sample.

6.2.3. Characterization

X-ray diffraction (XRD) patterns of the Fe_3O_4, PU, and the composite samples were measured with an Empyrean diffractometer (Malvern Panalytical) using monochromatic Cu Kα radiation (λ=1.54178 Å). The scanning angle (2θ) ranged between 10-90 degrees (°) at 40 kV and 40 mA

with a scan speed of 0.0954° per second and a step size of 0.0286°. The Match 3, PDF-4 + 2020 RDB software was used to analyse the measured data.

Scanning Electron Microscopy (SEM) (JEOL JSM-6490LV) was used to reveal the morphology and to perform energy dispersive spectroscopy (EDS) mapping. The samples were pre-coated with platinum by using an Edwards Sputter Coater to avoid charging during this process. The Aztec software suite (version 4.2) was used to analyze the EDS images.

A Physical Property Measurement System (PPMS) (Quantum Design, USA) was used to measure the magnetic properties of the Fe_3O_4: PU composites by employing the vibrating sample magnetometry (VSM) option. The sample was mounted on a low-background quartz holder with a small amount of Kapton tape, positioned to give a uniform (cancelling) diamagnetic background to conduct the measurements.

Transmission electron microscopy (TEM) (JEOL JEM 2010) was used to reveal the crystallinity and size distribution of the nanopowder. The brightfield TEM images were analyzed using the Gatan Digital Microscopy Suite (Version 2.32.888.0).

Laser flash analysis (Linseis LFA 1000) was used to understand the thermal conductivity of the neat polyurethane and Fe_3O_4-PU composites. The experiment was done under vacuum conditions at room temperature.

AC Inductive Heating: A custom apparatus was developed to investigate targeted heating of the Fe_3O_4: PU composites via an AC inductive heating process. The apparatus was based on a Geekcreit (maximum 1000 W / 20 A) induction heater, consisting of an 8-turn hollow copper tube induction coil (inner diameter 4.33 cm), operated at a frequency of 85 kHz. A 30 V power source

(GW INSTEK PSM 3004) was used to energize the coil with a current range of 3.6 - 3.8 A, producing a magnetic field amplitude in the range 5 – 10 Oe. A long quartz vial, encased in thermally-isolating polystyrene, was centred within the induction coil as a sample holder. A photograph of the apparatus is shown in an inset in the results section. A fixed mass of 3.66 g of the Fe_3O_4: PU composite was used for each experiment. The composites were inserted into the vial, and 15 mL of distilled water was also included. The water served dual purposes, to aid in heat transfer and to minimise thermal gradients across the sample, and to transfer the sample temperature to a position outside significant influence of the induction coil magnetic field, where a thermocouple (k type) was placed to measure the water (and by extension the Fe_3O_4:PU composite sample temperature). A custom LabVIEW (National Instruments, Version 2011) program was developed to log sample temperature at a ten-second interval. To minimise convection heat transfer from the copper coil to the sample, active cooling of the induction coil was achieved by flowing cooling water through the hollow void in the induction coil conductor – ensuring joule heating did not result in the coil's temperature rising above ambient. A benchtop multimeter (Keithley 2000) was used to read the sample's temperature.

Experiments consisted of starting with the sample/water mix at ambient temperature, then commencing logging and energizing the induction coil, and allowing the system to normalize at a final temperature representative of the balance of heat influx into the system through magnetic heating of the sample, and heat outflow from conduction and convection heat transfer to the ambient laboratory space. Control measurements were performed on pure water and pure PU.

6.3.Results

The X-ray diffraction patterns are shown in Figure 6.2 and indicate that the Fe_3O_4 particles retained their crystallographic phase during processing steps into the Fe_3O_4: PU composites. All the Bragg peaks above 30 degrees in the pure Fe_3O_4 nanopowder and Fe_3O_4: PU composites can be indexed to Fe_3O_4 (Crystallography Open Database 96-900-2320). A single broad feature between 15–30 degrees is the characteristic "peak" of the pair distribution function of the amorphous polyurethane, and it appears both in the neat PU and in the Fe$_3$O: PU composites.

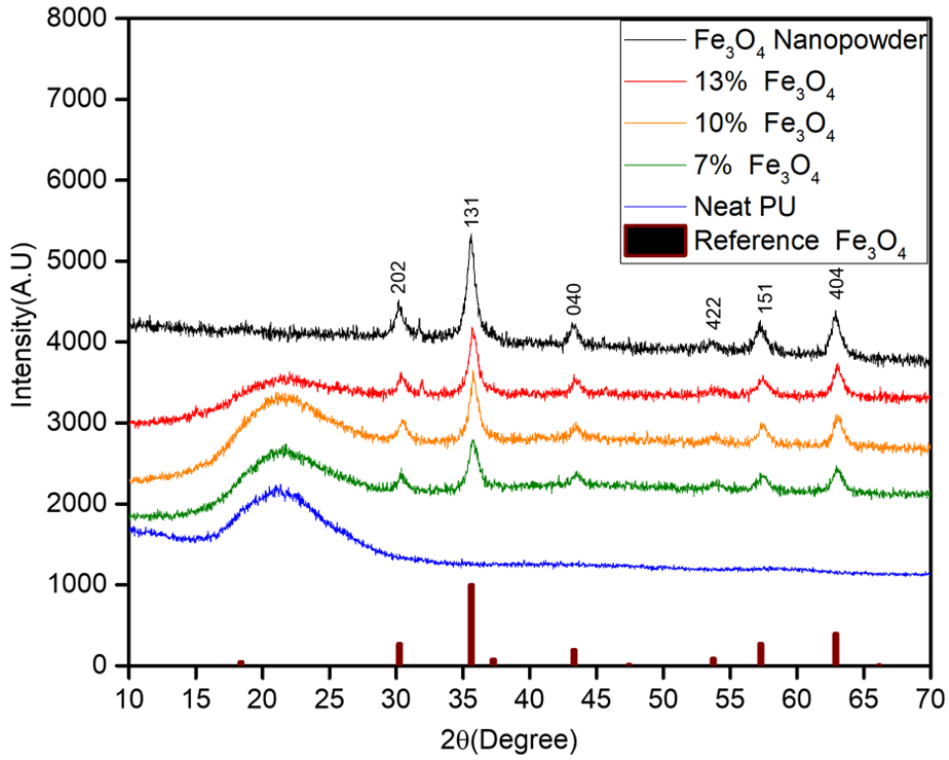

Figure 6.2: XRD pattern of Fe_3O_4-PU nanocomposites. The black pattern shows the pure Fe_3O_4 nanopowder, red indicates 13 wt.% Fe_3O_4-PU composite, the orange pattern is for 10 wt.% Fe_3O_4-PU, the olive pattern is for 7 wt.% Fe_3O_4-PU, the blue pattern indicates neat polyurethane; the bars show the reference pattern of Fe_3O_4 (COD:96-900-2320).

The average size of the Fe_3O_4 nanoparticles in the nanopowder was measured via transmission electron microscopy, and some representative images are shown in Figures 6.3a and b. The histogram of the particles sizes is shown in Figure 6.3c, indicating the average size was 9.5 ± 2.0 nm, in agreement with the supplier's nominal specifications.

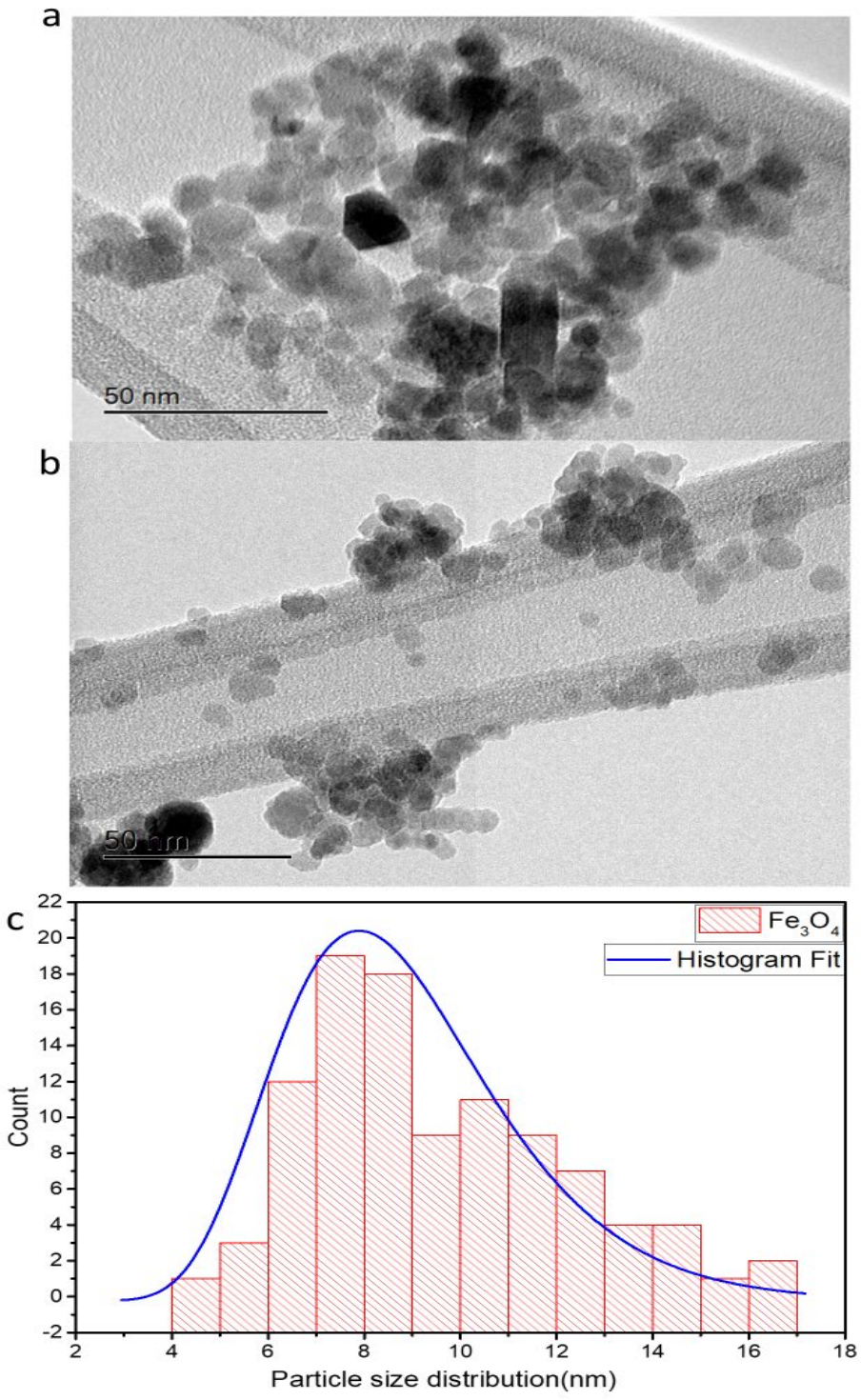

Figure 6.3: Transmission electron microscopy images of Fe_3O_4 nanopowder. (a) and (b) are the TEM images of the nanoparticles at two different positions on the carbon grid. (c) is the particle size distribution histogram of the Fe_3O_4 nanopowder.

Scanning electron microscopy was performed on the sample surfaces to assess the uniformity and distribution of the Fe_3O_4 nanoparticles incorporated into the PU. This was combined with the EDS technique to perform the elemental mapping. Figure 6.4 shows the surface of the 13% and 7% Fe_3O_4: PU composites, and overlaid in Figures 6.4c and 6.4d are the Fe EDS maps, showing the relatively uniform distribution of the Fe (particularly in the more highly loaded sample). The Fe is present as part of Fe_3O_4; however, the exact oxygen stoichiometry cannot be determined with EDS as it is not quantitatively accurate for lighter elements. Oxygen, however, was determined to be present wherever Fe was detected. Figure 6.4e is an example of a summed EDS spectra showing the characteristic peaks of Fe, C, O and Pt. The latter results from the thin surface coating on the samples, which was added to avoid charging during this measurement.

As the solvent-processing method involves dispersing the Fe_3O_4 in a liquid phase, it is possible that the vertical uniformity of the composites could be affected by gravity or buoyancy in the solution. Samples were cross-sectioned by cutting with a knife, and the resulting concentration of the Fe was assessed with EDS mapping (shown in Figure 6.5) to determine the homogeneity of the Fe_3O_4 through the thickness of the Fe_3O_4: PU composites. Clearly, Fe is present throughout the Fe_3O_4: PU composites and is relatively uniform, although there is some subtle evidence of surface-enrichment layers at both interfaces.

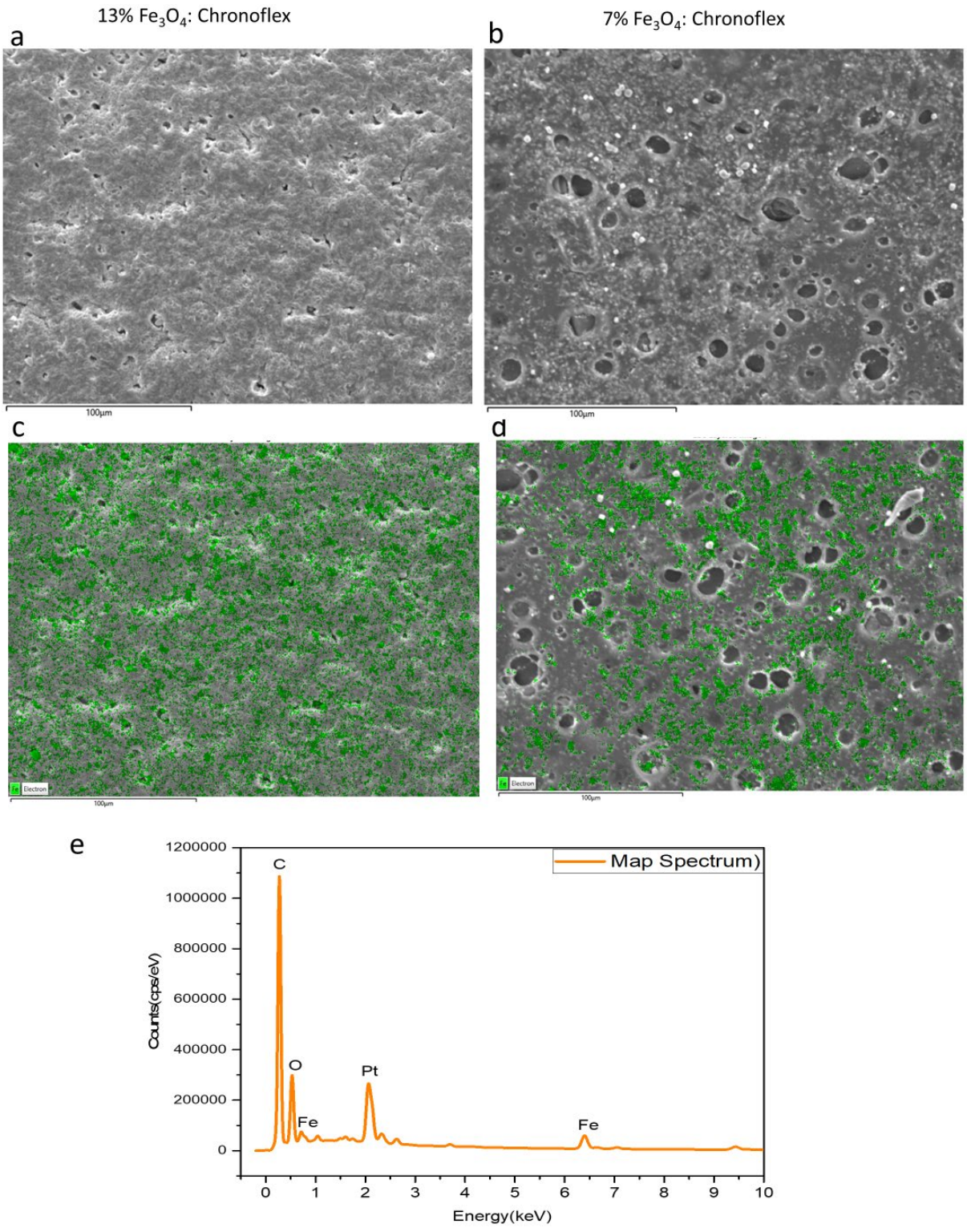

Figure 6.4: Plane-view low magnification SEM images and EDS of the composites. SEM image of (a) 13 wt.% Fe_3O_4-PU, (b) 7 wt.% Fe_3O_4-PU composites, where (c) and (d) show the iron

elemental distribution superimposed on corresponding SEM images. (e) is the energy dispersive spectrum of the nanocomposites.

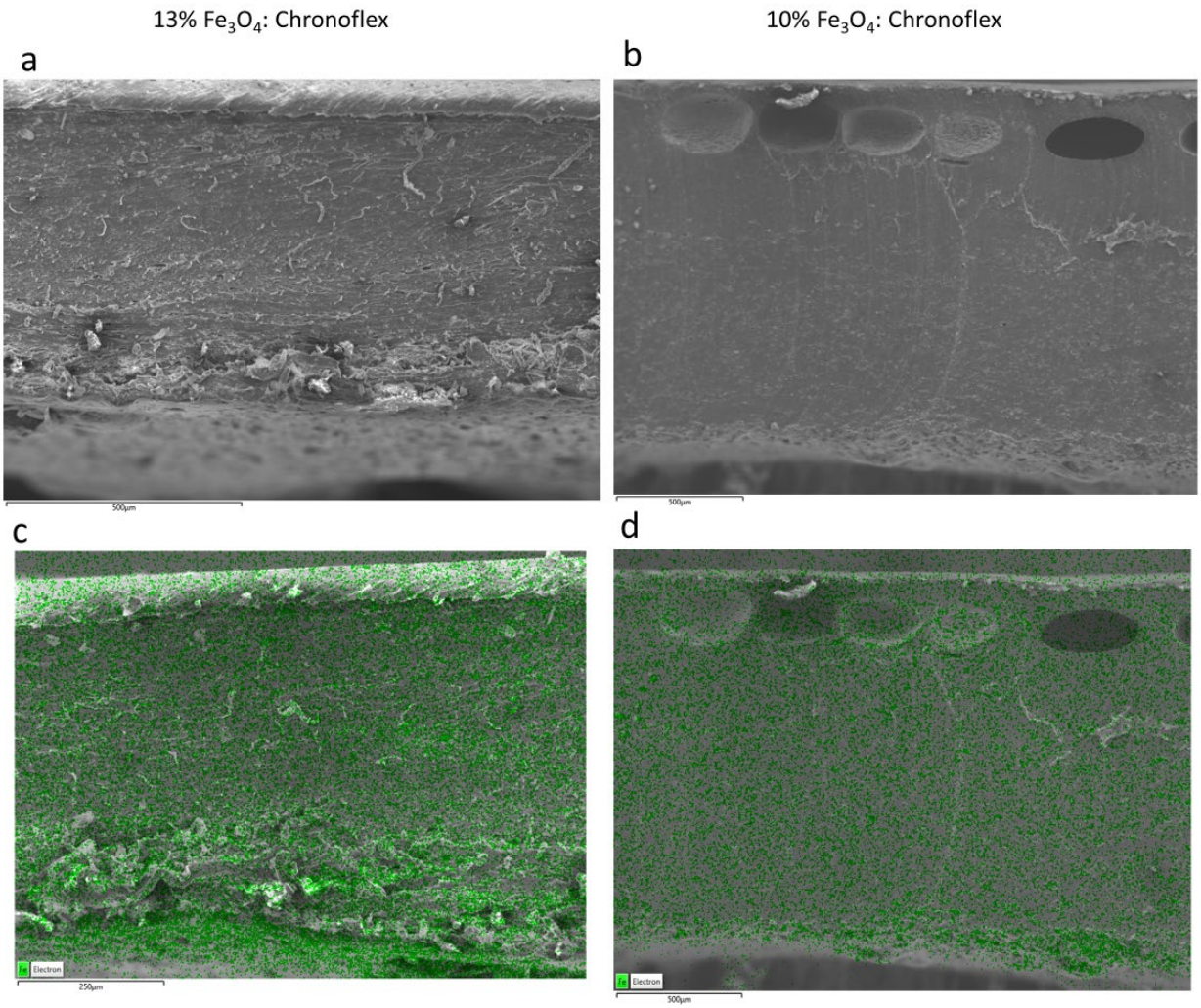

Figure 6.5: Cross-sectional SEM images and iron elemental distribution map of the Fe_3O_4-PU composites. (a) and (b) are cross-sectional SEM images of 13 wt.% Fe_3O_4-PU and 10 wt.% Fe_3O_4-PU, respectively. (c) and (d) show the iron distribution on a cross-sectional surface of 13 wt.% Fe_3O_4-PU, and 10% Fe_3O_4-PU, respectively.

Targeted heating requires polymers that are stable at higher temperatures. Thermogravimetric analysis (TGA) was performed to assess the thermal stability of the Fe_3O_4: PU composites and provide a measure of the experimental Fe_3O_4 weight percentages in the as-made Fe_3O_4: PU composites. Figure 6.6 shows the results of the TGA analysis. There is no mass loss of the polyurethane until ~200 ºC, whereupon there is a two-step mass loss as the material undergoes pyrolysis. The remaining mass after this point is a measure of the Fe_3O_4, which is stable to high temperatures. Table 6.1 presents the weight percent of Fe_3O_4 in the samples determined via TGA, magnetic saturation, and via a calculation made using the masses of the starting materials. The weight percentages for each composition determined experimentally are lower than the starting ratios would predict. This is attributed to a small loss of some of the Fe_3O_4 nanopowder (which sticks to the glassware) during the synthesis and also the hygroscopic nature of the PU, which absorbs a small amount of water when in ambient conditions.

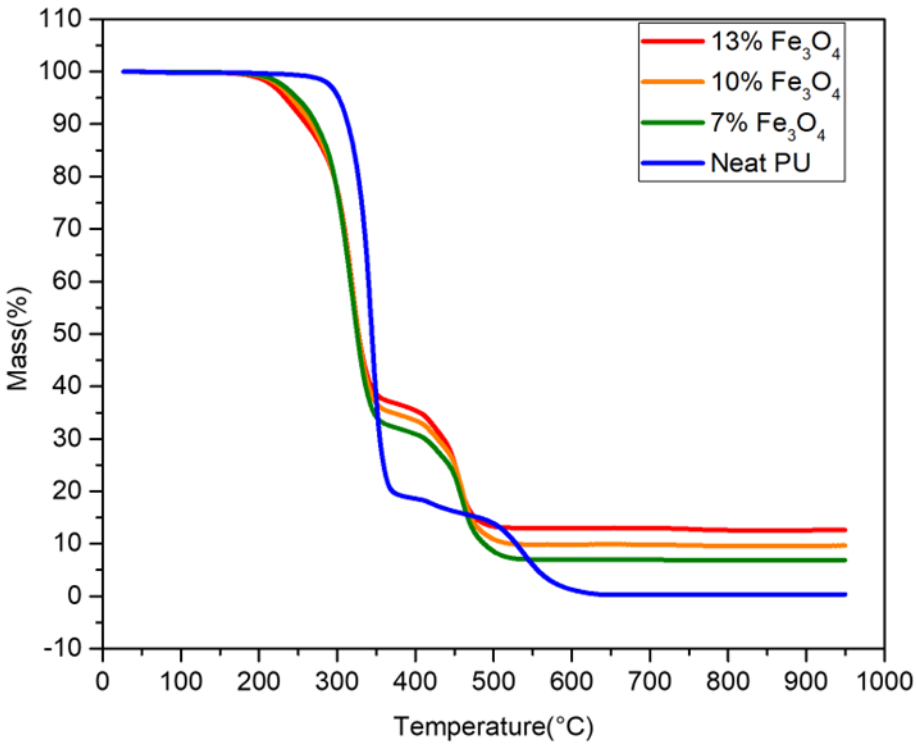

Figure 6.6.Thermal gravimetric analysis (TGA) of composites with different wt.% of Fe_3O_4. Red indicates 13 wt.% Fe_3O_4-PU composite, the orange for 10% Fe_30_4-PU, the olive for 7 wt.% Fe_3O_4-PU, blue indicates the results for the pure polyurethane. The TGA data shows the weight loss percentage with temperature.

Table 6.1. Theoretically calculated and experimentally measured wt.% of Fe_3O_4 in the samples during the synthesis and characterization process.

Sample	Theoretical wt.%	TGA wt.%	Saturation magnetization wt.%	Composition label in Figures
1. 7% Fe_3O_4 : Chronoflecx	9.05	6.9	7	"7%"
2. 10% Fe_3O_4: Chronoflex	13.1	9.9	9.4	"10%"
3. 13% Fe_3O_4 : Chronoflex	16.6	12.6	13.2	"13%"

Laser flash data analysis has been done to compare several methods to find the best fitting models to avoid experimental errors during measurements. Figures 6.7 and 6.8 show that the dedicated combined model was capable of fitting the data to a high level of accuracy, whereas the adiabatic and finite pulse methods show clear discrepancies of around (7.6% less). Figures 6.7 and 6.8 are the 13% Fe_3O_4-PU composite data at room temperature. All the data analysis has been done using baseline slope fitting with 25 filter points to obtain accurate fitting and thermal diffusivity results.

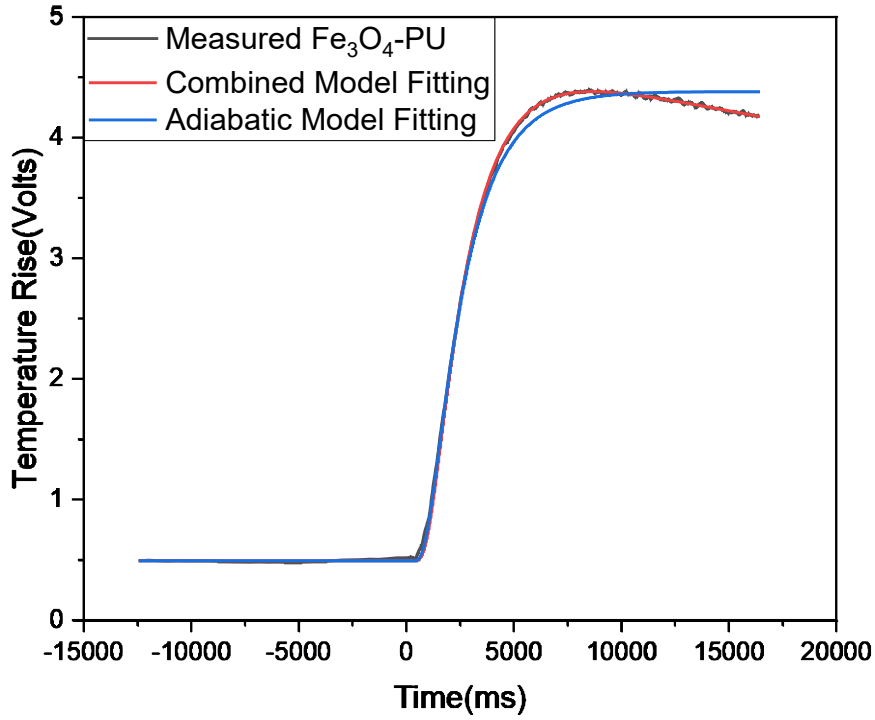

Figure 6.7: 13% Fe_3O_4-PU LFA data fitting comparison at room temperature between the adiabatic and combined model.

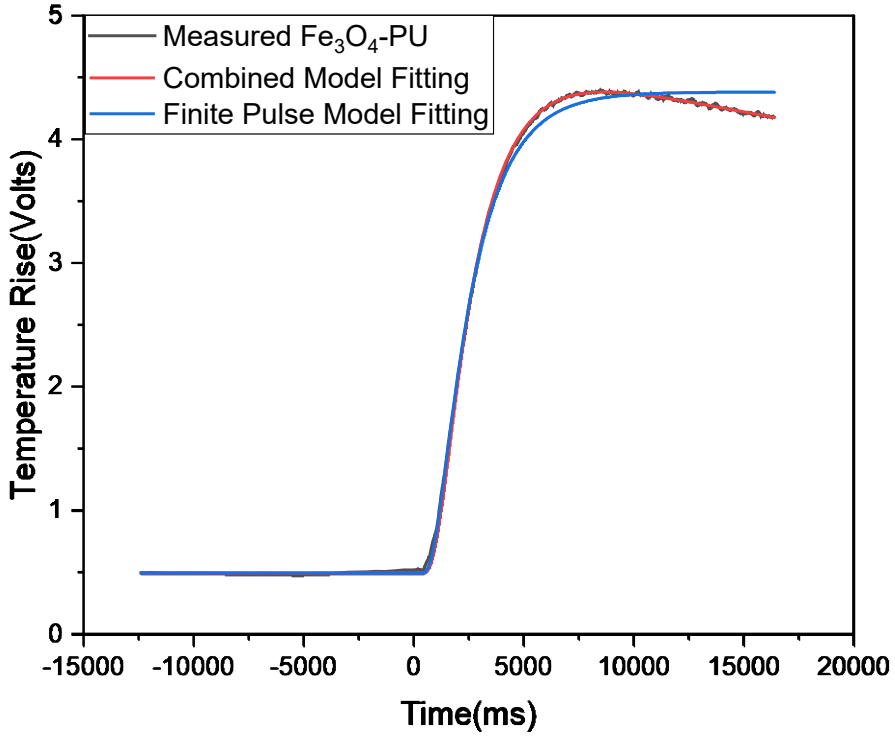

Figure 6.8: 13% Fe_3O_4-PU LFA data fitting comparison at room temperature between the finite pulse and combined model.

Laser flash analysis techniques were used to conduct thermal diffusivity on neat PU and Fe_3O_4-PU samples using Linseis LFA 1000. All the measurements were performed under vacuum conditions, and the experiments were done at room temperature. The nanocomposites showed a promising trend in thermal conductivity compared to neat polyurethane. Compared to neat polyurethane (0.094 $W.m^{-1}.K^{-1}$), the thermal conductivity was 41.5% in 7 wt.% Fe_3O_4-PU (0.133 $W.m^{-1}.K^{-1}$), 51% in 10 wt.% of Fe_3O_4-PU (0.142 $W.m^{-1}.K^{-1}$), and 178% in 13 wt.% Fe_3O_4-PU composites (0.262 $W.m^{-1}.K^{-1}$). Figure 6.9 illustrates the trend of enhancing the composites' thermal conductivity, and table 6.2 provides the actual thermal conductivity value.

Table 6.2: Thermal conductivity calculation of neat PU and Fe_3O_4-PU composites.

Measurements / Sample	Density (kg/m^3)	Heat Capacity (J/kg.k)	Thermal diffusivity (m^2/s)	Thermal conductivity ($W.m^{-1}.K^{-1}$)	The error of thermal conductivity	Controlled % of thermal conductivity
Neat PU	932.79	983	1.02E-07	0.0935	8.94E-7	-
7% Fe_3O_4-PU	1141.99	1002.42	1.16E-07	0.1328	5.18E-7	41
10% Fe_3O_4-PU	976.26	1100.02	1.32E-07	0.1417	1.10E-6	51
13% Fe_3O_4-PU	1071.96	1799.39	1.36E-07	0.2623	1.35E-6	178

Table 6.2 shows that the density of 10% Fe_3O_4-PU dropped by 14% compared with 7% Fe_3O_4-PU, directly impacting the final conductivity of the 10% Fe_3O_4-PU composite. Due to the lower density, the final thermal conductivity of 10% Fe_3O_4-PU is lower than expected, deviating slightly from the trends for than 7% and 13% Fe_3O_4-PU composites' results (Figure: 6.9). The low density

in 10% Fe_3O_4-PU is attributed to the presence of additional pores, which are also responsible for modifying the heat transport.

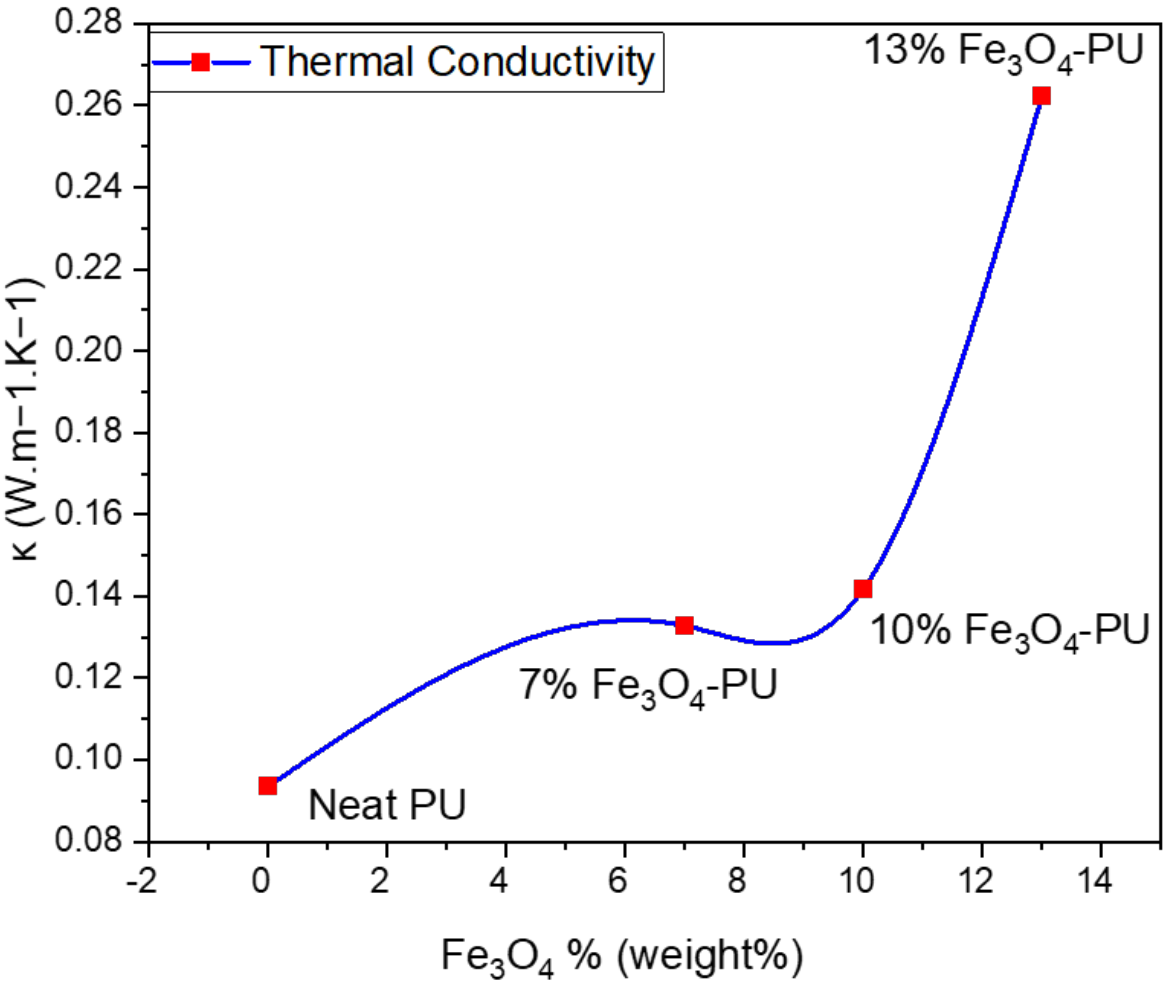

Figure 6.9: Summary of the thermal conductivity of neat PU, 7wt%, 10wt%, and 13wt % Fe_3O_4-PU composites.

Vibrating sample magnetometry was conducted to determine the magnetic properties of the Fe_3O_4: PU composites. All samples containing Fe_3O_4 showed room-temperature attraction and could be displaced using a permanent magnet, as illustrated (video link). Figure 6.10 shows the magnetic hysteresis loops at 300 K for several Fe_3O_4: PU composites, indicating a small coercive field of ~ 50 Oe at room temperature for a 3 Oe/s sweep rate. The coercive field is known to be one of the

important parameters for AC heating applications, as magnetic induction losses require irreversible losses during the switching of the magnet, where the heat from magnetization losses is proportional to the area within the hysteresis loop. So the presence of a small coercive field at room temperature is a prerequisite for inductive heating. In practice, the coercive field is frequency-dependent, such that it is expected to be enhanced at higher frequencies.

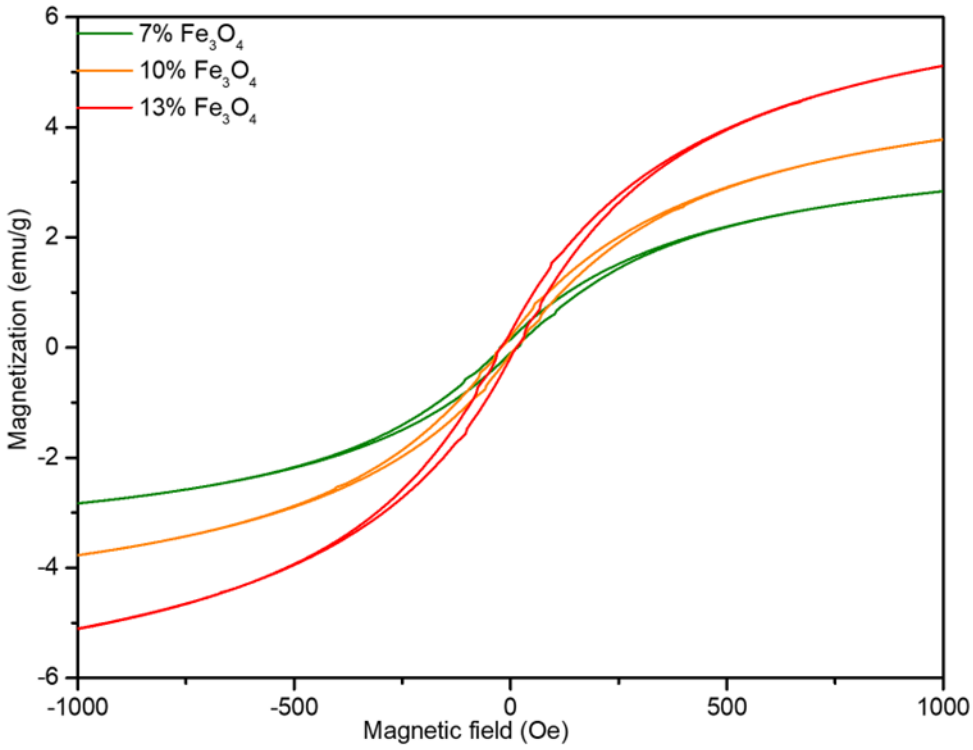

Figure 6.10: Room temperature magnetic hysteresis loops of nanocomposites with 7-13 wt. % Fe_3O_4 loading.

The data in Figure 6.10 provides a lower limit on the potential heat dissipated by the Fe_3O_4 nanoparticles during cycling near room temperature. The maximum (saturation) magnetization of the pure Fe_3O_4 nanopowder is ~ 70 emu/g, whereas, for the 7% Fe_3O_4: PU composite, it is 5 emu/g. This simply shows that the PU itself is non-magnetic, and magnetism, therefore, scales with the percentage of Fe_3O_4 in the composite. Indeed, the saturation magnetization can then be used as an

independent measure of the Fe_3O_4 weight percent, and the values are consistent with those presented in the TGA, as shown in Table 6.1. To investigate the temperature dependency of the hysteresis, Figure 6.11 shows several loops at different temperatures – both for the Fe_3O_4 nanopowder and the 7% Fe_3O_4: PU composite. Above 1 T, the magnetization plateaus in both datasets and the magnet is effectively saturated with its peak value at low temperature (5 K).

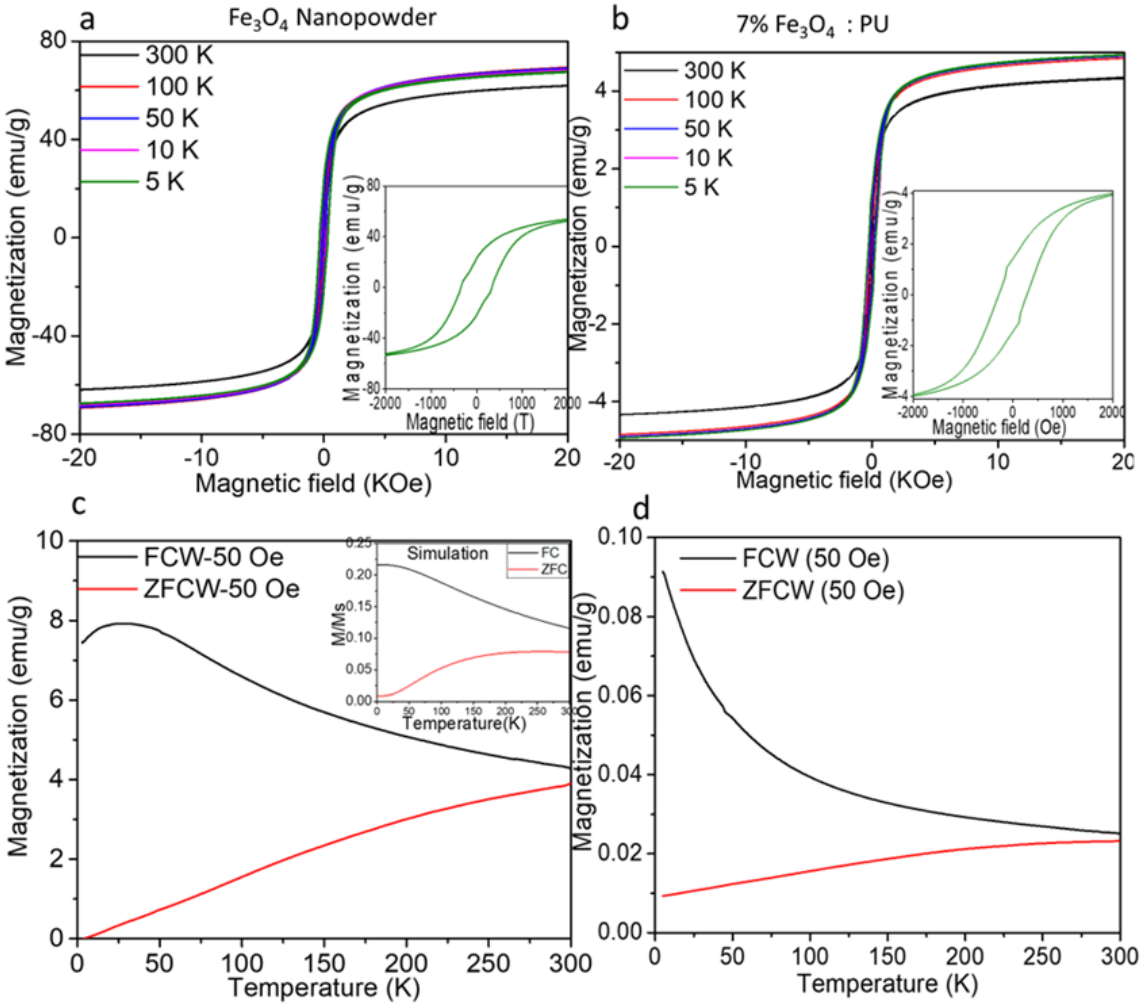

Figure 6.11: Magnetization versus magnetic field of the composites at 5-300 K for (a) pure Fe_3O_4 nanopowder and (b) 7 wt.% Fe_3O_4 loading of composite. 7 wt.% Fe_3O_4 loading of composite. (c) and (d) are the corresponding field cooled and zero field cooled curves of the pure nanopowder and 7 wt.% Fe_3O_4 composite. (c) The inset is a numerical simulation of magnetization.

To detect whether heating could be achieved in the Fe_3O_4:PU composites, a known mass of the Fe_3O_4:PU composite was inserted in the sample vial with 15 mL of distilled water and exposed to a weak, 85 kHz AC magnetic field. The temperature of the water, and hence the sample, was measured at the top of the vial to minimise magnetic field interference on the thermocouple. Experiments were performed for each Fe_3O_4: PU composite and for the Fe_3O_4 and PU starting materials; these experiments' temperature vs. time characteristics are shown in Figure 6.12. Peak temperatures of 45-50 ºC were achieved using the pure Fe_3O_4 nanopowder and for the 13% Fe_3O_4: PU composite after heating for approximately 18 minutes. While these temperatures are low compared to the melting temperature of PU, they are similar to biologically-relevant temperatures such as those involved in existing hyperthermia treatment schemes.

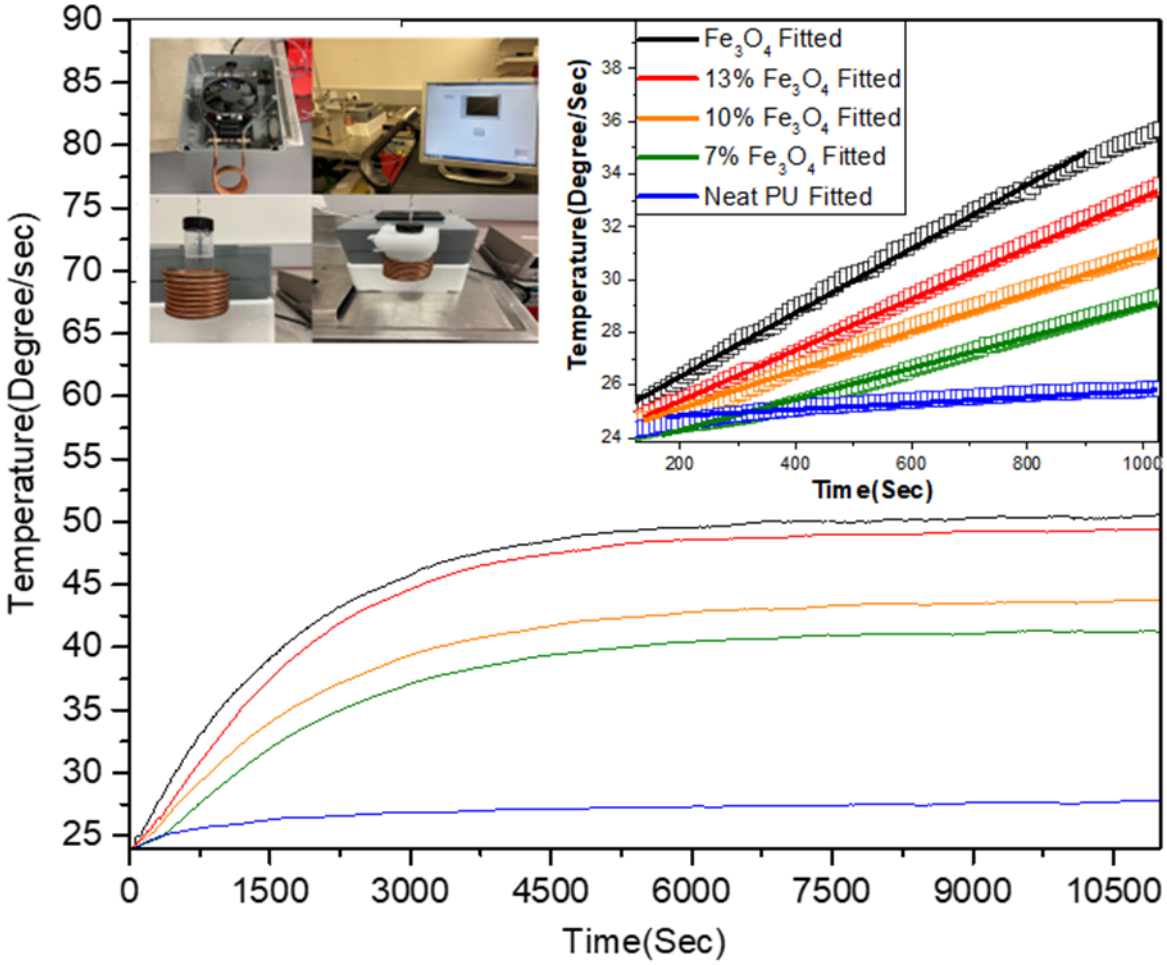

Figure 6.12: Temperature increase with respect to time in the Fe_3O_4 nanopowder, pure PU and PU composites with 7-13 wt.% Fe_3O_4 in an applied AC magnetic field. Inset figure shows the early-time rate of temperature increase for pure Fe_3O_4 nanopowder, neat PU and PU composites with 7-13 wt.% Fe_3O_4. The inset photograph shows the apparatus setup.

For example, hyperthermia generally targets a temperature range between 40-44 ºC to destroy cancerous cells. The maximum temperatures for each experiment configuration are reported in Table 6.3. Importantly, the maximum temperature attainable depends on many factors, not simply the efficiency of the samples themselves but also the ambient heat loss, amount of water, mass of the samples, and the amplitude of the driving magnetic field. From the initial temperature rise

(slope), it is possible to calculate the specific absorption rate (SAR) of the Fe_3O_4 nanoparticles using the formula:

$$SAR_{exp} = C\frac{\Delta T}{\Delta t}\frac{1}{m_{Fe}} \qquad 6.1$$

Note that the SAR was expressed in terms of the mass of m_{Fe} to allow comparison with past work on pure Fe_3O_4 powders. We use C=4.2 $kJ.kg^{-1}.K^{-1}$ for the heat capacity, and the values are reported in Table 6.3.

Table 6.3. Sample specific absorption rate (SAR) calculation.

Sample	Mass of Fe (g)	ΔT/Δt (°C/s)	Max temperature (°C)	SAR ($J.s^{-1}.g_{Fe}^{-1}$)
1. Pure Fe_3O_4 nanopowder	0.366	0.01213	50.50	0.1392
2. 13% Fe_3O_4	0.476	0.00966	49.03	0.0852
3. 10% Fe_3O_4	0.366	0.00727	43.66	0.0834
4. 7% Fe_3O_4	0.256	0.00588	41.44	0.0965
5. Neat PU	0	0.00117	27.66	N/A

6.4.Discussion

The solvent-based processing method used in this work is a simple and inexpensive way to produce relatively uniform plastic Fe_3O_4: PU composites. The resulting homogeneity is determined by the interaction of the components when in the solvent, but the as-made Fe_3O_4: PU composites presented here are relatively homogenous, as shown by the wide-area SEM mapping. The magnetic nature of bare Fe_3O_4 particles is known to lead to self-assembly into chains and other structures, such that ideal homogeneity is always challenging to achieve. For this reason, silica-coated Fe_3O_4 or other functional groups could be desirable to control the particle packing and interparticle distances in these composites. Nevertheless, the work here on inexpensive uncoated Fe_3O_4 nanoparticles is promising, as the microscale homogeneity is certainly acceptable for heating applications targeting features sizes at 0.1 mm^3 resolutions. Importantly the materials were stable to high temperatures and could enable targeted heating even in a small AC magnetic field.

The analytical analysis of thermal conductivity shows that the addition of Fe_3O_4 has a significant effect. The laser flash analysis technique shows that κ is enhanced for higher Fe_3O_4 volume fractions. The detailed magnetometry study shows that the main magnetic properties of the Fe_3O_4 nanopowder are retained in the composite. One detail that impacts nanomagnetic performance is particles' density and packing fraction, as dipolar interactions can modify the collective behaviour. As the composites used here contained relatively low weight (and volume) percentages of Fe_3O_4, it is expected that the spacing between the particles would be larger than in the pure powder, on the proviso that the particles are well-dispersed. This would manifest in a change in their susceptibility under an applied field. The field-cooled data in Figure 6.11 does indicate some differences between the pure powder and dispersed Fe_3O_4 nanopowder in the Fe_3O_4: PU

composites, suggesting the magnetic interactions are weaker in the composite giving a simpler Curie-Weis like dependency.

The specific absorption rates have been calculated in Table 6.3 for acquiring compatible outcomes with those reported for state-of-the-art pure Fe_3O_4 nanopowders [138, 139]. However, these values depend critically on the magnitude and frequency of the AC magnetic field. Therefore, there is scope to significantly improve the SAR of Fe_3O_4:PU composites in the future, if needed, by optimizing the frequency and size of the alternating driving field, although this may not be necessary and would depend on the specific application. The significant control in thermal conductivity also opens several doors to producing highly efficient, flexible future thermoelectric devices. Further studies are needed to improve electrical conductivity and get a considerable Seebeck effect from the composites.

6.5.Conclusion

The significant advantage of polymer-based materials is the ability to rapidly produce geometries via cast moulding (as in this work) or additive manufacturing (3D printing). The polyurethane used in this work, Chronoflex C®, is already being explored for use in implants. It has the advantage of being biocompatible, 3D printable and robust. Our work thus indicates strong future prospects for developing 3D printable materials based on Fe_3O_4: PU composites. To enable 3D printing, future work is necessary to optimize the melting points, mechanical properties, and electrical conductivity of these composites.

This chapter also demonstrated remote heating via induction. In general, magnetic heating is more gentle than optical heating (e.g. heating of Au by EM radiation); however, magnetic heating requires a high local concentration of the nanoparticles. Theoretical calculations showed that

heating biomedical implants embedded with nanoparticles are a viable option [140]. Whereas some previous work has shown the feasibility of destroying pathogens in rats using AC magnetic heating of metallic implants via induction, there is far less knowledge surrounding magnetic heating in polymer-based implants. The types of materials developed in this work may potentially allow these studies in the future.

The ability to target particles for remote heating makes nanocomposite plastics attractive in a variety of settings (drug delivery, chemical reactions, thermal actuation and chemical separation). Compared to existing magnetic plastics based on metallic Fe, Fe_3O_4 has some advantages. Firstly, it is more resistant to oxidization, and so the magnetic properties are expected to last for long periods. Secondly, it is biocompatible. The plastics also present room temperature magnetic motion, offering actuators and field guidance applications.

Chapter 7: Conclusion

This research project investigated different materials' thermal properties and conductivity, focusing on chemical methods to achieve heat management. These methods included nano-doping to tune thermal conductivity. The work explored Cu_2Se, Bi_2Te_3, polyurethane and Fe_3O_4 materials produced using both melt route processing and solvent-based processing methods. The experiments provide useful insights into methods to obtain desirable materials for specific applications that require particular levels of thermal conductivity. In particular, the work revealed a way to control thermal conductivity in polymer-based composites (Fe_3O_4-PU) and a method to significantly reduce the thermal conductivity in thermoelectric Na_2CO_3 doped Cu_2Se and Bi_2Te_3-PU composites.

The major findings from this work are listed below:

In Chapter 4, the main finding is the considerable reduction of the thermal conductivity by up to 34% in 1.4 wt.% Na_2CO_3 doped Cu_2Se compared to raw Cu_2Se at 554 K. Additionally, it followed an inverse trend between the reacted amount of Na_2CO_3 in Cu_2Se and thermal conductivity. The addition of Na_2CO_3 (0.09, 0.18, 0.35, 0.70, and 1.40 wt.%) in Cu_2Se decreased the thermal conductivity within the temperature range from 355 K to 981 K. As Cu_2Se is less expensive and less toxic than lead-based thermoelectric materials, Cu_2Se: Na_2CO_3 materials could become an excellent prospective candidate for energy extraction in future thermoelectric modules.

In Chapter 5, the main result was the investigation of polyurethane as an appropriate matrix for Bi_2Te_3 for developing flexible thermoelectric materials. A novel method was developed to produce Bi_2Te_3 nanoflakes using a liquid-phase exfoliation method to get the desired quasi-2D Bi_2Te_3 nanomaterials and then embed them into polyurethane using a solvent-based processing method.

One attractive finding is that the Bi_2Te_3-PU composites had a thermal conductivity reduced by a maximum of 94% in 2 v% Bi_2Te_3 at room temperature, 93% in 4 v.% Bi_2Te_3-PU and 87% reduction in 7 v% Bi_2Te_3-PU. These experimental results also show that it is possible to predict and engineer thermal conductivity in these composites at a certain level by using the Law of Mixtures.

In Chapter 6, novel magnetic: thermal composites were fabricated by a solvent-based processing method. Significant enhancement of the thermal conductivity up to 178% in 13% Fe_3O_4-PU compared to neat polyurethane was observed at room temperature, making the composites a prospective candidate for 3D printable wearable devices. Moreover, the magnetic attraction was also observed with a saturation magnetization of up to 5 emu/g and a low coercive field ($H_c < 50$ Oe). A promising form of remote heating of the plastic was demonstrated for samples submerged in a water environment. The temperature could be increased to 45° C within 18 minutes. This indicates that it is possible to custom-design plastic magnetic implants that can be heated remotely to achieve a variety of functionalities, including as a component in magnetic-field-to-energy conversion, inductive heating technology and hyperthermia.

7.1.Future work

Investigation of the electrical and thermal transport parameters has importance for determining whether a given thermoelectric system is promising or not. This research project mainly focused on controlling thermal conductivity to produce future thermoelectric generators. The research has developed low thermal conductivity composites because low thermal conductivity is the prime

requirement for producing efficient thermoelectric materials. I propose the following strategies for future work based on this research project.

(1) The doping approach is a promising way to modify thermoelectric parameters in bulk materials. In this study, Na_2CO_3 was chemically doped into the Cu_2Se matrix, significantly reducing thermal conductivity. In future work, it might be possible to obtain improved thermoelectric performance by using additional dopants (such as Al, Pt) that substitute into the Cu sites of this compound.

(2) Combining a polyurethane matrix with Bi_2Te_3 resulted in a considerably reduced thermal conductivity due to the effect of the nanoinclusions. Future work is still needed, however, to produce an electrical signal from the flexible composites. I hope to implement novel designs of microstructures using nano-compositing methods to improve thermoelectric performance in future research work. Inclusion of magnetic particles may be very effective in transforming polyurethane/Bi_2Te_3 nanocomposites into a functional or 'smart' thermoelectric polymer that can also be heated remotely.

(3) The use of Fe_3O_4 in polyurethane for controlling thermal conductivity was in preparation for creating future wearable devices that can be remotely heated. Due to the medical approval of Fe_3O_4 and polyurethane, it may be possible to produce skin-contacting wearable devices, possibly in combination with TE materials. In future work, introducing another phase (such as a thermoelectric phase) could be a viable way to obtain considerable multifunctional performance from these composites where solvent base processing methods have been proven

to produce a uniform distribution of nanoparticles. For producing flexible composites, this process is also eco-friendly and inexpensive.

(4) High-performance wearable devices are an exciting direction for future work. I will explore new techniques to produce hybrid composites that can make a thin film and flexible composites. This may open a new way to harvest energy using wearable smart devices and clothing.

References

[1] M. Belmonte, "Advanced ceramic materials for high temperature applications," *Advanced engineering materials,* vol. 8, no. 8, pp. 693-703, 2006.

[2] S. M. K. Nazrul-Islam *et al.*, "Beneficial Effect of Na2CO3 Additions on the Thermoelectric Performance of Melt-Route Cu2Se," *Advanced Electronic Materials,* p. 2100802, 2021.

[3] K. Kawano, K. Kurosaki, T. Sekimoto, H. Muta, and S. Yamanaka, "Effect of Sn doping on the thermoelectric properties of ErNiSb-based p-type half-Heusler compound," *Applied Physics Letters,* vol. 91, no. 6, p. 062115, 2007.

[4] N. Haldolaarachchige *et al.*, "Effect of chemical doping on the thermoelectric properties of FeGa3," *Journal of Applied Physics,* vol. 109, no. 10, p. 103712, 2011.

[5] S. Komarneni, "Nanocomposites," *Journal of Materials Chemistry,* vol. 2, no. 12, pp. 1219-1230, 1992.

[6] D. Hull, "An Introduction to Composite Materials," ed, 1998.

[7] C.-L. Huang, X. Qian, and R.-G. Yang, "Influence of nanoparticle size distribution on the thermal conductivity of particulate nanocomposites," *EPL (Europhysics Letters),* vol. 117, no. 2, p. 24001, 2017.

[8] X. Yang *et al.*, "A review on thermally conductive polymeric composites: classification, measurement, model and equations, mechanism and fabrication methods," *Advanced composites and hybrid materials,* vol. 1, no. 2, pp. 207-230, 2018.

[9] C. Kittel, P. McEuen, and P. McEuen, *Introduction to solid state physics*. Wiley New York, 1996.

[10] G. Chen, *Nanoscale energy transport and conversion: a parallel treatment of electrons, molecules, phonons, and photons*. Oxford university press, 2005.

[11] R. H. Dalitz and R. E. Peierls, *Selected Scientific Papers of Sir Rudolf Peierls, with Commentary by the Author*. World Scientific, 1997.

[12] R. Peierls, "Quantum Theory of Solids–Oxford UP," *London, England,* p. 108, 1955.

[13] A. Einstein, *Ann. Phys.,* vol. 340, p. 898, 1911.

[14] G. A. Slack, "The thermal conductivity of nonmetallic crystals," *Solid state physics,* vol. 34, pp. 1-71, 1979.

[15] D. G. Cahill, S. K. Watson, and R. O. Pohl, "Lower limit to the thermal conductivity of disordered crystals," *Physical Review B,* vol. 46, no. 10, p. 6131, 1992.

[16] R. Zeller and R. Pohl, "Thermal conductivity and specific heat of noncrystalline solids," *Physical Review B,* vol. 4, no. 6, p. 2029, 1971.

[17] N. Yüksel, "The review of some commonly used methods and techniques to measure the thermal conductivity of insulation materials," in *Insulation materials in context of sustainability*: IntechOpen, 2016.

[18] H. Czichos, T. Saito, and L. Smith, *Springer handbook of materials measurement methods*. Springer, 2006.

[19] S. A. Al-Ajlan, "Measurements of thermal properties of insulation materials by using transient plane source technique," *Applied thermal engineering,* vol. 26, no. 17-18, pp. 2184-2191, 2006.

[20] Z. Chen, X. Zhang, and Y. Pei, "Manipulation of phonon transport in thermoelectrics," *Advanced Materials,* vol. 30, no. 17, p. 1705617, 2018.

[21] A. A. Balandin, "Thermal properties of graphene and nanostructured carbon materials," *Nature materials,* vol. 10, no. 8, pp. 569-581, 2011.

[22] J. F. Archilla, S. M. Coelho, F. D. Auret, C. Nyamhere, V. I. Dubinko, and V. Hizhnyakov, "Experimental observation of intrinsic localized modes in germanium," in *Quodons in Mica*: Springer, 2015, pp. 343-362.

[23] E. Lehockey, A. Brennenstuhl, G. Palumbo, and P. Lin, "On the relationship between grain boundary character distribution and intergranular corrosion," *Scripta materialia,* vol. 36, no. 10, 1997.

[24] D. Li, Y. Wu, P. Kim, L. Shi, P. Yang, and A. Majumdar, "Thermal conductivity of individual silicon nanowires," *Applied Physics Letters,* vol. 83, no. 14, pp. 2934-2936, 2003.

[25] A. Balandin and K. L. Wang, "Significant decrease of the lattice thermal conductivity due to phonon confinement in a free-standing semiconductor quantum well," *Physical Review B,* vol. 58, no. 3, p. 1544, 1998.

[26] J.-F. Li, W.-S. Liu, L.-D. Zhao, and M. Zhou, "High-performance nanostructured thermoelectric materials," *NPG Asia Materials,* vol. 2, no. 4, pp. 152-158, 2010.

[27] M. Alger, *Polymer science dictionary*. Springer Science & Business Media, 1996.

[28] D. R. Askeland, P. P. Fulay, and W. J. Wright, "The Science and Engineering of Materials,—6th ed., Cengage Learning," 2010.

[29] J. C. Maxwell, *A treatise on electricity and magnetism*. Clarendon press, 1873.

[30] J. Xu, B. Gao, and F. Kang, "A reconstruction of Maxwell model for effective thermal conductivity of composite materials," *Applied Thermal Engineering,* vol. 102, pp. 972-979, 2016.

[31] R. Bird, W. Stewart, and E. Lightfoot, "Other mechanisms for mass transport," *Transport Phenomena, John Wiley & Sons, Inc,* 2007.

[32] L. Rayleigh, "LVI. On the influence of obstacles arranged in rectangular order upon the properties of a medium," *The London, Edinburgh, and Dublin Philosophical Magazine and Journal of Science,* vol. 34, no. 211, pp. 481-502, 1892.

[33] R. Pumps Bird, W. Stewart, and E. Lightfoot, "Transport Phenomena, Revised," ed: John Wiley & Sons, New York, 2007.

[34] K. Pietrak and T. S. Wisniewski, "A review of models for effective thermal conductivity of composite materials," *Journal of Power Technologies,* vol. 95, no. 1, p. 14, 2015.

[35] B. R. Powell Jr, G. Youngblood, D. Hasselman, and L. D. Bentsen, "Effect of Thermal Expansion Mismatch on the Thermal Diffusivity of Glass-Ni Composites," *Journal of the American Ceramic Society,* vol. 63, no. 9-10, pp. 581-586, 1980.

[36] D. Hasselman and L. F. Johnson, "Effective thermal conductivity of composites with interfacial thermal barrier resistance," *Journal of composite materials,* vol. 21, no. 6, pp. 508-515, 1987.

[37] E. T. Swartz and R. O. Pohl, "Thermal boundary resistance," *Reviews of modern physics,* vol. 61, no. 3, p. 605, 1989.

[38] V. D. Bruggeman, "Berechnung verschiedener physikalischer Konstanten von heterogenen Substanzen. I. Dielektrizitätskonstanten und Leitfähigkeiten der Mischkörper aus isotropen Substanzen," *Annalen der physik,* vol. 416, no. 7, pp. 636-664, 1935.

[39] R. Landauer, "The electrical resistance of binary metallic mixtures," *Journal of Applied Physics,* vol. 23, no. 7, pp. 779-784, 1952.

[40] A. Every, Y. Tzou, D. Hasselman, and R. Raj, "The effect of particle size on the thermal conductivity of ZnS/diamond composites," *Acta metallurgica et materialia,* vol. 40, no. 1, pp. 123-129, 1992.

[41] Y. Benveniste, "Effective thermal conductivity of composites with a thermal contact resistance between the constituents: Nondilute case," *Journal of applied physics,* vol. 61, no. 8, pp. 2840-2843, 1987.

[42] A. Devpura, P. E. Phelan, and R. S. Prasher, "Percolation theory applied to the analysis of thermal interface materials in flip-chip technology," in *ITHERM 2000. The Seventh Intersociety Conference on Thermal and Thermomechanical Phenomena in Electronic Systems (Cat. No. 00CH37069)*, 2000, vol. 1, pp. 21-28: IEEE.

[43] X.-Q. Fang, "Non-steady effective thermal conductivity of matrix composite materials with high volume concentration of particles," *Computational materials science,* vol. 44, no. 2, pp. 481-488, 2008.

[44] X.-Q. Fang, J.-X. Liu, T. Zhang, and X.-H. Wang, "Scattering of thermal waves and unsteady effective thermal conductivity of particular composites with functionally graded interface," *Journal of composite materials,* vol. 43, no. 21, pp. 2351-2369, 2009.

[45] N. N. Greenwood and A. Earnshaw, *Chemistry of the Elements*. Elsevier, 2012.

[46] M. Francombe, "Structure-cell data and expansion coefficients of bismuth telluride," *British Journal of Applied Physics,* vol. 9, no. 10, p. 415, 1958.

[47] W. Huang, H. Da, and G. Liang, "Thermoelectric performance of mx2 (m= mo, w; x= s, se) monolayers," *Journal of Applied Physics,* vol. 113, no. 10, p. 104304, 2013.

[48] B. Huang, X. Yang, L. Liu, and P. Zhai, "Effects of Van der Waals bonding on the compressive mechanical behavior of bulk Bi 2 Te 3: A molecular dynamics study," *Journal of Electronic Materials,* vol. 44, no. 6, pp. 1668-1673, 2015.

[49] J. Ko, J.-Y. Kim, S.-M. Choi, Y. S. Lim, W.-S. Seo, and K. H. Lee, "Nanograined thermoelectric Bi 2 Te 2.7 Se 0.3 with ultralow phonon transport prepared from chemically exfoliated nanoplatelets," *Journal of Materials Chemistry A,* vol. 1, no. 41, pp. 12791-12796, 2013.

[50] R. Deng *et al.*, "High thermoelectric performance in Bi 0.46 Sb 1.54 Te 3 nanostructured with ZnTe," *Energy & Environmental Science,* vol. 11, no. 6, pp. 1520-1535, 2018.

[51] K.-C. Kim *et al.*, "Precision interface engineering of an atomic layer in bulk Bi2Te3 alloys for high thermoelectric performance," *ACS nano,* vol. 13, no. 6, pp. 7146-7154, 2019.

[52] P. Dharmaiah, K.-H. Lee, S. H. Song, H. S. Kim, and S.-J. Hong, "Enhanced thermoelectric performance of Bi0. 5Sb1. 5Te3 composites through potential barrier scattering at heterogeneous interfaces," *Materials Research Bulletin,* vol. 133, p. 111023, 2021.

[53] K. Ahmad and C. Wan, "Enhanced thermoelectric performance of Bi2Te3 through uniform dispersion of single wall carbon nanotubes," *Nanotechnology,* vol. 28, no. 41, p. 415402, 2017.

[54] S. Li *et al.*, "Graphene quantum dots embedded in Bi2Te3 nanosheets to enhance thermoelectric performance," *ACS applied materials & interfaces,* vol. 9, no. 4, pp. 3677-3685, 2017.

[55] S. Cao, Z.-Y. Huang, F.-Q. Zu, J. Xu, L. Yang, and Z.-G. Chen, "Enhanced thermoelectric properties of Ag-modified Bi0. 5Sb1. 5Te3 composites by a facile electroless plating method," *ACS applied materials & interfaces,* vol. 9, no. 42, pp. 36478-36482, 2017.

[56] B. Zhang, J. Sun, H. Katz, F. Fang, and R. Opila, "Promising thermoelectric properties of commercial PEDOT: PSS materials and their Bi2Te3 powder composites," *ACS applied materials & interfaces,* vol. 2, no. 11, pp. 3170-3178, 2010.

[57] X. Liu *et al.*, "Exploring Sodium Storage Mechanism of Topological Insulator Bi2Te3 Nanosheets Encapsulated in Conductive Polymer," *Energy Storage Materials,* 2021.

[58] K. Tyagi, B. Gahtori, S. Bathula, S. Auluck, and A. Dhar, "Band structure and transport studies of copper selenide: An efficient thermoelectric material," *Applied Physics Letters,* vol. 105, no. 17, p. 173905, 2014.

[59] S. M. Nazrul Islam, "Effectiveness of mill scale on the decomposition of dye ingredients for the treatment of textile effluent," 2013.

[60] S. M. K. N. Islam, A. Kurny, and F. Gulshan, "Degradation of commercial dyes using Mill scale by photo-fenton," *Environmental Processes,* vol. 2, no. 1, pp. 215-224, 2015.

[61] H. Chi *et al.*, "Low-temperature structural and transport anomalies in Cu 2 Se," *Physical Review B,* vol. 89, no. 19, p. 195209, 2014.

[62] H. Liu *et al.*, "Copper ion liquid-like thermoelectrics," *Nature materials,* vol. 11, no. 5, pp. 422-425, 2012.

[63] H. Liu *et al.*, "Copper ion liquid-like thermoelectrics," *Nat. Mater.,* 10.1038/nmat3273 vol. 11, no. 5, pp. 422-425, 05//print 2012.

[64] S. M. K. N. Islam *et al.*, "Copper Diffusion Rates and Hopping Pathways in Superionic Cu2Se," *Acta Materialia,* p. 117026, 2021.

[65] E. F. Hampl, "Thermoelectric composition," United States Patent 3,853,632, 1973.

[66] T. W. Day *et al.*, "High-temperature thermoelectric properties of $Cu_{1.97}Ag_{0.03}Se_{1+y}$," *Mater. Renew. Sustain. Energy,* vol. 3, p. 26, 2014.

[67] T. P. Bailey *et al.*, "Enhanced ZT and attempts to chemically stabilize Cu_2Se via Sn doping," *J. Mater. Chem. A,* vol. 4, p. 17225, 2016.

[68] A. Olvera *et al.*, "Partial indium solubility induces chemical stability and colossal thermoelectric figure-of-merit in Cu_2Se," *Energy & Environmental Science,* vol. 10, no. 7, pp. 1668-1676, 2017.

[69] P. Peng *et al.*, "Structure and thermoelectric performance of β-Cu_2Se doped with Fe, Ni, Mn, In, Zn or Sm," *Intermetallics* vol. 75, pp. 72-78, 2016.

[70] H. Liu *et al.*, "Ultrahigh thermoelectric performance by electron and phonon critical scattering in $Cu_2Se_{1-x}I_x$," *Adv. Mater.,* vol. 25, no. 45, pp. 6607-6612, 2013.

[71] S. M. K. N. Islam *et al.*, "Giant enhancement of the figure-of-merit over a broad temperature range in nano-boron incorporated Cu_2Se," *J. Mater. Chem. A,* vol. 6, pp. 18409-18416, 2018.

[72] S. D. Kang *et al.*, "Enhanced stability and thermoelectric figure-of-merit in copper selenide by lithium doping," *Materials Today Physics,* vol. 1, pp. 7-13, 2017.

[73] L. Zhao *et al.*, "Improvement of thermoelectric properties and their correlations with electron effective mass in $Cu_{1.98}S_xSe_{1-x}$," *Scientific Reports,* vol. 7, p. 40436, 2017.

[74] L. Yang, Z.-G. Chen, G. Han, M. Hong, L. Huang, and J. Zou, "Te-doped Cu_2Se nanoplates with a high average thermoelectric figure-of-merit," *Journal of Materials Chemistry A,* 10.1039/C6TA02998A vol. 4, no. 23, pp. 9213-9219, 2016.

[75] A. P. Sudha, J. Henry, K. Mohanraj, and G. Sivakumar, "Effect of Na doping on structural, optical, and electrical properties of Cu_2Se thin films prepared by chemical bath deposition method," *Appl. Phys. A,* vol. 124, p. 164, 2018.

[76] Z. Zhu, Y. Zhang, H. Song, and X. J. Li, "High thermoelectric performance and low thermal conductivity in $Cu_{2-x}Na_xSe$ bulk materials with micro-pores," *Appl. Phys. A,* vol. 125, p. 572, 2019.

[77] Y. Jin, M.-K. Han, S.-J. Kim, Y. Jin, M.-K. Han, and S.-J. Kim, "Na-doping effects on thermoelectric properties of $Cu_{2-x}Se$ nanoplates," *Appl. Sci.,* vol. 8, p. 12, 2018.

[78] M. Li *et al.*, "Ultra-high thermoelectric performance in graphene incorporated Cu2Se: Role of mismatching phonon modes," *Nano Energy,* vol. 53, pp. 993-1002, 2018.

[79] S. Hébert *et al.*, "Thermoelectric materials taking advantage of spin entropy: lessons from chalcogenides and oxides," *Science and Technology of Advanced Materials,* vol. 22, no. 1, pp. 583-596, 2021.

[80] J.-B. Vaney, S. A. Yamini, H. Takaki, K. Kobayashi, N. Kobayashi, and T. Mori, "Magnetism-mediated thermoelectric performance of the Cr-doped bismuth telluride tetradymite," *Materials Today Physics,* vol. 9, p. 100090, 2019.

[81] E. Kuchma, S. Kubrin, and A. Soldatov, "The local atomic structure of colloidal superparamagnetic iron oxide nanoparticles for theranostics in oncology," *Biomedicines,* vol. 6, no. 3, p. 78, 2018.

[82] L. S. Ganapathe, M. A. Mohamed, R. Mohamad Yunus, and D. D. Berhanuddin, "Magnetite (Fe3O4) nanoparticles in biomedical application: from synthesis to surface functionalisation," *Magnetochemistry,* vol. 6, no. 4, p. 68, 2020.

[83] R. Moreno *et al.*, "The role of faceting and elongation on the magnetic anisotropy of magnetite Fe 3 O 4 nanocrystals," *Scientific reports,* vol. 10, no. 1, pp. 1-14, 2020.

[84] H. Liu and C. Di Valentin, "Band gap in magnetite above Verwey temperature induced by symmetry breaking," *The Journal of Physical Chemistry C,* vol. 121, no. 46, pp. 25736-25742, 2017.

[85] B. T. Hogan, E. Kovalska, M. F. Craciun, and A. Baldycheva, "2D material liquid crystals for optoelectronics and photonics," *Journal of Materials Chemistry C,* vol. 5, no. 43, pp. 11185-11195, 2017.

[86] S. M. K. Nazrul Islam, "Study of Chalcogenide based Thermoelectric Materials for Waste Heat Recovery," 2018.

[87] A. Philipp, J. F. Eichinger, R. C. Aydin, A. Georgiadis, C. J. Cyron, and M. Retsch, "The accuracy of laser flash analysis explored by finite element method and numerical fitting," *Heat and Mass Transfer,* vol. 56, no. 3, pp. 811-823, 2020.

[88] D. Watt, "Theory of thermal diffusivity by pulse technique," *British Journal of Applied Physics,* vol. 17, no. 2, p. 231, 1966.

[89] L. Vozár and W. Hohenauer, "Flash method of measuring the thermal diffusivity. A review," *High temperatures-High pressures,* vol. 36, no. 3, pp. 253-264, 2004.

[90] L. Clark Iii and R. Taylor, "Radiation loss in the flash method for thermal diffusivity," *Journal of Applied Physics,* vol. 46, no. 2, pp. 714-719, 1975.

[91] T. Azumi and Y. Takahashi, "Novel finite pulse-width correction in flash thermal diffusivity measurement," *Review of scientific instruments,* vol. 52, no. 9, pp. 1411-1413, 1981.

[92] J. Cape and G. Lehman, "Temperature and finite pulse-time effects in the flash method for measuring thermal diffusivity," *Journal of applied physics,* vol. 34, no. 7, pp. 1909-1913, 1963.

[93] R. Heckman, "Finite pulse-time and heat-loss effects in pulse thermal diffusivity measurements," *Journal of Applied Physics,* vol. 44, no. 4, pp. 1455-1460, 1973.

[94] R. Taylor, T. RE, and L. I. CLARK, "FINITE PULSE TIME EFFECTS IN FLASH DIFFUSIVITY METHOD," 1974.

[95] T. Lechner and E. Hahne, "Finite pulse time effects in flash diffusivity measurements," *Thermochimica acta,* vol. 218, pp. 341-350, 1993.

[96] D. G. Park, H. M. Kim, S. J. Baik, B. O. Yoo, S. B. Ahn, and W. S. Ryu, "Correction Effect of Finite Pulse Duration for High Thermal Diffusivity Materials," 2010.

[97] L. Dusza, "Combined solution of the simultaneous heat loss and finite pulse corrections with the laser flash method," *High Temperatures. High Pressures (Print),* vol. 27, no. 5, pp. 467-473, 1995.

[98] C. B. Vining, "An inconvenient truth about thermoelectrics," *Nature Mater.,* vol. 8, pp. 83-89, 2009.

[99] (2016). *Final Technical Report: Thermoelectric Waste Heat Recovery Program for Passenger Vehicles*. Available: https://www.osti.gov/servlets/purl/1337561

[100] A. R. M. Siddique, S. Mahmud, and B. V. Heyst, "A review of the state of the science on wearable thermoelectric power generators (TEGs) and their existing challenges," *Renewable and Sustainable Energy Reviews,* vol. 73, pp. 730-744, 2017.

[101] S. M. K. N. Islam, M. B. Cortie, and X. Wang, "Grape juice: an effective liquid additive for significant enhancement of thermoelectric performance in Cu_2Se, ," *J. Mater. Chem. A,* vol. 8, no. 33, pp. 16913-16919, 2020.

[102] L. Zhao *et al.*, "Significant enhancement of figure-of merit in carbon-reinforced Cu_2Se nanocrystalline solids," *Nano Energy,* vol. 41, pp. 164–171, 2017.

[103] R. Nunna *et al.*, "Ultrahigh thermoelectric performance in Cu_2Se-based hybrid materials with highly dispersed molecular CNTs," *Energy Environ. Sci.,* vol. 10, pp. 1928-1935, 2017.

[104] Q. Hu, Y. Zhang, Y. Zhang, X.-J. Li, and H. Song, "High thermoelectric performance in Cu_2Se/CDs hybrid materials," *J. Alloys Compounds,* vol. 813, p. 152204, 2020.

[105] M. Wojdyr, "Fityk : a general-purpose peak fitting program," *J. Appl. Cryst.,* vol. 43, pp. 1126-1128, 2010.

[106] L. Gulay, M. Daszkiewicz, O. Strok, and A. Pietraszko, "Crystal structure of Cu_2Se," *Chem. Met. Alloys,* vol. 4, no. 3-4, pp. 200-205, 2011.

[107] S. I. Kim *et al.*, "Dense dislocation arrays embedded in grain boundaries for high-performance bulk thermoelectrics," *Science,* vol. 348, no. 6230, pp. 109-114, 2015.

[108] Z.-G. Chen, X. Shi, L.-D. Zhao, and J. Zou, "High-performance SnSe thermoelectric materials: Progress and future challenge," *Prog. Mater. Sci.,* vol. 97, pp. 283-346, 2018.

[109] T. Zhu, Y. Liu, C. Fu, J. P. Heremans, J. G. Snyder, and X. Zhao, "Compromise and synergy in high-efficiency thermoelectric materials," *Adv. Mater.,* vol. 29, no. 14, p. 1605884, 2017.

[110] J.-W. Kim and H.-G. Lee, "Thermal and carbothermic decomposition of Na_2CO_3 and Li_2CO_3," *Metall. Mater. Trans. B,* vol. 32, no. 1, pp. 17-24, 2001.

[111] K. Motzfeldt, "The thermal decomposition. of sodium carbonate by the effusion method," *J. Phys. Chem.,* vol. 59, no. 2, pp. 139-147, 1955.

[112] J.-W. Kim and H.-G. Lee, "Thermal and carbothermic decomposition of Na 2 CO 3 and Li 2 CO 3," *Metallurgical and materials transactions B,* vol. 32, no. 1, pp. 17-24, 2001.

[113] K. Motzfeldt, "The thermal decomposition. of sodium carbonate by the effusion method," *The Journal of Physical Chemistry,* vol. 59, no. 2, pp. 139-147, 1955.

[114] D. K. C. MacDonald, *Thermoelectricity: an introduction to the principles*. Courier Corporation, 2006.

[115] W. Liu, X. Yan, G. Chen, and Z. Ren, "Recent advances in thermoelectric nanocomposites," *Nano Energy,* vol. 1, no. 1, pp. 42-56, 2012.

[116] M. A. Kamarudin, S. R. Sahamir, R. S. Datta, B. D. Long, M. F. Mohd Sabri, and S. Mohd Said, "A review on the fabrication of polymer-based thermoelectric materials and fabrication methods," *The Scientific World Journal,* vol. 2013, 2013.

[117] S. N. Girard *et al.*, "In situ nanostructure generation and evolution within a bulk thermoelectric material to reduce lattice thermal conductivity," *Nano letters,* vol. 10, no. 8, pp. 2825-2831, 2010.

[118] K. S. Novoselov *et al.*, "Electric field effect in atomically thin carbon films," *science,* vol. 306, no. 5696, pp. 666-669, 2004.

[119] K. S. Novoselov *et al.*, "Two-dimensional atomic crystals," *Proceedings of the National Academy of Sciences,* vol. 102, no. 30, pp. 10451-10453, 2005.

[120] M. Yi and Z. Shen, "A review on mechanical exfoliation for the scalable production of graphene," *Journal of Materials Chemistry A,* vol. 3, no. 22, pp. 11700-11715, 2015.

[121] A. Ambrosi, Z. k. Sofer, J. Luxa, and M. Pumera, "Exfoliation of layered topological insulators Bi2Se3 and Bi2Te3 via electrochemistry," *ACS nano,* vol. 10, no. 12, pp. 11442-11448, 2016.

[122] H. Li, J. Wu, X. Huang, Z. Yin, J. Liu, and H. Zhang, "A universal, rapid method for clean transfer of nanostructures onto various substrates," *ACS nano,* vol. 8, no. 7, pp. 6563-6570, 2014.

[123] J. N. Coleman *et al.*, "Two-dimensional nanosheets produced by liquid exfoliation of layered materials," *Science,* vol. 331, no. 6017, pp. 568-571, 2011.

[124] S. M. Liff, N. Kumar, and G. H. McKinley, "High-performance elastomeric nanocomposites via solvent-exchange processing," *Nature materials,* vol. 6, no. 1, pp. 76-83, 2007.

[125] M. Nofar, B. Batı, E. B. Küçük, and A. Jalali, "Effect of soft segment molecular weight on the microcellular foaming behavior of TPU using supercritical CO2," *The Journal of Supercritical Fluids,* vol. 160, p. 104816, 2020.

[126] T. Kajitani, T. Nozaki, and K. Hayashi, "Thermoelectric Iron Oxides," in *Advances in Science and Technology*, 2010, vol. 74, pp. 66-71: Trans Tech Publ.

[127] C. Li *et al.*, "Magnetism-induced huge enhancement of the room-temperature thermoelectric and cooling performance of p-type BiSbTe alloys," *Energy & Environmental Science,* vol. 13, no. 2, pp. 535-544, 2020.

[128] A. Diaconu, A. P. Chiriac, I. Neamtu, and L. E. Nita, "Magnetic Polymeric Nanocomposites," *Polymeric Nanomaterials in Nanotherapeutics,* pp. 359-386, 2019.

[129] O. Bajpai, D. Setua, and S. Chattopadhyay, "A brief overview on ferrite (Fe3O4) based polymeric nanocomposites: recent developments and challenges," *Journal of Research Updates in Polymer Science,* vol. 3, no. 4, pp. 184-204, 2014.

[130] M. Aghayi-Anaraki and V. Safarifard, "Fe3O4@ MOF magnetic nanocomposites: Synthesis and applications," *European Journal of Inorganic Chemistry,* vol. 2020, no. 20, pp. 1916-1937, 2020.

[131] K. Do Kim, S. S. Kim, Y.-H. Choa, and H. T. Kim, "Formation and surface modification of Fe3O4 nanoparticles by co-precipitation and sol-gel method," *Journal of Industrial and Engineering Chemistry,* vol. 13, no. 7, pp. 1137-1141, 2007.

[132] C. Han, N. Cai, V. Chan, M. Liu, X. Feng, and F. Yu, "Enhanced drug delivery, mechanical properties and antimicrobial activities in poly (lactic acid) nanofiber with mesoporous Fe3O4-COOH nanoparticles," *Colloids and Surfaces A: Physicochemical and Engineering Aspects,* vol. 559, pp. 104-114, 2018.

[133] H. Khakbaz *et al.*, "3D printing of highly flexible, cytocompatible nanocomposites for thermal management," *Journal of Materials Science,* vol. 56, no. 10, pp. 6385-6400, 2021/04/01 2021.

[134] N. C. Paxton *et al.*, "Additive manufacturing enables personalised porous high-density polyethylene surgical implant manufacturing with improved tissue and vascular ingrowth," *Applied Materials Today,* vol. 22, p. 100965, 2021.

[135] C. Lin *et al.*, "Processable and recyclable polyurethane/HNTs@ Fe3O4 solid–solid phase change materials with excellent thermal conductivity for thermal energy storage," *Polymer Composites,* 2021.

[136] L. S. Sundar, M. K. Singh, and A. C. Sousa, "Investigation of thermal conductivity and viscosity of Fe3O4 nanofluid for heat transfer applications," *International communications in heat and mass transfer,* vol. 44, pp. 7-14, 2013.

[137] M. Häring, J. Schiller, J. Mayr, S. Grijalvo, R. Eritja, and D. D. Díaz, "Magnetic gel composites for hyperthermia cancer therapy," *Gels,* vol. 1, no. 2, pp. 135-161, 2015.

[138] E. Elbeshir, "On the gum arabic to improve the thermal properties of Fe3O4 nanoparticles," *AIP Advances,* vol. 11, no. 4, p. 045224, 2021.

[139] G. D. Soto *et al.*, "Magnetic nanocomposites based on shape memory polyurethanes," *European Polymer Journal,* vol. 109, pp. 8-15, 2018.

[140] M. B. Cortie, D. L. Cortie, and V. Timchenko, "Heat transfer from nanoparticles for targeted destruction of infectious organisms," *International Journal of Hyperthermia,* vol. 34, no. 2, pp. 157-167, 2018.